

**High-Fidelity Simulations to Study Spray-Induced
Extinction and Particulate Formation
Characteristics of Nonpremixed Ethylene-Air
Flames**

by

Paul G. Arias

A dissertation submitted in partial fulfillment
of the requirements for the degree of
Doctor of Philosophy
(Mechanical Engineering)
in The University of Michigan
2013

Doctoral Committee:

Professor Hong G. Im, Chair
Professor Arvind Atreya
Assistant Professor Mathias Ihme
Associate Professor Angela Violi

© Paul G. Arias 2013
All Rights Reserved

Hay, hermanos, muchísimo que hacer. - Cesar Vallejo
For my father, Carlos, my mother, Patricia, and my sister, Cecilia.

ACKNOWLEDGEMENTS

I would like to give thanks to my advisor, Dr. Hong G. Im, for his support and patience over the years, providing valuable guidance and opening doors that allowed me to see life as an independent researcher.

While at Michigan, I have had the opportunity to work with very brilliant minds in combustion at the Computational Reaction Flows Laboratory. I appreciate their consistent support, and wish them all the best.

The work in this dissertation was supported by the Department of Energy, Office of Basic Energy Science, SciDAC Computational Chemistry Program as well as the National Science Foundation PetaApps Program.

TABLE OF CONTENTS

DEDICATION	ii
ACKNOWLEDGEMENTS	iii
LIST OF FIGURES	vi
LIST OF TABLES	ix
LIST OF APPENDICES	x
LIST OF ABBREVIATIONS	xi
ABSTRACT	xii
CHAPTER	
I. Introduction	1
1.1 High-fidelity numerical simulations of turbulent combustion: current status and challenges	1
1.2 Navier-Stokes Characteristic Boundary Conditions for Mass- Additive Systems	5
1.3 Turbulence and spray induced quenching	7
1.4 Advanced soot model development	8
1.5 Outline of presentation	10
II. Computational development	12
2.1 Introduction	12
2.2 Compressible Navier-Stokes Equations with Lagrangian Droplet Model	13
2.3 Non-conservative and characteristic governing equations	14
2.4 Single Droplet Mean Flow Test	19
2.5 Steady counterflow diffusion flame with water spray	21
2.6 Modified mixture fraction formulation for spray-laden flows	24

2.7	Concluding Remarks	31
III.	Turbulence and spray induced quenching	33
3.1	Introduction	33
3.2	A Unified Extinction Criterion	34
3.3	Problem Configuration	36
3.4	Results	37
3.4.1	Laminar Flames	37
3.4.2	Turbulent Flames	39
3.5	Concluding Remarks	45
IV.	Dynamics of soot formation using MOMIC approach	47
4.1	Introduction	47
4.2	Soot Moments: Method of Moments with Interpolative Closure	47
4.3	Numerical challenges to high-fidelity soot modeling	52
4.3.1	Comparison of MOMIC studies	52
4.3.2	Realizability	53
4.3.3	Results	56
4.3.4	One-dimensional inert, non-reactive, transport test	59
4.3.5	One-dimensional fuel-core, diffusion-flame	59
4.4	Concluding remarks	63
V.	Conclusions	70
5.1	Conclusion	70
5.2	Future work	72
	APPENDICES	75
	BIBLIOGRAPHY	97

LIST OF FIGURES

Figure

2.1	Behaviors of velocity vectors with different outflow boundary conditions; Case A on the left, Case B on the right. The contours represent x-direction velocity at $t=7.10 \mu\text{sec}$ with dynamic range from 200-300 cm/s. The peak value of the x-direction velocity is 314 cm/s. . . .	19
2.2	Maximum normal velocity at both upper and lower outflow boundary. Corrected boundary conditions are activated at $t=7.10\mu\text{sec}$	22
2.3	x-direction velocity isocontours with droplets, $u _{x=0} = 230\text{cm/s}$ and $u _{x=l_x} = -230\text{cm/s}$. From top to bottom, left side, $t=0.01,1.2,2.4,3.6 \mu\text{sec}$. From top to bottom, right side, $t=7.0,7.1,8.4,9.1 \mu\text{sec}$	23
2.4	Scatter plot of temperature vs Z. Outer blue mixture fraction corresponds to domain not affected by spray. From left to right, $t=0.9,1.7,2.8 \mu\text{sec}$	30
2.5	Temperature, uncorrected and corrected mixture fraction variables at $t=2.8 \mu\text{sec}$	30
3.1	Counterflow flame configuration. Solid lines denote potential flow streamlines. Dotted lines represent temperature contours. Solid yellow line indicates the stoichiometric mixture fraction demarcating the flame location.	36
3.2	Heat release rate isocontours with spray overlay (red dots) for Case B at $t = 0.3, 5.7, 6.2 \text{ ms}$	38
3.3	Temporal history of integrated heat release rate and weakness factor at the midpoint of the flame, for the three cases considered.	40

3.4	Spatial distribution of normalized scalar dissipation rate, integrated heat release rate and the weakness factor along the flame surface for Case B at $t = 5.9$ ms.	41
3.5	Temporal evolution of heat release rate isocontours for turbulent flame simulation without spray.	41
3.6	Distribution of the normalized scalar dissipation rate, integrated heat release rate (kW/m^2) and the weakness factor for the turbulent flames without spray at the four times shown in Fig. 3.5	42
3.7	Temporal evolution of heat release rate isocontours for turbulent flame simulation without spray.	43
3.8	Distribution of the normalized scalar dissipation rate, integrated heat release rate (kW/m^2) and the weakness factor for the turbulent flames with spray at the four times shown in Fig. 3.7	43
3.9	Turbulence without spray case; integrated heat release rate (kW/m^2) versus weakness factor along the stoichiometric mixture fraction lines for cumulative data over the simulation time. The vertical line denotes the $R = 1$ condition.	44
3.10	Turbulence with spray case; integrated heat release rate (kW/m^2) versus weakness factor along the stoichiometric mixture fraction lines for cumulative data over the simulation time. The vertical line denotes the $R = 1$ condition.	45
4.1	Ignition delay time as a function of initial mixture temperature for validation of skeletal (68 species) and reduced (62 species) chemical mechanism.	50
4.2	Pyrene mass fraction versus function of residence time	51
4.3	Diffusion flame profile of pyrene (A4) concentration.	51
4.4	Initial conditions for the transport test cases. The moments are plotted in log scale.	56
4.5	One-dimensional evolution of soot profile, with fractional moment diffusion in a quiescent field of pure air, $T=500$ K, $P=1$ atm. Moment profiles in log plot at $t=0.25$ ms	57
4.6	Weighing function for the artificial diffusion filter.	58

4.7	Case NV-DS, $t=0.255\text{ms}$	59
4.8	Case NV-DS, realizability, $t=0.255\text{ms}$	60
4.9	Case NV-FS zoomed, $t=1.725\text{ms}$	61
4.10	Case NV-DS zoomed, $t=1.725\text{ms}$	62
4.11	Plot of mixture fraction Z and temperature across space, initial conditions	63
4.12	Plot of mixture fraction Z , soot volume fraction f_v , average diameter of soot particles d_{avg} , and soot reaction terms, $t=0.0$ ms	64
4.13	Plot of mixture fraction Z , soot volume fraction f_v , average diameter of soot particles d_{avg} , and soot reaction terms, $t=0.25$ ms	65
4.14	Plot of mixture fraction Z , soot volume fraction f_v , average diameter of soot particles d_{avg} , and soot reaction terms, $t=0.37$ ms	66
4.15	Plot of mixture fraction Z , soot volume fraction f_v , average diameter of soot particles d_{avg} , and soot reaction terms, $t=0.0$ ms	67
4.16	Plot of mixture fraction Z , soot volume fraction f_v , average diameter of soot particles d_{avg} , and soot reaction terms, $t=0.25$ ms	68
4.17	Plot of mixture fraction Z , soot volume fraction f_v , average diameter of soot particles d_{avg} , and soot reaction terms, $t=0.75$ ms	69

LIST OF TABLES

Table

2.1	Single droplet test cases, with and without corrected boundary conditions	19
3.1	Parameters used for three laminar test cases.	38
4.1	Cases for soot transport evaluation stability and realizability	61
A.1	Temporal part in characteristic form	85
A.2	Normal flux terms in conservative variable form in terms of \mathcal{L}	85
A.3	Normal flux terms in conservative variable form in terms of \mathbf{d}	86
A.4	Transverse, viscous and source terms w.r.t. x-direction in characteristic form	86
A.5	Transverse, viscous and source terms w.r.t. y-direction in characteristic form	87
A.6	Transverse, viscous and source terms w.r.t. z-direction in characteristic form	87
B.1	Reference parameters for soot	88
B.2	Physical parameters for soot	88
B.3	Soot non-dimensional values	89

LIST OF APPENDICES

Appendix

A. Practical details for Navier-Stokes Characteristic Boundary Conditions (NSCBC) 76

B. Soot source terms for Method of Moments with Interpolative Closure (MOMIC) 88

LIST OF ABBREVIATIONS

CFD	Computational Fluid Dynamics
CFL	CourantFriedrichsLewy
DNS	Direct Numerical Simulation
DRG	Directed Relation Graph
IHR	Integrated Heat Release Rate
MOMIC	Method of Moments with Interpolative Closure
NSCBC	Navier-Stokes Characteristic Boundary Conditions
PAH	polycyclic aromatic hydrocarbons
HACA	Hydrogen Abstraction Carbon Addition
PSDF	Particle Size Distribution Function

ABSTRACT

High-Fidelity Simulations to Study Spray-Induced Extinction and Particulate Formation Characteristics of Nonpremixed Ethylene-Air Flames

by

Paul G. Arias

Chair: Hong G. Im

This work developed and employed high-fidelity direct numerical simulations to investigate fundamental flame behavior in laminar and turbulence nonpremixed flames. The scope of the work includes several advances in computational algorithms such as improved Navier-Stokes Characteristic Boundary Conditions (NSCBC) for mass additive systems and advanced soot models. In addition, detailed investigations into the effects of thermal quenching were conducted in an effort to understand ways of accurately describing the nature of flame extinction comprehensively. The software developed in the course of these investigations allow for multi-platform, massively parallel direct numerical simulations that contribute to the understanding of flame phenomenon and scientific discoveries associated with chemically reacting flows.

The computational component to this study centers on a new formulation of the NSCBC. This formulation resolves a lingering issue of spurious solution behavior encountered in the coupling of Lagrangian spray droplets and the gas phase computational boundary, and is applicable to a host of problems where mass is exchanged

through some feedback mechanism, as is the case in our soot model. The improved boundary conditions are validated through a variety of tests involving droplet evaporation by hot gas as well as laminar flames. This application is then used to study the thermal and aerodynamic quenching effects of droplet and turbulent eddy interactions. The simulations demonstrate that the corrected NSCBC addresses the effects of non-physical acoustic perturbations that manifested as a result of spray-evaporation and computational boundary interaction.

As an important analytical tool for describing spray-laden turbulent combustion problems, a three-stream mixture fraction formulation is developed. This formulation builds upon previous work on three-stream mixture fraction formulations that introduce a gas diluent into a combustion configuration. This method describes the three streams (fuel, oxidizer, and spray) by separate conserved variables, and provides a framework to capture the flame location based on a search algorithm for finding the stoichiometric chemistry balance. The findings show that this three-stream mixture fraction formulation accurately and unambiguously captures the flame location, allowing for a confident analysis of various flame quantities relevant to water spray-flame interactions.

As an application to fundamental and practical combustion problems, the study investigates the interaction of water spray and turbulence with nonpremixed diffusion flames. The simulations incorporate detailed chemistry of ethylene flames, the chemistry of which is recognized as an important chemical pathway for combustion processes. The numerical studies performed include laminar diffusion flames under various strain rates and water spray loading conditions. A unified extinction condition that accounts for thermal quenching and strain induced quenching simultaneously is demonstrated to be effective at capturing the moment of extinction and tracking extinction holes in turbulent flames. The findings show that in the formation of edge flames, the evolution leading to the flame recovery or total extinction is found to de-

pend strongly on the temporal history of the local strain rate as well as the presence of the spray droplets. While turbulent mixing leads to the formation of the edge flames, the presence of spray droplets suppresses the ability of edge flames to heal extinction holes.

The final part of this study examines the dynamics of soot formation in ethylene-air nonpremixed flames using a Method of Moments with Interpolative Closure (MOMIC) approach. The one-dimensional laminar flames studied use detailed chemistry, multi-component transport Computational Fluid Dynamics (CFD) code to provide insights on the advantages and shortcomings of the MOMIC approach in the context of high-fidelity simulations. A number of technical challenges related to the simulation of soot and gas phases were addressed. The nucleation, oxidation, and surface growth reactions for soot contribute to mass exchange with the gas phase species. The treatment of the interpolation moments, which play a role in the diffusion of soot as well as the soot reaction source terms, was found to be consistent with the mathematic description of MOMIC, and was shown to be consistent with the conditions of statistical realizability of the soot moments for the reaction test cases. The results of this study provide the Direct Numerical Simulation (DNS) community with a numerical framework towards the development and implementation of high-fidelity soot sub-models.

CHAPTER I

Introduction

1.1 High-fidelity numerical simulations of turbulent combustion: current status and challenges

In the past few decades, advances in high-performance computing have enabled the study of laboratory scale fluid dynamic problems using high fidelity simulations. Powerful supercomputers with tens of thousands of central processing units (CPUs) with multiple cores, as well as systems utilizing Graphical Processing Units (GPUs) have allowed the use of DNS as a tool to explore the fundamental dynamics of fluid physics. Unlike conventional engineering simulations, the DNS approach is not subject to turbulence modeling errors, thereby allowing the investigation of physical processes from a first-principles approach. The performance capabilities and greater accessibility of supercomputing platforms have expanded the range of physical problems that DNS is able to address. The present study aims to contribute towards the development of high-fidelity simulation capabilities for reacting flows by developing new capabilities pursuant to spray-laden flows and soot formation.

Despite the advancements of high-performance computing platforms, challenges remain in developing software for DNS to be truly predictive models for turbulent combustion. The benefits of such detailed simulations come at a major computational

overhead in terms of computational time, as the spatial and temporal resolution requirements needed to capture the large scale disparity in physical and chemical processes increases enormously with the flow Reynolds numbers. In addition, the complex chemical reaction processes add ever more serious demands on computational cost, due to the need to incorporate a large number of chemical species and reactions at vastly different time scales. Therefore, as research continues to explore more accurate and reliable modeling of turbulent combustion and underlying physical mechanisms, a sustained effort is necessary to develop computational models and solution algorithms for robust and accurate simulation of complex physical processes of interest.

One of the scientific goals of this study is to unravel, by means of detailed numerical simulations, the physical processes responsible for flame extinction due to evaporating water spray. The problem is of practical interest in fire safety application, in which utilization of fine water droplets is considered a more effective means for flame suppression. The problem is also important as temperature control mechanism in gas turbines, where fast time-scale and inexpensive control of combustion can extend their mechanical lifetime. We attempt to develop a unified criterion for flame extinction that extends the classical extinction strain condition to include non-adiabatic configurations in which additional flame weakening arises from heat losses due to evaporative cooling or thermal radiation. It is recognized that flame extinction occurs from combined effects of strain, preferential diffusion, and heat losses, such that the corresponding extinction condition for nonpremixed laminar flames, usually given by the critical scalar dissipation rate, needs to be appropriately modified to account for other external flame weakening effects. Recent studies (*Wang and Trouve (2006)*, *Narayanan and Trouve (2009)*) addressed this issue for a flame subjected to radiative cooling by a solid wall. In order to accomplish this goal, this study addresses some computational issues associated with the liquid-gas phase coupling effects. The present study considers only a sparse liquid spray with relatively

monodisperse size distribution. The transport processes of individual droplets are solved by a Lagrangian particle-in-cell method developed and implemented into the DNS code by *Wang and Rutland* (2007). Several associated computational challenges that have not been fully addressed in the past include consistent acoustically non-reflecting boundary conditions for mass-additive systems and a correct way to identify and track the flame location in the presence of additional mass generation in the gas phase equations due to water evaporation.

Recent studies (*Yoo and Im* (2007b) and *Sutherland and Kennedy* (2003)) provide a comprehensive framework for the development of the characteristic boundary conditions for combustion problems, underscoring the importance of accounting for reactive terms and transverse terms in the development of acoustically non-reflecting boundary conditions. On the other hand, numerical simulations of spray-laden flows in combustion (*Xia et al.* (2008)) commonly treat the boundary conditions by utilizing a sponge layer in order to damp out the numerical noise generated at the boundary. This approach, however, often demands that a region of space within the domain be damped by artificially increasing the viscosity (*Coloni* (2004)). In the counterflow flame simulation to be considered in this study, the artificial viscosity modification could lead to reduction in the solution fidelity. Thus, a generalized formulation of the characteristic boundary conditions in the presence of mass addition by spray evaporation is sought. It is attempted to mitigate the non-physical perturbations that emanate from coupled particle-gas phase at the boundary without the need for artificial damping.

Another scientific goal of this study is to create a framework for the development and implementation of a high-fidelity soot model into DNS. The development of high-fidelity soot models will provide detailed information on interactions between turbulence, radiation, chemistry and soot formation. The emission of soot from combustion systems is a major concern in the design of practical combustion because soot

formation is a symptom of inefficient combustion and because of negative environmental and health effects of particulates. Toward the challenging goal of developing predictive soot models in turbulent combustion with detailed chemistry, the present study mainly addresses some subtle computational issues that have not been fully resolved in previous studies, such as the accuracy and stability metrics needed to resolve computational challenges associated with the MOMIC, which is considered an optimal approach in terms of accuracy and computational efficiency.

In the last few decades, the development and implementation of soot models in high fidelity simulations have evolved significantly. *Yoo and Im (2007a)* utilized a semi-empirical soot model to study the effects of turbulence, chemistry, and radiation interactions in a counterflow diffusion flames. While the semi-empirical model provided useful information regarding the interaction of soot chemistry and transport in the presence of turbulent flows, the model utilized (*Moss et al. (1988)*, *Moss et al. (1995)*) suffers from limitations: (i) the method requires a priori adjustment of key parameters in the soot formation model, and (ii) the soot inception species was acetylene (C_2H_2), which has been found to over-predict the soot volume fraction and number density (*Mehta et al. (2009)*). Recent work by *Lignell et al. (2007)* demonstrated significant progress towards detailed soot modeling in DNS by utilizing simpler version of the method of moments, predicting the soot mass and number density. The present study extends the state of the art in combustion DNS by incorporating higher order method of moments with interpolative closure, and a more comprehensive detailed reaction mechanism to include polycyclic aromatic hydrocarbons (PAH) precursor, such as pyrene, as the main soot nucleation precursor.

In the validation and parametric simulations of the above problems, the counterflow diffusion flame has served as an ideal model and has been adopted as a main configuration. The one-dimensional structure of counterflow flames, in which important scalars can be defined as a function of mixture fractions, provides an adequate

database for the detailed analysis of flame extinction and re-ignition, flame propagation, and pollutant formation. Since the physical configuration is also studied extensively in experiments, the numerical configuration and integration of the modeling advancements can be used to validate with experimental results. Key science issues of this study focus on the fundamental understanding of extinction phenomenon during the interaction of flow turbulence, flame, and spray evaporation. The soot model development study is mainly focused on the assessment of the various modeling approaches and some quantitative evaluation of the accuracy of the prediction of key soot variables.

More specific details of the objectives for each subjects described above are discussed in the following.

1.2 Navier-Stokes Characteristic Boundary Conditions for Mass-Additive Systems

An important challenge in DNS of compressible flows is the numerical treatment of boundary conditions. While high-fidelity codes are designed to provide a high degree of numerical accuracy, these algorithms are mostly non-dissipative and may be subjected to strong sensitivities to improper boundary condition treatment. For the compressible formulation adopted in the present DNS, it is critical to ensure that the boundaries are transparent to the impinging acoustic waves, or any spurious reflection or amplification of the acoustic wave energy at the boundary may cause a sever contamination of the solution fidelity. The problem is even more challenging in DNS studies that are confined to a finite domain size due to computational cost consideration, and hence need to deal with a significant level of flow action at the boundaries.

The approach to specifying characteristic boundary conditions was initially devel-

oped for a hyperbolic system of Euler equations for the computational aero-acoustics applications (*Rudy and Strikwerda (1980), Thompson (1987)*). This method requires the derivation of the Euler equations in characteristic wave space, thereby allowing the definition of the flow dynamics at the boundary as a system of characteristic waves. The approach has subsequently been adapted to the system of viscous Navier-Stokes equations for subsonic reacting flow applications (*Poinsot and Lele (1992)*). This approach, known as NSCBC, has been further extended to multi-component reacting flows (*Baum et al. (1995)*), treatment of chemical source terms (*Sutherland and Kennedy (2003)*), a low Mach number asymptotic expansion to decouple acoustics from flow transport (*Wang and Trounev (2004)*), and the treatment of strong transverse terms present in turbulence simulations (*Yoo et al. (2005), Yoo and Im (2007b)*).

While significant advances have been made in robust and accurate implementation of the characteristic boundary conditions, additional challenges arise in the spray-laden flows, which is the subject of this study. In particular, the challenge is to allow evaporating liquid droplets to pass through the numerical boundaries without generating unphysical perturbations that appear due to mass addition to the Eulerian solver. The present study aims to overcome this difficulty by generalizing the formulation of NSCBC for mass-additive systems in coupled Lagrangian-Eulerian transport equations. The present approach is distinguished from previous semi-empirical approaches utilized in lower order finite difference and finite volume methods (*Xia et al. (2008)*), in which the acoustic perturbations generated by the interaction of droplets and gas phases are damped out by an artificial sponge layer. Unfortunately, the latter approach affects the fidelity of solutions well into the computational domain, and hence is not well suited for high-fidelity DNS application. Instead, the present approach carefully addresses various acoustic sources arising from the liquid-gas interaction by implementing consistent characteristic equations at the boundaries, thereby

eliminating the need to employ any artificial boundary damping methods.

1.3 Turbulence and spray induced quenching

Flame extinction has a significant impact on the efficiency of non-premixed combustion processes. It can affect the overall burning rate as well as undesired pollutant formation (CO, NO_x, soot). In internal combustion engines, extinction can occur from the turbulence intensity associated with the momentum driven, high Reynolds number flows, along with heat losses to the walls. In low Reynolds number flows, extinction can result from the low intensity combustion due to increased volumetric heat loss (such as gas radiation). In fire suppression application, addition of inert gases or water spray is used to promote heat losses due to dilution and evaporative cooling. The study of spray-induced flame quenching is of practical relevance in fire safety application. While traditional sprinkler systems achieve fire suppression through fuel cooling or cutting off the oxidizer contact, newer fire suppression systems exploits direct flame cooling by using fine water mist. This has the potential benefit of more efficient fire suppression by reducing the water consumption, and increasing performance by allowing for fine mist to be more easily dispersed on the objects. Despite high interest in this technology, there are few studies that address the fundamental mechanisms of water spray interaction with flames.

A systematic characterization of flame extinction mechanism has been established in combustion theory (*Williams (1985)*). Extinction occurs if the Damköhler number, defined as the ratio of the characteristic flow residence time to the characteristic chemical reaction time, falls below a critical limit. In the above examples, flame extinction mechanism can be categorized into (a) strain-induced quenching due to reduced flow residence time and (b) suppression of chemical reactions due to thermal cooling or radical inhibition. One of the ultimate goals of the present study is to identify an extended unified extinction criterion that accounts for the latter effect

arising from the spray evaporation.

An additional subtle issue in accurate modeling of spray-laden flames lies in the post-processing and analysis of the flame data. A standard approach to describe nonpremixed flame characteristics is to describe the solution variables in terms of the conserved scalar variable based on the elemental mass fraction for a two (fuel and air) stream mixture system. This approach is subjected to a large uncertainty in the presence of water evaporation within the flame zone as the additional hydrogen and water vapor generated in the mixture can shift the mixture fraction variable. To resolve this issue, the present study investigates an alternative definition of the mixture fraction variable based on three stream mixture systems.

The above theoretical and mathematical framework is applied to parametric simulations of turbulent nonpremixed flames with spray injection and the resulting extinction characteristics are systematically analyzed. The validity of the unified extinction criteria is also assessed.

1.4 Advanced soot model development

Despite the recent advances in combustion DNS using detailed gas-phase chemistry, high fidelity models for accurate prediction of soot formation is not fully developed. The primary reason for the difficulty in modeling soot formation and transport is due to the multi-scale nature of the soot dynamical processes. The growth of soot takes place primarily at molecular scales (*Frenklach and Wang (1990)*) while the transport of soot particles takes place at much larger scales on the order of millimeters to meters. Accurate simulations of soot, particularly spanning these scales with minimal compromise on fidelity to the physics of soot formation and transport is a daunting task. This study attempts to advance the numerical capabilities of DNS to simulation soot formation and transport by incorporating a high-fidelity state-of-the-art method of moment algorithms. This numerical modeling approach will be directly

applied to the study of conditions common in practical combustion systems.

Previous turbulent flames simulations that sought to simulate soot used semi-empirical soot models (*Yoo and Im (2007a)*, *Lignell et al. (2007)*). These models proved to be numerically efficient because of the low level of additional computational loading (often two additional transport variables). Nonetheless, the fidelity of the methods used is subject to a priori modification of parameters associated with the formation mechanisms that allow for matching with experimental data, and hence, are problem dependent. Meanwhile, a detailed soot model has been developed (*Appel et al. (2000)*, *Frenklach and Wang (1990)*) that considers the use of PAH as the primary inception species. In this model, the coalescence and nucleation of PAH molecules results in the formation of the soot particles, while the surface growth of the particles occurs both through coalescence of soot particles as well as the Hydrogen Abstraction Carbon Addition (HACA) mechanism. This mechanism requires a large number of chemical species (approximately 100 species and 500 reactions), which is appropriate due to the level of chemical complexity in soot formation. Nonetheless this places a significant computational burden due to the need for greater spatial accuracy and the need for smaller time steps due to chemical stiffness. To ameliorate this burden, our code incorporates a specialized reduced mechanism (*Lu and Law (2005)*) that reduced the number of species and utilizes quasi-steady state assumptions (QSSA) to reduce a larger number of chemical reactions to algebraic equations.

The development of a strategy that allows for the incorporation of the high fidelity soot models is described. A statistical approach to soot modeling is considered favorable as a means to describe the dynamics associated with transport due to the size, structure, and prevalence of soot particles in diffusion flames. These soot moments describing soot particles are utilized as the primary transport variables.

An important challenge in the development of soot moment transport is the need to provide closure to terms that appear as part of the transport equations. The deriva-

tion of soot moment transport equations introduces moment variables of a fractional order that play important roles in the diffusion and reaction terms. In this study, the method to derive these terms is through the use of interpolation schemes that calculate the values of the fractional moments from the transported whole moments. This approach, called method of moments with interpolative closure (MOMIC), is adopted as a submodel for the present DNS. This method was originally developed in the context of one-dimensional laminar premixed flames (*Frenklach (2002)*). It was discovered that in the context of high-order spatial and temporal methods, this approach presented a number of computational issues leading to unphysical oscillations. The present study is largely devoted to a thorough investigation of these numerical issues in order to suggest rational remedies for DNS applications, and points to future work in soot particle dynamic modeling that needs to be addressed.

1.5 Outline of presentation

The subsequent chapters are organized as follows. In Chapter 2, a generalized formulation for NSCBC for spray-laden flows is developed. A special treatment for the characteristic boundary conditions in the presence of liquid droplets at the boundary is described in detail. The validity of the modified NSCBC is tested by a simple two-dimensional simulation with a single droplet passing through the boundary. Subsequently, the method is validated in a more hostile condition of turbulent flames with a large number of droplets, demonstrating that the new development results in a significantly improved level of stability and accuracy of the simulation. In addition, an extended mixture fraction formulation is developed and the theoretical reasoning for the new formulation in a three-stream mixture system is discussed.

Chapter 3 presents the application of the computational methods developed in Chapter 2 by investigating the characteristics of flame extinction induced by fine spray evaporation. In particular, a unified extinction criterion is proposed in order

to account for both strain-induced flame weakening and the temperature attenuation due to the heat losses associate with water evaporation. The results from various test simulations demonstrate that the unified extinction criterion serves as an accurate detection of the onset of flame extinction in the presence of various physical mechanisms that cause flame weakening.

Chapter 4 describes the detailed soot model based on the MOMIC approach along with consideration of PAH as a soot precursor. Computational issues that are responsible for the generation of spurious solution oscillations are identified in a systematic manner, and the options to alleviate the issues are presented.

In Chapter 5, the overall results are summarized and possible immediate future work is recommended and discussed.

CHAPTER II

Computational development

2.1 Introduction

This chapter presents two essential computational developments to allow accurate and robust simulations of spray-laden reacting flows: (a) an improved characteristic boundary conditions, and (b) a modified mixture fraction formulation, both of which account for the gas-liquid phase coupling via additional source terms associated with liquid spray evaporation. The former resolves many lingering issues associated with the acoustic perturbations resulting from the interaction of mass-feedback with gas phase at the computational boundaries, while the latter provides a means to accurately capture the flame location and associated characteristics in the presence of detailed chemistry and mass interaction due to spray evaporation. The improvements achieved by the modified approaches are validated by test simulations. The improved boundary conditions are tested by the advection of an evaporating water droplet passing through an outflow boundary. The validity of the new mixture fraction formulation is tested by a simulation of steady laminar flames subjected to a monodisperse droplet spray injected from the oxidizer stream. Improvements on the laminar flame location diagnostic tools that aid in characterizing flame behavior under water spray loading conditions are presented, described in detail in *Narayanan et al.* (2009b) It is demonstrated that the improved boundary conditions allows for accurate

and efficient high fidelity simulations of laminar and turbulent flames interacting with liquid droplets.

2.2 Compressible Navier-Stokes Equations with Lagrangian Droplet Model

The system of conservation equations for general compressible reacting flows with detailed chemistry and transport is described. Defining the total specific energy as:

$$e_t = \frac{\mathbf{u}_\alpha \cdot \mathbf{u}_\alpha}{2} - \left(\frac{p}{\rho}\right) + \sum_{i=1}^N h_i Y_i \quad (2.1)$$

we can write the conservation of mass, momentum and energy as:

$$\frac{\partial}{\partial t} \begin{bmatrix} \rho \mathbf{u}_\alpha \\ \rho \\ \rho e_t \\ \rho Y_i \end{bmatrix} = \begin{bmatrix} -\nabla_\beta \cdot (\rho \mathbf{u}_\alpha \mathbf{u}_\beta + p \delta_{\alpha\beta}) + \nabla_\beta \cdot \tau_{\beta\alpha} + \rho \sum_{i=1}^N Y_i \mathbf{f}_{i\alpha} + \psi_{u_\alpha} \\ -\nabla_\beta \cdot (\rho \mathbf{u}_\beta) + \psi_\rho \\ -\nabla_\beta \cdot [(\rho e_0 + p) \mathbf{u}_\beta] + \nabla_\beta \cdot (\tau_{\beta\alpha} \cdot \mathbf{u}_\alpha - \mathbf{q}_\beta) + \rho \sum_{i=1}^N \mathbf{f}_{i\beta} \cdot (\mathbf{u}_\beta + \mathbf{V}_{i\beta}) + \psi_e \\ -\nabla_\beta \cdot (\rho Y_i \mathbf{u}_\beta) - \nabla_\beta \cdot (\rho Y_i \mathbf{V}_{i\beta}) + W_i \dot{\omega}_i + \psi_{Y_i} \end{bmatrix} \quad (2.2)$$

where ψ_α is the momentum source term in each direction, ψ_ρ is the mass added to the gas phase, ψ_e is the energy source term, ψ_{Y_i} represents the component of the mass that may be added to the individual species that we are including in the chemistry. As in *Sutherland and Kennedy* (2003), the ∇_β operation represents the gradient in direction β , Y_i is the species mass fraction, $W_i \dot{\omega}_i$ represents the species mass reaction rate, $\tau_{\beta\alpha}$ represents the viscous stress tensor, \mathbf{q}_β represents the heat flux vector, $\mathbf{V}_{i\beta}$ is the species mass diffusion velocity, and $\mathbf{f}_{i\alpha}$ represents a force field (such as gravity) for each component i .

The spray droplets are treated in a Lagrangian formulation (*Wang and Rutland* (2005), *Wang and Rutland* (2007)), where the drag force is derived by Stokes law,

and the thermal conductivity is assumed infinite inside the droplet. The Lagrangian equations of motion for the momentum, mass, and energy can be expressed in the following manner:

$$\begin{bmatrix} \frac{dx_{d,i}}{dt} \\ m_d \frac{du_{d,i}}{dt} \\ \frac{dm_d}{dt} \\ \frac{dT_d}{dt} \end{bmatrix} = \begin{bmatrix} u_{d,i} \\ F_{gd,i} \\ -2\pi\rho D r_d Sh_d B_M \\ \frac{4\pi r_d^2}{m_d c_{liq}} \left[\rho \frac{dr_d}{dt} L_{vap} + \frac{\lambda_g (T - T_d) Nu_d}{2r_d} \right] \end{bmatrix} \quad (2.3)$$

where subscript d indicates droplet properties, and the Sherwood number Sh_d , Nusselt number Nu_d , and the mass transfer number B_M are defined in *Wang and Rutland (2007)*. The source terms $\psi_{\rho-Y_i}$ that provide feedback to the gas phase are expressed as:

$$\begin{bmatrix} \psi_\rho \\ \psi_{u_\alpha} \\ \psi_e \end{bmatrix} = \begin{bmatrix} -\frac{1}{\Delta V} \sum_{k=1}^{n_d} \left(\frac{dm_d}{dt} \right)_k \\ -\frac{1}{\Delta V} \sum_{k=1}^{n_d} \left(F_{gd,i} + \frac{dm_d}{dt} u_{d,i} \right)_k \\ -\frac{1}{\Delta V} \sum_{k=1}^{n_d} \left[\frac{d(m_d h_d)}{dt} + F_{gd,i} u_{d,i} + \frac{dm_d}{dt} \left(\frac{1}{2} u_{d,i}^2 \right) \right]_k \end{bmatrix} \quad (2.4)$$

One important feature of this method is that additional mass is introduced into the gas-phase Navier-Stokes equations. This motivates the need to derive the boundary conditions for mass-additive systems.

2.3 Non-conservative and characteristic governing equations

In order to specify boundary conditions, where the primitive variables are described, it is more convenient to use the non-conservative form of the Navier-Stokes equations. Moreover, the characteristic form of the Navier-Stokes equations allows an identification of characteristic wave speeds and amplitudes that need to be properly treated in order to render acoustically transparent boundaries. The extension of characteristic boundary condition formulations to the viscous Navier-Stokes equa-

tions, named the NSCBC, was first developed by *Poinsot and Lele* (1992). A series of further improvements have since been reported, such as the study by *Sutherland and Kennedy* (2003) incorporating a correct treatment of reaction source terms, and studies (*Yoo et al.* (2005) *Yoo and Im* (2007b)) accounting for strong tangential velocity and viscous shear stresses at the boundaries. These efforts significantly improved the stability and accuracy of turbulent reacting flow simulations in the presence of considerable physical and chemical activities near the computational boundaries. In the present study, the NSCBC approach is further extended to account for gas-liquid phase interactions near the boundaries.

Thompson (1987) described the nature of the incoming and outgoing waves by analyzing the behavior of the hyperbolic part of the Navier-Stokes equations. The Euler equations are described in the following way:

$$\frac{\partial \tilde{\mathbf{U}}}{\partial t} + \frac{\partial \mathbf{F}}{\partial x} + \mathbf{C}' = 0 \quad (2.5)$$

$$\begin{array}{ccc} & \mathbf{P}^{-1} \Downarrow & \Uparrow \mathbf{P} \\ \frac{\partial \mathbf{U}}{\partial t} + \mathbf{A} \frac{\partial \mathbf{U}}{\partial x} + \mathbf{C} & = & 0 \end{array} \quad (2.6)$$

$$\begin{array}{ccc} & S^{-1} \Downarrow & \Uparrow S \\ S^{-1} \frac{\partial \mathbf{U}}{\partial t} + S^{-1} \mathbf{A} \frac{\partial \mathbf{U}}{\partial x} + S^{-1} \mathbf{C} & = & 0 \end{array} \quad (2.7)$$

The variables $\tilde{\mathbf{U}}$ and \mathbf{U} represent the conservative and primitive variables of the Euler equations, respectively; \mathbf{F} represents the flux vector, which can be represented in primitive variable space by $\mathbf{A}\partial\mathbf{U}/\partial x$. \mathbf{C}' and \mathbf{C} are inhomogeneities that appear typically in non-cartesian grids. \mathbf{A} is a similarity matrix of the following form:

$$\mathbf{A} = S\mathbf{\Lambda}S^{-1} \quad (2.8)$$

The rows of matrix S represents the left eigenvectors, and the columns of S rep-

represent the right eigenvectors of \mathbf{A} . Matrix Λ represents the eigenvalues of matrix \mathbf{A} . The equations are ordered such that $\lambda_1 \leq \lambda_2 \leq \dots \leq \lambda_n$, where n is the number of equations in the system.

With Eqn. 2.8, we can represent Eqn. 2.7 in component form as:

$$\mathbf{l}_i \frac{\partial \mathbf{U}}{\partial t} + \lambda_i \mathbf{l}_i \frac{\partial \mathbf{U}}{\partial x} + \mathbf{l}_i \mathbf{C} = 0 \quad (2.9)$$

Equation 2.9 provides the mathematical reasoning needed to formulate acoustically transparent numerical boundary conditions. The approach of NSCBC is to operate directly on the characteristic equations which provide the appropriate expression for the evolution of the conservative variables.

Following *Thompson (1987)*, we adopt the method of separating the contributions of the convective terms and the viscous/diffusive terms, and the contributions of the normal components and tangential components with respect to the boundary direction. Considering the mass source terms resulting from the liquid droplet evaporation, the full transport equations in conservative, primitive and characteristic variables are written as

$$\frac{\partial \mathbf{U}_\alpha}{\partial t} + \nabla_{(n)} \cdot \mathbf{F}_\alpha^{(n)} + \nabla_{(t)} \cdot \mathbf{F}_\alpha^{(t)} = \mathbf{D}_\alpha^{(n)} + \mathbf{D}_\alpha^{(t)} + \mathbf{s}_\alpha \quad (2.10)$$

$$(\mathbf{P})_{ba}^{-1} \Downarrow \quad \Uparrow \mathbf{P}_{ab}$$

$$\frac{\partial U_b}{\partial t} + A_{bd}^{(n)} \cdot (\nabla_{(n)} \cdot U_d) + A_{bd}^{(t)} \cdot (\nabla_{(t)} U_d) = D_b^{(n)} + D_b^{(t)} + s_b \quad (2.11)$$

$$(S^{(n)})_{cb}^{-1} \Downarrow \quad \Uparrow S_{bc}^{(n)}$$

$$(S^{(n)})_{cb}^{-1} \frac{\partial U_b}{\partial t} + \mathcal{L}_c^{(n)} + \mathcal{A}_{cd}^{(t)} \cdot (\nabla_{(t)} U_d) = \mathcal{D}_c^{(n)} + \mathcal{D}_c^{(t)} + \mathfrak{s}_c \quad (2.12)$$

where \mathbf{U} and U represent the conservative and primitive variables of the Navier-Stokes equations. The terms \mathbf{D} , D , and \mathcal{D} represent the diffusive terms in conservative, primitive and characteristic space; superscripts (n) and (t) represent the normal

and tangential components with respect to the boundary condition direction of interest; \mathbf{F} represent the convective fluxes; subscripts a, b, c , and d are equation indices; and \mathbf{s} , s , and \mathbf{s} represent source terms for the governing equations in the three different levels.

The transport of liquid spray droplets is described by the Lagrangian particle-in-cell method implemented into the present DNS code by *Wang and Rutland (2007)*. There are a number of source terms arising from the liquid vaporization. First the evaporation of water presents a source term in the continuity equation. Furthermore, there is a momentum exchange from liquid to gas phase through the phase change process as well as the Stokes drag force. Finally, the droplet evaporation also serves as a sink term in the gas-phase energy equation. All these source terms appearing in the transport equations are expressed as:

$$\begin{bmatrix} s_u \\ s_v \\ s_w \\ s_\rho \\ s_p \\ s_{Y_i} \end{bmatrix} = \begin{bmatrix} \Sigma_{i=1}^N Y_i f_{i,x} + (\psi_u - w\psi_\rho)/\rho \\ \Sigma_{i=1}^N Y_i f_{i,y} + (\psi_v - v\psi_\rho)/\rho \\ \Sigma_{i=1}^N Y_i f_{i,z} + (\psi_w - w\psi_\rho)/\rho \\ \psi_\rho \\ (\gamma - 1)(\Sigma_{i=1}^N [-(h_i - c_p T W/W_i)(W_i \dot{\omega}_i + \psi_\rho \delta_{i,H_2O}) \\ + \rho Y_i f_{i,\alpha} V_{i,\alpha}] + \frac{1}{2} \mathbf{u}_\alpha \mathbf{u}_\alpha \psi_\rho - \mathbf{u}_\alpha \psi_{\mathbf{u}_\alpha} + \psi_{e_t}) \\ (1/\rho)(W_i \dot{\omega}_i + (1 - Y_i)\psi_\rho \delta_{i,H_2O}) \end{bmatrix} \quad (2.13)$$

To derive physically correct boundary conditions for the above source terms, the steps described by (*Sutherland and Kennedy (2003)*) are used:

(1) At the beginning of each stage in the time-integration (R-K, Adams-Bashford, etc.), decompose the \mathbf{U} -vector in to the primitive variables, $U = \{u, v, w, \rho, p, Y_i, M_i\}$ where M_i represents additional scalars from sub-models that introduce mass source terms into the system.

(2) Impose any boundary conditions involving primitive variables (i.e. no-slip on channel walls).

(3) Compute diffusive flux terms $(\tau_{\beta\alpha}, \mathbf{q}_\alpha, \rho Y_i \mathbf{V}_{i\alpha})$.

(4) Impose any boundary conditions on the diffusive flux terms.

(5) Compute the full right-hand side (RHS) of all equations.

(6) Remove the RHS terms associated with the normal-to-boundary characteristics at all points along the boundary by:

i. Computing the wave amplitude variations $\mathcal{L}_c^{(n)}$ using data interior to the domain, irrespective of direction of associated eigenvalue.

ii. Computing the normal-to-boundary advective component of the primitive NSE, $d_b^{(n)} = A_{bd}^{(n)} \cdot (\nabla_{(n)} \cdot U_d)$ by using the computed wave amplitude variations.

iii. Computing the normal-to-boundary advective component of the conservative NSE, $\nabla_n \cdot \mathbf{F}^{(n)}$ by using the $d_b^{(n)}$ and subtracting from the RHS terms.

iv. For $\mathcal{L}_c^{(n)}$ associated with incoming eigenvalues, impose appropriate values corresponding to the intended boundary condition. Compute the $\mathcal{L}_c^{(n)}$ associated with outgoing eigenvalues with interior data.

v. Recompute the values of $d_b^{(n)}$ with the values of $\mathcal{L}_c^{(n)}$, some of which were just previously modified to account for the intended boundary condition.

vi. Compute $\nabla_n \cdot \mathbf{F}^{(n)}$ from the $d_b^{(n)}$ values and add to the RHS.

(7) The conservative variable \mathbf{U} -vector can now be updated at all boundary points with the adjusted RHS.

This new formulation is tested on two configurations. A single droplet in hot ambient air is simulated in order to test the effects on the boundary from a single evaporating droplet. A more complex two-dimensional counterflow configuration is used in order to test the overall effects of a large number of droplets interacting with the outflow boundary.

2.4 Single Droplet Mean Flow Test

To test the new source terms for NSCBC, a single stationary droplet was injected into air with a mean flow of 230 cm/s and uniform temperature at 1000K. This is done in order to observe carefully how the temperature, pressure, and velocity fields are affected by the injection of a droplet. While the droplet-to-gas-phase interaction occurs as expected, without the corrected boundary conditions, an unphysical acceleration in the solution variables occurs at the outflow boundary.

Case	gas-phase conditions	boundary condition
A	$u = 230\text{cm/s}, T = 1000\text{ K}$	uncorrected
B	$u = 230\text{cm/s}, T = 1000\text{ K}$	corrected

Table 2.1: Single droplet test cases, with and without corrected boundary conditions

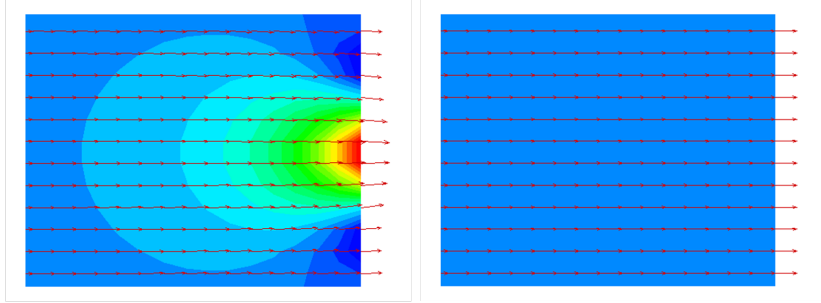


Figure 2.1: Behaviors of velocity vectors with different outflow boundary conditions; Case A on the left, Case B on the right. The contours represent x-direction velocity at $t=7.10\ \mu\text{sec}$ with dynamic range from 200-300 cm/s. The peak value of the x-direction velocity is 314 cm/s.

Figure 2.1 shows that without the appropriate boundary conditions, the gas-phase velocity exhibits an unphysical large acceleration, increasing the maximum velocity to 314 cm/s. At the same simulation time and location for Case B, the mean flow is maintained at 230 cm/s. Several studies have recognized the importance of additional source terms. *Yoo and Im* (2007b) explained the addition of transverse terms address some lingering issued associated with pressure drift when these values are large.

Following from the approach of locally one-dimensional inviscid (LODI) approaches, the non-reflecting boundary condition at $x = l_x$ is given by:

$$L_1^{(x)} = \alpha(p - p_\infty) + L_{1,exact}^{(x)} \quad (2.14)$$

A generalized expression for the wave amplitude (*Yoo and Im (2007b)*) accounting for transverse terms is represented as:

$$L_1^{(x)} = \alpha(p - p_\infty) + a\mathfrak{T}_{1,exact}^{(x)} + (1 - a)\mathfrak{T}_1^{(x)} + V_1^{(x)} + S_1^{(x)} \quad (2.15)$$

Appendix A provides the primitive variable constituents of the transverse, viscous and source terms.

In Case A, the effective characteristic wave amplitude was:

$$L_1^{(x)} = \alpha(p - p_\infty) + a\mathfrak{T}_{1,exact}^{(x)} + (1 - a)\mathfrak{T}_1^{(x)} + V_1^{(x)} + S_1^{(x)} - S_{1,spray}^{(x)} \quad (2.16)$$

This results in the temporal form of the characteristic wave:

$$\frac{1}{2} \left(\frac{\partial p}{\partial t} - \rho c \frac{\partial u}{\partial t} \right) = -\alpha(p - p_\infty) - a(\mathfrak{T}_1 - \mathfrak{T}_{1,exact}) + S_{1,full} - S_{1,gas} \quad (2.17)$$

The term $S_{1,full} - S_{1,gas}$ corresponds to an unsteady value that serves as the source of velocity and pressure disturbances.

A new generalized expression for the wave amplitude is proposed as:

$$L_1^{(x)} = \alpha(p - p_\infty) + a\mathfrak{T}_{1,exact}^{(x)} + (1 - a)\mathfrak{T}_1^{(x)} + V_1^{(x)} + S_{1,full}^{(x)} \quad (2.18)$$

where $S_{1,full}^{(x)} = S_{1,spray}^{(x)} + S_{1,gas}^{(x)}$. This formulation leads to the temporal form:

$$\frac{1}{2} \left(\frac{\partial p}{\partial t} - \rho c \frac{\partial u}{\partial t} \right) = -\alpha(p - p_\infty) - a(\mathfrak{T}_1 - \mathfrak{T}_{1,exact}) \quad (2.19)$$

The above form indicates that the variation in pressure and velocity is mitigated by attenuating pressure values to the intended target value. In the present study, the counterflow diffusion flame configuration is used to confirm that the improved boundary conditions works in cases where strong transverse values are encountered along with water-gas phase interaction.

2.5 Steady counterflow diffusion flame with water spray

The counterflow configuration test will serve as a convenient way to ascertain the effectiveness of the corrected boundary conditions under a spatially varying and high water loading scenario. The transverse boundary velocity varies from -230cm/s to 230cm/s along the outflow boundary. Once the spray injection begins, we find that many droplets are advected by the local gas velocity without closely interacting with the high temperature region. This creates a spray zone where the droplets are evaporating at different rates. This configuration was tested in the following way:

1. Obtained a steady state counterflow diffusion flame using S3D.
2. Injected droplets near the flame on the oxidizer side at a continuous rate.
3. The outflow boundary conditions were left in their original form, to highlight the severity of the error on solution.
4. At later time, we turned on the improved boundary conditions module to recapture the correct solution.

Figure 2.3 shows that with multiple droplet interaction, the boundary conditions significantly affect the solution, showing the transverse velocity at the outflow. While the acceleration of the gas in the normal direction is expected to be large (see Fig.

2.2), the transverse direction velocity is severely affected for a large distance away from the zone of the interacting droplets. This is because the droplets have a larger zone-of-interaction thickness, and the effect of the localized error propagates along the boundary. Once the corrected boundary conditions were activated, the behavior of the transverse velocity improved and returned to the original steady state profile that should observe for counterflow diffusion flames.

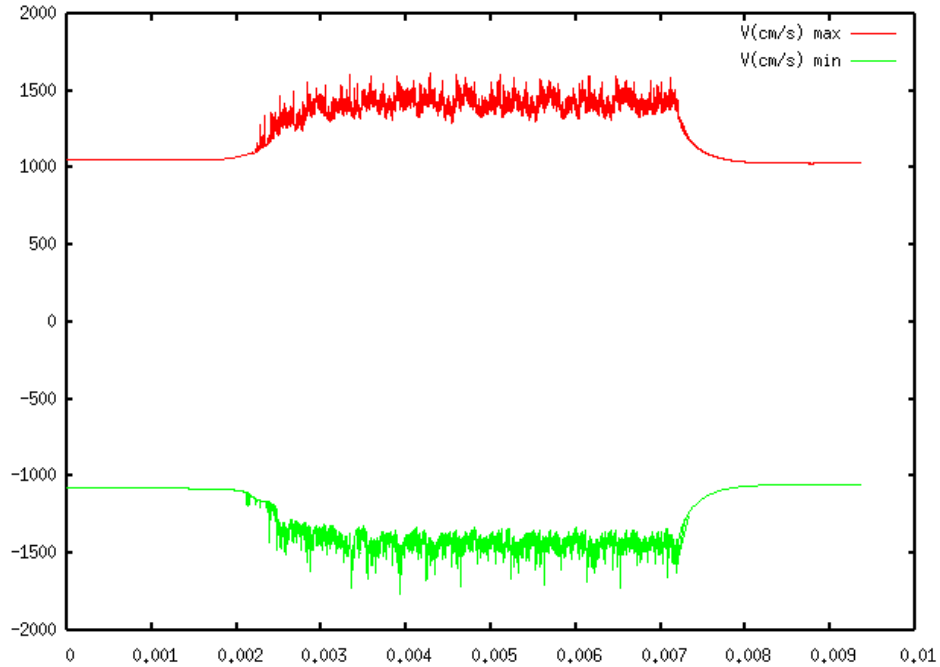


Figure 2.2: Maximum normal velocity at both upper and lower outflow boundary. Corrected boundary conditions are activated at $t=7.10\mu\text{sec}$

The new form of the mass-additive NSCBC ensure that injected particle can pass through the numerical boundaries in a manner that is acoustically transparent. This allows the solver to test a variety of problems and water loading conditions, where droplets do not need to be entirely evaporated as they pass through the numerical boundary. This is very important for turbulent simulations since the local gas velocity will move droplets around in a unpredictable manner, making the location and concentration of the droplets beyond their injection location exceedingly difficult to predict.

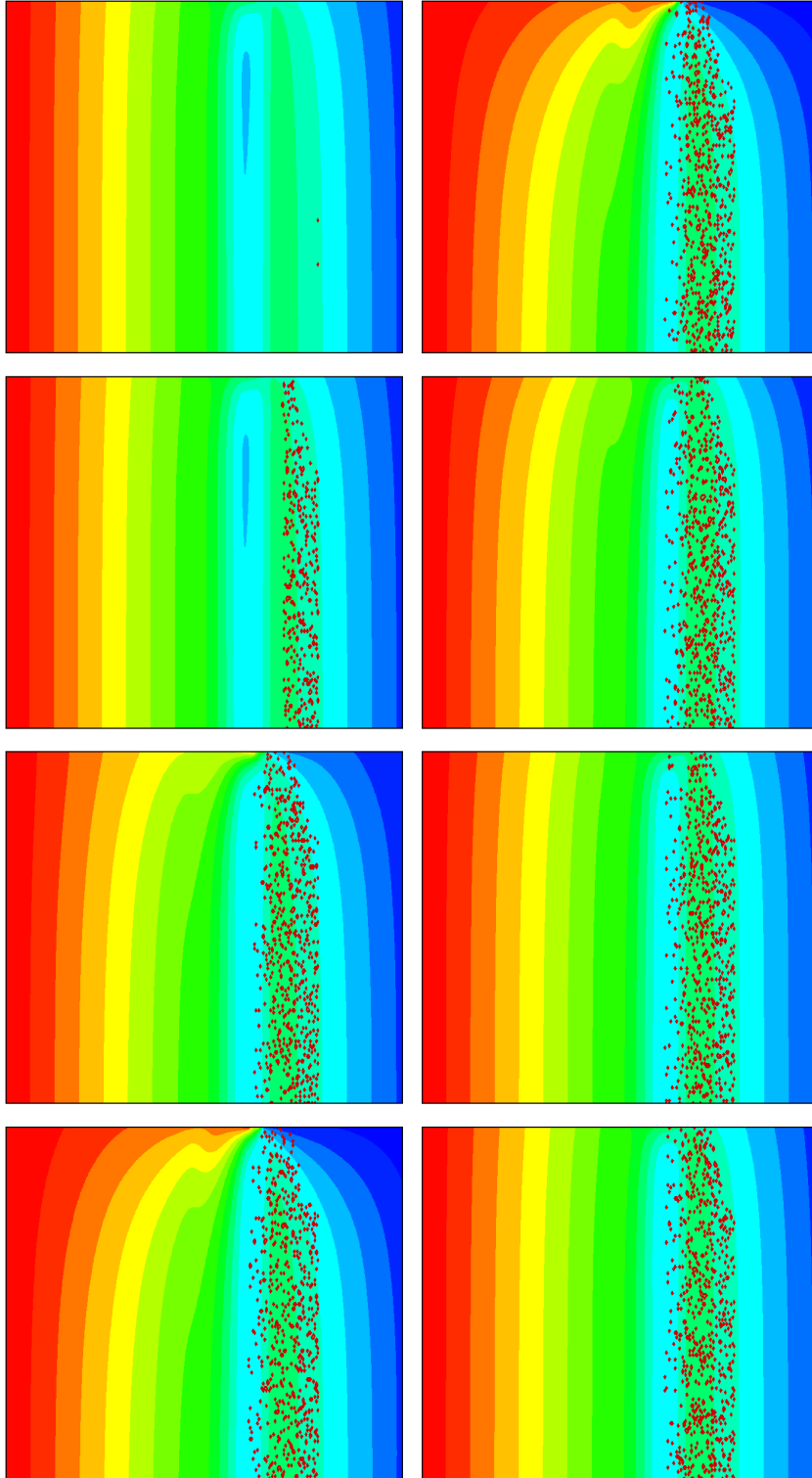


Figure 2.3: x-direction velocity isocontours with droplets, $u|_{x=0} = 230\text{cm/s}$ and $u|_{x=l_x} = -230\text{cm/s}$. From top to bottom, left side, $t=0.01, 1.2, 2.4, 3.6$ μsec . From top to bottom, right side, $t=7.0, 7.1, 8.4, 9.1$ μsec .

2.6 Modified mixture fraction formulation for spray-laden flows

With the addition of water into the domain from the particle-in-cell Lagrangian spray module, mass is no longer locally or globally conserved when we analyze the gas phase. Evaporation will transfer some of the mass, energy and momentum into the gas phase, rendering previous methods for determining a mixture fraction unsuitable. This leads to a problem finding the flame location, since the mixture fraction value is no longer just a function of two streams of fuel and air.

Recent work on three-stream models have been applied to combustion systems, where the third stream of operates as a source of diluent (*Kim et al. (2005), Ihme and See (2011)*). Applying a similar methodology, a three-stream model for the mixture fraction is proposed, comprising of fuel, air and water spray. Unity Lewis number assumption is invoked to equate thermal and mass diffusion, which also makes all proposed models for mixture fraction equivalent. The counterflow configuration is used as the test case for flame injection, where droplets are injected on the fuel and oxidizer side, with preheating to facilitate droplet evaporation and subsequent dilution by water vapor.

Consider the three stream mixing system without chemical reaction characterized by fuel and air (streams 1 and 2 respectively), with the third stream constituting the spray of H₂O. If we represent the mass fraction of some component k in the mixture (a conserved variable) as:

$$Y_k = ZY_{k,1} + \beta Y_{k,2} + \gamma Y_{k,3} \quad (2.20)$$

where the subscripts k, j denote the mass fraction Y of component k in stream j . Z, β, γ are the mixture fraction variables associated with this three-stream formulation. Rewriting the above equation in terms of masses of component k from each

stream, one obtains the following expressions:

$$\frac{m_k}{m} = \frac{m_1}{m_1 + m_2 + m_3} \frac{m_{k,1}}{m_1} + \frac{m_2}{m_1 + m_2 + m_3} \frac{m_{k,2}}{m_2} + \frac{m_3}{m_1 + m_2 + m_3} \frac{m_{k,3}}{m_3} \quad (2.21)$$

$$m = m_1 + m_2 + m_3 \quad (2.22)$$

$$Z = \frac{m_1}{m_1 + m_2 + m_3} \quad (2.23)$$

$$\beta = \frac{m_2}{m_1 + m_2 + m_3} \quad (2.24)$$

$$\gamma = \frac{m_3}{m_1 + m_2 + m_3} \quad (2.25)$$

$$(2.26)$$

With the sum of the mixture fractions being unity, we can express β as:

$$\beta = 1 - Z - \gamma \quad (2.27)$$

If $\gamma = 0$, the problem reduces to the two stream mixing problem, with Z being sufficient to describe mixing of fuel and air streams. In the presence of spray, which constitutes an additional mass source, it is inadequate to represent the system in terms of only one mixing variable Z , as conservation of mass is violated.

Consider the mixing problem with stream 1 constituting fuel F , stream 2 constituting air (O_2, N_2 as components), and stream 3 constituting water. Let L represent the advection-diffusion operator given by:

$$L(\phi) = \frac{\partial \rho \phi}{\partial t} - \frac{\partial}{\partial x_j} (\rho u_j \phi) - \frac{\partial}{\partial x_k} (\partial D_k \frac{\partial \phi}{\partial x_j}) \quad (2.28)$$

Note that for the present analysis, $D_k = D$ for all k , with a unity Lewis number assumption for all species. Diagnostic tests on a unity L_e flame demonstrate that within this framework, all the mixture fraction definitions proposed give identical results, and may be seen as validating the models proposed. In a non-unity L_e

framework, the models proposed are seen to deviate from each other, but the deviations observed may be considered acceptably small insofar as concerning diagnostic integrity. The transport equations for each species in the mixing problem can be written as:

$$\begin{aligned}
L(Y_F) &= 0 \\
L(Y_{O_2}) &= 0 \\
L(Y_{N_2}) &= 0 \\
L(Y_{H_2O}) &= \psi_\rho
\end{aligned} \tag{2.29}$$

In equation (2.29) the source term of water ψ_ρ is non-zero, and represents the mass addition from injection. We propose conserved scalars for various diagnostics (this becomes pertinent when there is combustion). Quantities of interest in terms of mixing variables proposed in equation 2.27 can be expressed as:

$$\left. \begin{aligned}
Y_F &= ZY_{F,1} \\
Y_{O_2} &= (1 - Z - \gamma)Y_{O_2,2} \\
Y_{N_2} &= (1 - Z - \gamma)Y_{N_2,2} \\
Y_{H_2O} &= \gamma \text{ (since } Y_{H_2O,3} = 1 \text{)}
\end{aligned} \right\} \begin{aligned}
&\Rightarrow L(Z) = 0 \\
&\Rightarrow L(\gamma) = \psi_\rho
\end{aligned} \tag{2.30}$$

and

$$\begin{aligned}
Z &= \frac{Y_F}{Y_{F,1}} \\
\gamma &= Y_{H_2O}
\end{aligned} \tag{2.31}$$

In a reacting framework, mixture fraction can be defined by identifying conserved quantities and reconstructing the mixture fraction Z accordingly, such that it is unity in the fuel stream and zero in the oxidizer stream. An expression for γ will also be derived. A simplifying approximation that is employed is that during chemical reaction, the main components are CO_2 and H_2O . It will be shown from tests that such an assumption is perfectly justified.

Assume that the fuel under consideration has the form C_nH_m . Recognizing that

atomic carbon mass Y_C is a conserved quantity, a conserved scalar Z satisfying the sought boundary conditions is expressed as:

$$Z = \frac{Y_C}{Y_{C,1}} \quad (2.32)$$

with

$$\begin{aligned} Y_C &= \left(\frac{nM_C}{M_{C_nH_m}} \right) Y_{C_nH_m} + M_C/M_{CO_2} Y_{CO_2} \\ L(Z) &= 0 \\ Z &= 1 \text{ in stream 1} \\ Z &= 0 \text{ in stream 2} \end{aligned} \quad (2.33)$$

However, note that Y_H and Y_O are not conserved because of addition from the water stream.

$$\begin{aligned} Y_H &= \left(\frac{mM_H}{M_{C_nH_m}} Y_{C_nH_m} \right) + \left(\frac{2M_H}{M_{H_2O}} \right) Y_{H_2O} \\ L(Y_H) &= \left(\frac{2M_H}{M_{H_2O}} \right) \psi_\rho \end{aligned} \quad (2.34)$$

Likewise one may write

$$\begin{aligned} Y_O &= Y_{O_2} + \left(\frac{2M_O}{M_{CO_2}} \right) Y_{CO_2} + \left(\frac{M_O}{M_{H_2O}} \right) Y_{H_2O} \\ L(Y_O) &= \left(\frac{M_O}{M_{H_2O}} \right) \psi_\rho \end{aligned} \quad (2.35)$$

Expressions for γ may now be obtained by removing the portion of H_2O that comes from chemical reaction. This will be the mass fraction of the third stream that consists entirely of water.

$$\gamma = \left(\frac{M_{H_2O}}{2M_H} \right) Y_H - \left(\frac{mM_{H_2O}}{2nM_C} \right) Y_C \quad (2.36)$$

with

$$\begin{aligned} L(\gamma) &= \psi_\rho \\ \gamma &= 0 \text{ in stream 1 and 2} \\ \gamma &= 1 \text{ in stream 3} \end{aligned} \quad (2.37)$$

Expressions for Y_C , Y_H and Y_O in terms of Z and γ are expressed as:

$$Y_C = ZY_{C,1} \quad (2.38)$$

$$Y_H = ZY_{H,1} + \gamma Y_{H,3} \quad (2.39)$$

$$Y_O = (1 - Z - \gamma)Y_{O,2} + \gamma Y_{O,3} \quad (2.40)$$

The stoichiometric flame location is computed in conformity with Bilger's approach (*Bilger (1977)*). For global chemistry, it is assumed that the oxygen mass fraction at the flame is dependent only on the amounts of CO_2 , H_2O and molecular oxygen O_2 :

$$Y_O = Y_{O_2} + \left(\frac{2M_O}{M_{CO_2}}\right) Y_{CO_2} + \left(\frac{M_O}{M_{H_2O}}\right) Y_{H_2O} \quad (2.41)$$

We can replace eliminate the product mass fractions by utilizing Eqns. 2.33 and 2.34 to obtain

$$2\frac{Y_C}{M_C} + \frac{Y_H}{2M_H} - \frac{Y_O}{M_O} = 6\frac{Y_{C_2H_4}}{M_{C_2H_4}} - \frac{Y_{O_2}}{M_O} \quad (2.42)$$

Eqn. 2.42 can lead to both a corrected mixture fraction variable as well as to the stoichiometric criteria. By using eqns. 2.38, 2.39, and 2.40 and using the left hand side of eqn. 2.42, we obtain

$$\begin{aligned} 2\frac{Y_C}{M_C} + \frac{Y_H}{2M_H} - \frac{Y_O}{M_O} &= Z\frac{Y_{C,1}}{M_C} + \frac{ZY_{H,1} + \gamma Y_{H,3}}{2M_H} \\ &+ \frac{(1 - Z - \gamma)Y_{O,2} + \gamma Y_{O,3}}{M_O} \end{aligned} \quad (2.43)$$

We can now derive an expression for the mixture fraction variable Z , using the relation between hydrogen and oxygen mass fraction from the third stream $Y_{H,3}/M_H = 2Y_{O,3}/M_O$.

$$Z_{Bilger} = \frac{\frac{2Y_C}{M_C} + \frac{Y_H}{2M_H} - \frac{Y_O}{M_O} + (1 - \gamma)\frac{Y_{O,2}}{M_O}}{\frac{2Y_{C,1}}{M_C} + \frac{Y_{H,1}}{2M_H} + \frac{Y_{O,2}}{M_O}} \quad (2.44)$$

Eqn. 2.42 can also be used to find the stoichiometric location. Since fuel and oxidizer are completely consumed, eqn. 2.42 leads to the stoichiometric criterion

$$2\frac{Y_C}{M_C} + \frac{Y_H}{2M_H} - \frac{Y_O}{M_O} = 0 \quad (2.45)$$

The stoichiometric condition can be found numerically by searching for the location that satisfies 2.45. This mixture fraction formulation was tested by injecting droplets from the oxidizer side of a counterflow diffusion flame configuration such that spray is injected only on the lower half of the domain. The water loading parameter is defined as:

$$WLP = \frac{\text{energy used to evaporate droplets to steam}}{\text{initial flame power}} \quad (2.46)$$

A variety of loading tests were conducted, and the case of WLP= 25% was selected for reporting. Thermal and mass diffusion was set equal by setting the Lewis numbers equal to 1. Table 2.5 shows the isocontours of temperature, uncorrected and corrected mixture fraction variables.

The uncorrected, two-stream method for the mixture fraction and stoichiometric composition is shown to incorrectly capture the flame location, leading to incorrect evaluation of important scalar quantities. This is observed when the plot of temperature vs. mixture fraction (corrected and uncorrected) is presented (2.4). With the uncorrected mixture fraction formulation and criteria, there would be an underestimate of the flame temperature by hundreds of degrees Kelvin. It can also be observed that the improved mixture fraction formulation and criterion correctly captures the temperature behavior near the traditional $Z_{st} = 0.0673$ for ethylene-air combustion.

While Z_{st} will change slightly due to the loading from water spray, the change is both minute and immaterial, since our criterion looks for a very specific balance of elemental mass fractions of carbon, hydrogen, and water.

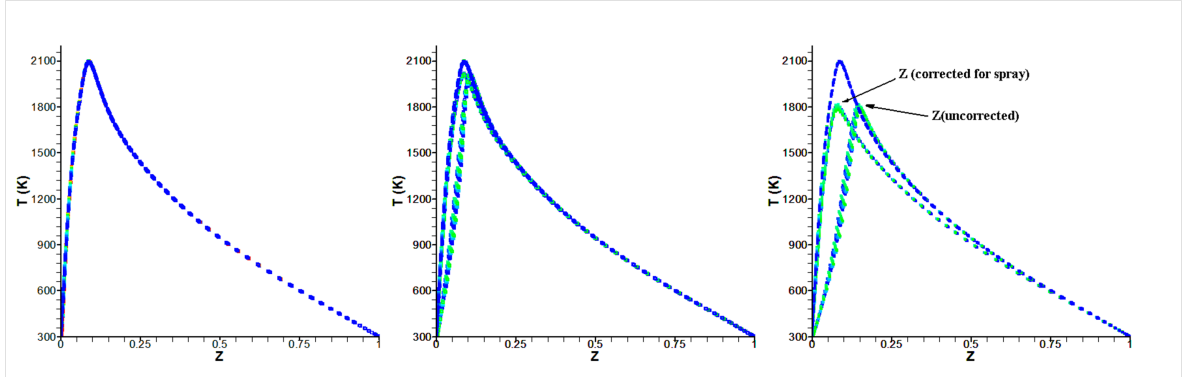


Figure 2.4: Scatter plot of temperature vs Z . Outer blue mixture fraction corresponds to domain not affected by spray. From left to right, $t=0.9, 1.7, 2.8 \mu\text{sec}$.

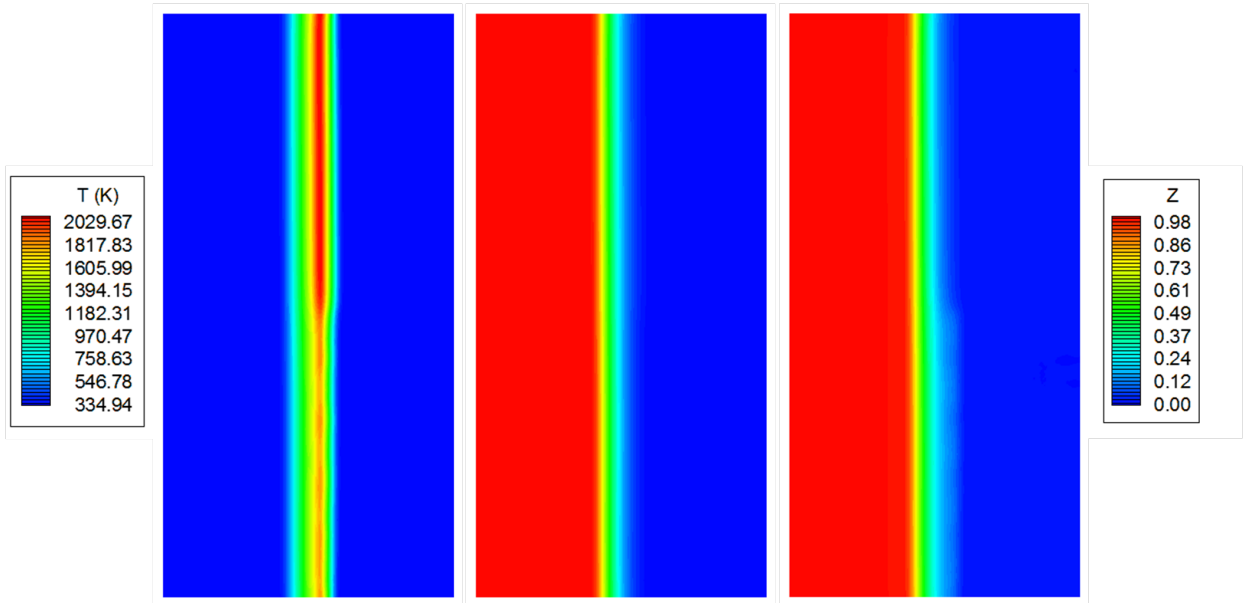


Figure 2.5: Temperature, uncorrected and corrected mixture fraction variables at $t=2.8 \mu\text{sec}$.

2.7 Concluding Remarks

A numerical framework, composed of improved characteristic boundary conditions for mass-additive systems and analytical tools for determining flame location, is presented. The framework addresses challenges associated with the lack of acoustic transparency of the numerical boundary when droplets begin to interact with the fluid at the boundary. The single spray droplet case shows an abnormally large acceleration when the droplet begins to interact with the outflow boundary. It was shown that the corrected boundary condition allows the droplet to pass without producing adverse effects to the velocity field, as compared to the uncorrected single-droplet test.

To further demonstrate the capabilities of the improved boundary condition, a counterflow diffusion flame case with significant spray loading was performed. This case demonstrated that the transverse velocity can be significantly distorted when the spray zone thickness is large. Subsequent correction of the Navier-Stokes Characteristic Boundary Conditions allow for a smooth solution of the velocity vectors at the boundary. Isocontours of velocity as well as time history plots of minimum and maximum pressure provide evidence of successful boundary treatment.

Finally, a three-stream mixture fraction formulation was introduced and validated under direct numerical simulation of laminar counterflow diffusion flames, accurately capturing the flame location. The formulation provides a methodology for tracking the elemental composition of the gas phase provided by fuel, air, and spray sources. Plots of the mixture fraction contours under spray loading demonstrate significant deviation from steady state. In addition, plots of temperature versus mixture fraction indicate that deviation results in significant underestimation of the flame temperature. The three-stream mixture fraction accurately captures the flame temperature and preserves the mixture fraction profile from significant deviation.

The numerical framework allows for more a more complex study of flame extinction

under hostile quenching conditions. The following chapter utilizes the numerical framework developed thus far to answer fundamental questions about the nature of turbulence and spray laden interactions, and attempts to create a unified extinction criterion that captures aerodynamic and thermal quenching.

CHAPTER III

Turbulence and spray induced quenching

3.1 Introduction

This chapter presents a science study of the physical processes responsible for flame extinction due to evaporating water spray by means of detailed numerical simulations. The problem is of practical interest in fire safety applications, in which utilization of fine water droplets is considered a more effective means of flame suppression. In particular, we attempt to develop a unified criterion for flame extinction that extends the classical extinction strain-rate condition to include non-adiabatic configurations in which additional flame weakening arises from heat losses due to evaporative cooling or thermal radiation. It is recognized that flame extinction occurs from combined effects of strain, preferential diffusion, and heat losses, such that the corresponding extinction condition for nonpremixed laminar flames, usually given by the critical scalar dissipation rate, needs to be appropriately modified to account for other external flame weakening effects. Recent studies (*Wang and Trouve (2006)*, *Narayanan and Trouve (2009)*) addressed this issue for a flame subjected to radiative cooling by a solid wall. The present study extends and complements this work by considering water spray evaporation, and showcases our recent developments in combustion DNS coupled with Lagrangian spray dynamics (*Wang and Rutland (2007)*).

The adopted model problem configuration consists of laminar and turbulent coun-

terflow nonpremixed flames of ethylene and air, interacting with monodisperse dilute water spray injected from the air stream side of the flame. Details in the computational development of the problems are described in Chapter 2, part of which was published in *Arias et al. (2010)*, which includes a conservative treatment of coupling between Lagrangian spray droplets and the Eulerian gas-phase fluid dynamics, and modified characteristic boundary conditions to account for spray evaporation effects. In this study, test cases at various droplet loading conditions and strain rates are analyzed in terms of a theoretically developed extinction criterion in order to quantify the level of flame weakening and the onset of extinction.

3.2 A Unified Extinction Criterion

According to laminar flame theory (*Linán (1974), Peters (1983)*), flame extinction occurs when the flow residence time becomes shorter than a critical limit below which intense chemical reactions are not sustainable. For nonpremixed flames, such a condition is identified by the extinction strain rate, or more formally by the scalar dissipation rate based on the mixture fraction variable. Although the extinction scalar dissipation rate is considered a unique property of a fuel-air mixture under a given initial enthalpy condition, studies of flames with radiative heat losses (*Chao et al. (1990), Wang et al. (2007)*) reported dual extinction limits, the lower of which is induced by the flame weakening due to the heat loss. Following the asymptotic theory (*Linán (1974), Peters (1983)*), this leads to the reduced Damkhler number, δ , which follows the scaling relation at leading order as:

$$\delta \sim \frac{\exp(-T_a/T_{st})}{\chi_{st}} \quad (3.1)$$

where T_a is the activation temperature, T_{st} and χ_{st} are the flame temperature and scalar dissipation rate at the stoichiometric location. Extinction occurs if δ falls

below a critical extinction limit. The reduced Damkhler number represents the ratio of the characteristic flow time to the chemical time, such that extinction condition is reached either by reduced flow residence time (χ_{st}^{-1}) or by reduced chemical reactivity ($\exp(-T_a/T_{st})$). Recalling the dual extinction limits (*Wang et al. (2007)*, *Chao et al. (1990)*), the upper limit corresponds to the strain induced extinction, while the lower limit is primarily due to the suppressed chemical reactivity due to the large radiative heat loss. The weakening of chemical reactivity may also be caused by other physical processes, such as evaporative cooling of water spray (the subject of the present study); all of these flame weakening effects are manifested by the reduced flame temperature.

The above discussion suggests that various extinction mechanisms may be described by a unified extinction criterion, referred to as the flame weakness factor, defined as:

$$R = \frac{\chi_{st}}{\chi_{st,ext}} \frac{\exp(-T_a/T_{st,ext})}{\exp(-T_a/T_{st})} \quad (3.2)$$

where subscripts *ext* denotes the values at the extinction condition of the corresponding adiabatic flame. The general extinction condition is identified as $R > 1$. Note that such a simple description is based on a number of assumptions, such as a one-step global reaction with Arrhenius kinetics and unity Lewis numbers. A similar form of Eq. (2) has been adopted in the study of turbulent flame-wall interaction *Wang and Trounev (2006)*, and laminar ethylene flames with radiative heat losses (*Narayanan et al. (2009a)*). The present study investigates the validity of the approach in identifying laminar and turbulent ethylene-air flame extinction by water spray evaporation.

3.3 Problem Configuration

Figure 3.1 shows the flame configuration under study. The flow configuration corresponds to a two dimensional, laminar and turbulent counterflow flames with ethylene-air chemistry. A reduced chemical mechanism based on the directed-relation graph technique *Lu and Law (2005)* was adopted. The mechanism consists of 19 major species, 10 quasi-steady species, and 167 reaction steps.

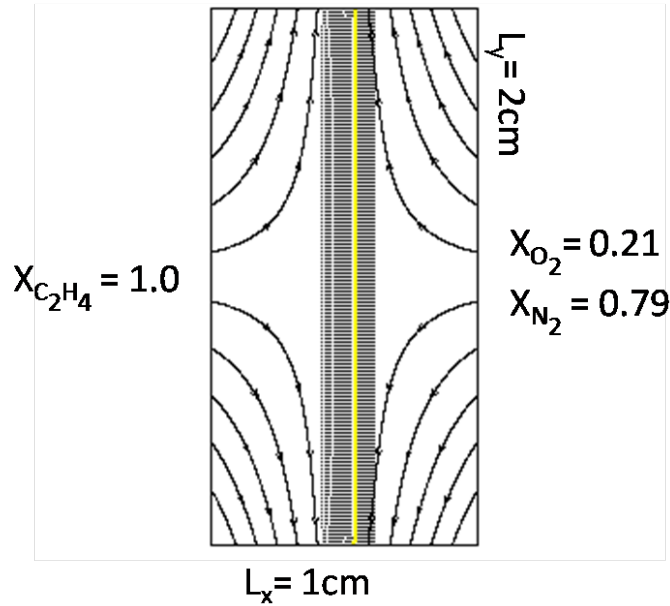


Figure 3.1: Counterflow flame configuration. Solid lines denote potential flow streamlines. Dotted lines represent temperature contours. Solid yellow line indicates the stoichiometric mixture fraction demarcating the flame location.

The domain size was 1cm x 2cm with 600x800 grid points in the x and y directions. The inlet temperature and pressure were at 300K and 1 atm. The steady counterflow diffusion flame was initialized first by overlaying the 1-D solution from OPPDIF (*Lutz et al. (1996)*) onto the 2-D domain, and temporally evolving the solution until it reached a steady state. Subsequently, water spray droplets of 10 μm size diameters were injected at 1mm distance from the flame on the oxidizer side, matching the local gas x-directional gas speed at injection location. Laminar flame tests were conducted with two different strain rates. For the turbulent cases, homogeneous

isotropic turbulence was injected at both inlets by first generating an auxiliary 2-D field using a prescribed energy spectrum, which was then translated from the space domain into the time domain by using the Taylor hypothesis.

The DNS solver employs high order central differencing and explicit time integration for compressible reacting flow equations *Im et al.* (2007). The spray droplets are treated on a Lagrangian formulation (*Wang and Rutland* (2007)), where the drag force is derived by the Stokes law, and the thermal conductivity is assumed infinite inside the droplet. The Lagrangian particles are coupled to the Eulerian gas equations through the mass, momentum and energy source terms associated with water evaporation (*Wang and Rutland* (2007), *Arias et al.* (2010)). Improved characteristic boundary conditions were also developed to account for spray evaporation effects at the outflow boundaries (*Arias et al.* (2010)).

As for the diagnostics, the consideration of the additional water stream due to spray evaporation required a modified formulation of the mixture fraction variables and state-relationships, details of which are described in *Narayanan et al.* (2009b). In applying Eq. (2) as the extinction criterion, the global activation energy, T_a , for the ethylene-air flame was determined following the method of *Sun et al.* (1999), and was found to be 18,692 K. For the nonpremixed flame considered, the extinction scalar dissipation rate for the adiabatic flame without spray was at $\chi_{st,ext} = 116s^{-1}$, and the temperature at extinction $T_{st,ext}$, was found to be 1745 K.

3.4 Results

3.4.1 Laminar Flames

Table 3.1 shows the three laminar cases under study. The scalar dissipation rate and the specific flame power (average heat release rate per unit flame area) are based on the initial steady state diffusion flame. The water loading parameter (WLP) is

the actual amount of water evaporated normalized by the initial flame power. In case there is a significant temporal variation in WLP, the maximum attainable value was used. Flame extinction was observed for Cases B and C only; for Case A, both fluid dynamic strain and water loading were not sufficient to quench the flame.

Case	χ_{st}	Specific flame power	WLP (%)
A	$13.3s^{-1}$	$400kW/m^2$	7.5%
B	$13.3s^{-1}$	$400kW/m^2$	18.0%
C	$24.5s^{-1}$	$600kW/m^2$	11.5%

Table 3.1: Parameters used for three laminar test cases.

Figure 3.2 shows a temporal evolution of flame quenching by water spray, for Case B. As the injected water spray approaches the reaction zone, the heat release rate is locally reduced. The spray is monodisperse and is spatially uniformly distributed, such that the flame weakening is also uniformly spread along the flame. Therefore, the analysis of a representative flame history was conducted along the flame location at the midpoint of the flame.

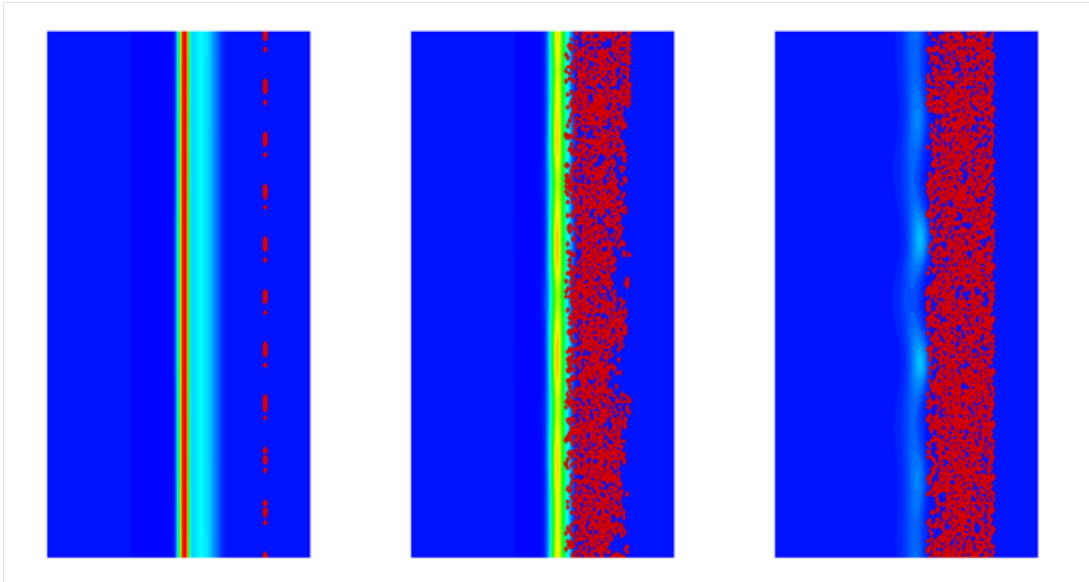


Figure 3.2: Heat release rate isocontours with spray overlay (red dots) for Case B at $t = 0.3, 5.7, 6.2$ ms.

Figure 3.3 shows the temporal history of the Integrated Heat Release Rate (IHR)

(in kW/m²) at the center point of the flame location line and the flame weakness factor, R , for the three simulation cases. The flame in Case A is subjected to a very small value of R , and no extinction occurs. For Cases B and C, an abrupt drop in IHR coincides with an increase in R value above unity. Therefore, it is qualitatively found that the $R = 1$ criterion appropriately identifies the onset of flame extinction.

To further examine if the extinction criterion captures the local extinction events, Figure 3.4 shows an instantaneous image of the normalized scalar dissipation rate ($\chi_{st}/\chi_{st,ext}$), IHR, and R distribution along the flame surface (represented by the stoichiometric mixture fraction line), for Case B at $t = 5.9$ ms, which is approximately at the onset of local extinction event. The results further demonstrate that the peaks in the R factor accurately identifies the local IHR minima, thus providing correct information to detect extinction points. On the other hand, the normalized scalar dissipation rate shows little variation across the entire flame surface. Therefore, Figures 3.3 and 3.4 show that the R factor serves as a valid metric to determine the level of flame weakening and subsequent extinction.

3.4.2 Turbulent Flames

Based on the reference laminar flame studies, two-dimensional turbulent flame simulations were conducted. The steady laminar flame for Case C (at $\chi_{st} = 24.5s^{-1}$) was used as the initial condition, on which homogeneous turbulent flow was created and injected at both inlet boundaries. As for the turbulence parameters, the integral length scale (L_{11}) was 0.5 cm, and the turbulence intensity was 0.85 times the mean inlet velocity, such that the turbulent Reynolds number was 654. The turbulence parameters were selected such that turbulent eddies are strong enough to cause strain-induced extinction at some flame locations. A second simulation was run with exactly identical turbulent conditions and an additional spray injection was imposed at $WLP = 20\%$. By comparing the two simulation data sets, the additional flame weakening

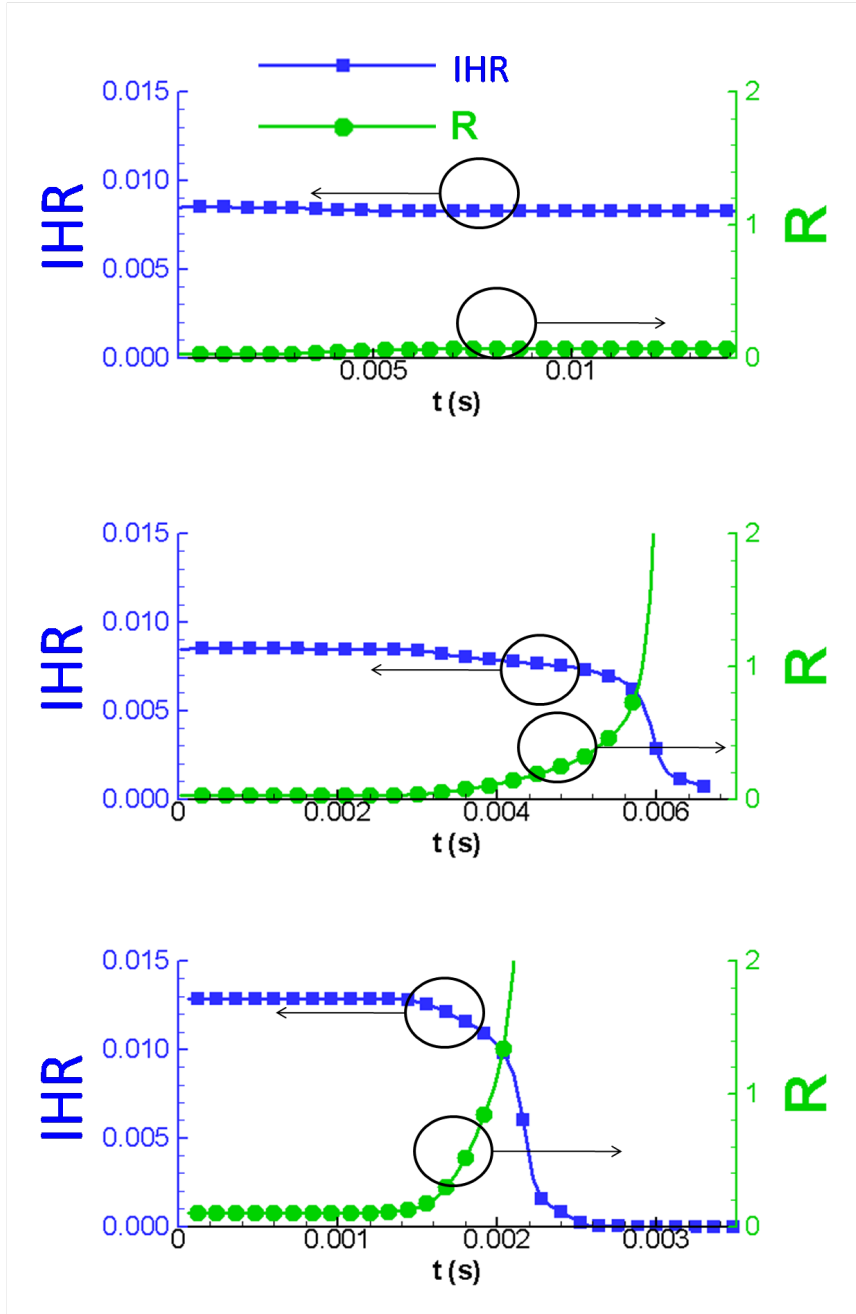


Figure 3.3: Temporal history of integrated heat release rate and weakness factor at the midpoint of the flame, for the three cases considered.

by spray can be clearly identified.

Figure 3.5 shows the temporal evolution of the heat release rate isocontours as the turbulent flow interacts with the planar flame. At 4.1ms, the turbulence-induced strain enhances mixing, resulting in a temporary increase in heat release rate. Further

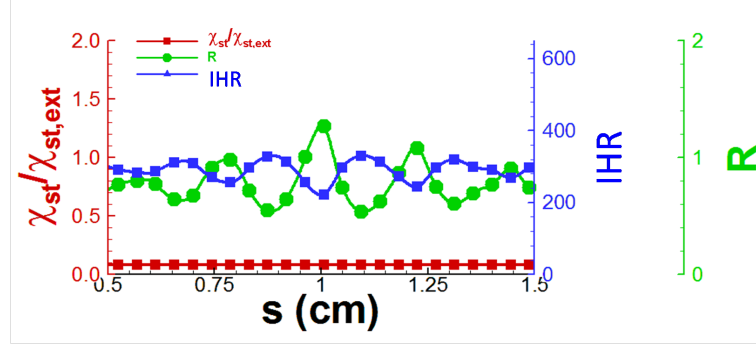


Figure 3.4: Spatial distribution of normalized scalar dissipation rate, integrated heat release rate and the weakness factor along the flame surface for Case B at $t = 5.9$ ms.

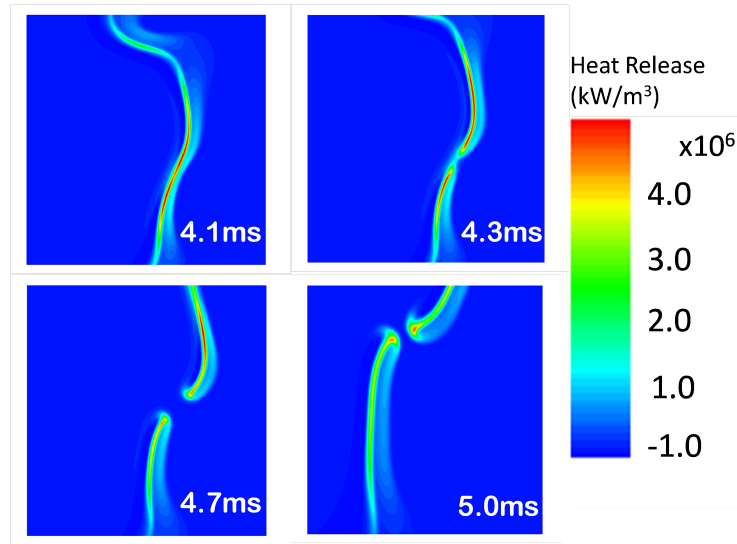


Figure 3.5: Temporal evolution of heat release rate isocontours for turbulent flame simulation without spray.

increase in the local scalar dissipation rate creates an extinction event, with two visible edge flame structures at 4.7 ms. After the local extinction, the local strain rate decays and the two edge flames propagate onto each other along the stoichiometric line, recovering a connected flame structure at 5.1 ms.

Figure 3.6 shows the spatial distribution of the normalized scalar dissipation rate, IHR, and R along the flame surface for the four instantaneous moments shown in Figure 5. Since the actual flame length is longer than the domain length, only a length of 2 cm along the stoichiometric flame line capturing the extinction event is

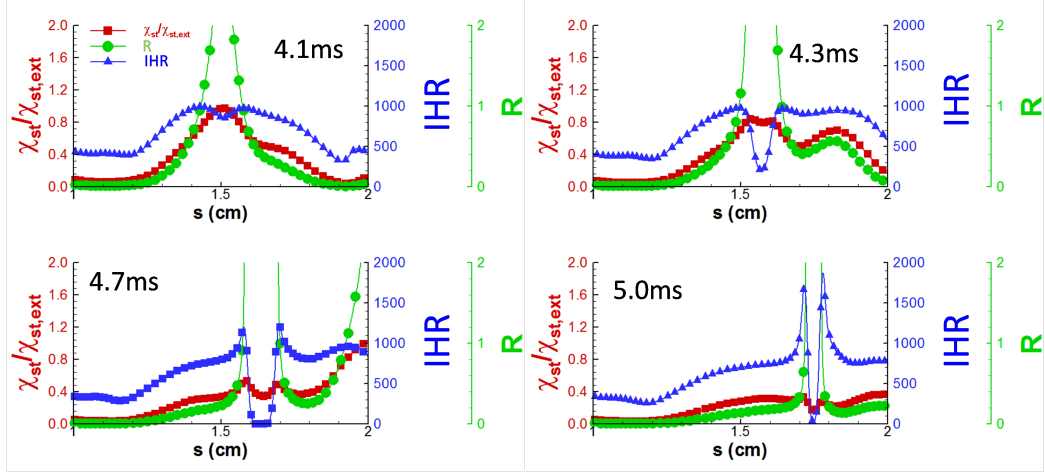


Figure 3.6: Distribution of the normalized scalar dissipation rate, integrated heat release rate (kW/m^2) and the weakness factor for the turbulent flames without spray at the four times shown in Fig. 3.5

shown for comparison. At 4.1 ms, a moderate increase in IHR is shown, along with the R factor increasing above unity, indicating that a subsequent extinction event is imminent. At two subsequent times, a large peak in R appears as the local heat release rate drops to exhibit extinction event. On the other hand, the normalized scalar dissipation rate remains lower than unity throughout the entire event. Once the local extinction occurs and the two distinct edge flames form (noticeable at 5.1 ms), IHR peaks indicate that the local heat release rate is significantly higher than that of the original laminar flame. This is due to the typical edge flame behavior that the burning characteristics at the edge is closer to those of a stoichiometric premixed flame, exhibiting a peak heat release rate that is substantially higher than that in the trailing diffusion flame branch (*Im and Chen (1999)*).

Figures 3.7 and 3.8 show similar four instantaneous images and corresponding distribution along the flame surface for the turbulent flames with spray. The initial local extinction point is identified to be the same as in no-spray case, but this time the two edge flames retreat from each other, leading to a total extinction of the entire flame. This is due to the additional flame weakening provided by the spray evaporation. The additional flame weakening is further evidence in Figure 3.8 (at 4.2

ms) in that the IHR peaks representing the two flame edges show the heat release values much lower than those in the previous case without spray. Again, $R = 1$ appears to serve as an accurate criterion to predict imminent local extinction (at 3.7 ms), while the scalar dissipation rate no longer provides any meaningful information about the state of the flame strength.

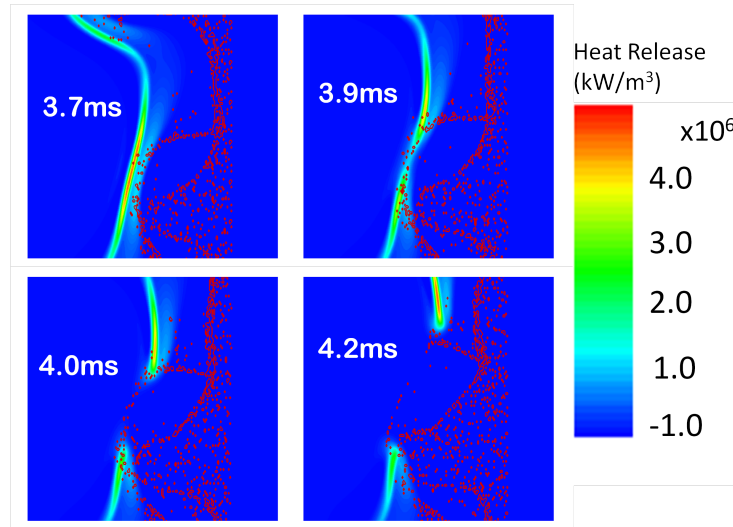


Figure 3.7: Temporal evolution of heat release rate isocontours for turbulent flame simulation without spray.

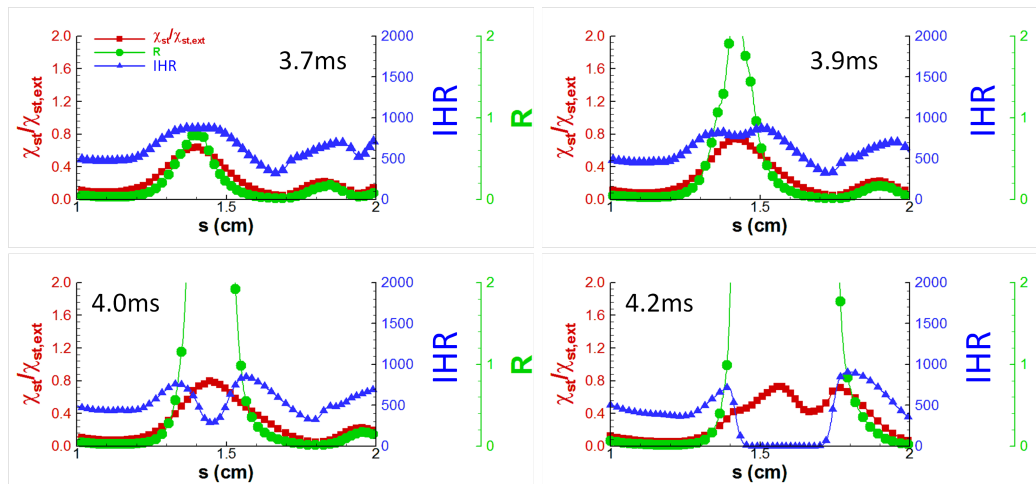


Figure 3.8: Distribution of the normalized scalar dissipation rate, integrated heat release rate (kW/m^2) and the weakness factor for the turbulent flames with spray at the four times shown in Fig. 3.7

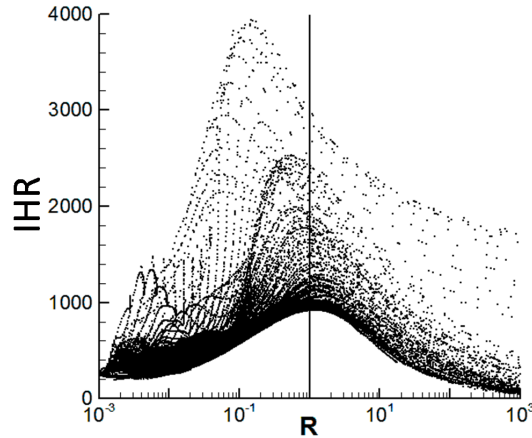


Figure 3.9: Turbulence without spray case; integrated heat release rate (kW/m^2) versus weakness factor along the stoichiometric mixture fraction lines for cumulative data over the simulation time. The vertical line denotes the $R = 1$ condition.

In the context of turbulent combustion modeling, statistical data for the R factor distribution in turbulent flames are investigated. Figures 3.9 and 3.10 show the time-cumulative scatter plot of IHR versus R factor along the stoichiometric line for the turbulent flame case without and with spray, respectively. For $R < 1$, the flame strength increases with an increase in R . This is a weak strain (high Damköhler number) regime of the flames in which a higher strain rate provides more reactants to the flame, thereby enhancing the burning intensity. The $R = 1$ line is the suggested extinction condition, but there are surprisingly a large number of data points to indicate that the flame segments have finite heat release rate at R above extinction limit. This is a manifestation of transient flame dynamics; instantaneous snapshots of highly transient turbulent flames can show the weakening (and eventually extinguishing) flamelet segments as a combustion pocket at finite reaction rate. Note that the $R = 1$ criterion is still a valid metric to predict the local extinction event. However, the probability density of the local heat release rate distribution in highly turbulent flames may exhibit a more continuous spectrum in terms of the flame weakness factor.

Finally, the scattered data points at IHR values much higher than the initial spe-

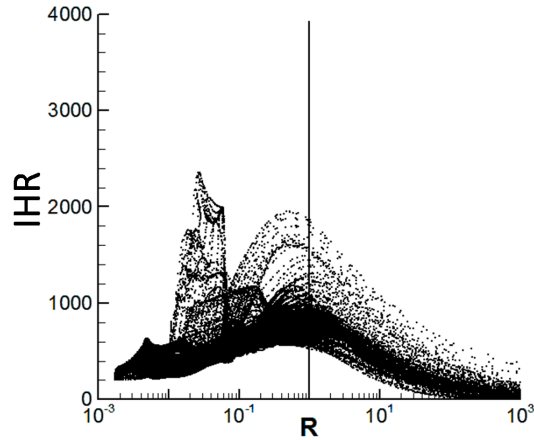


Figure 3.10: Turbulence with spray case; integrated heat release rate (kW/m^2) versus weakness factor along the stoichiometric mixture fraction lines for cumulative data over the simulation time. The vertical line denotes the $R = 1$ condition.

cific flame power ($600 \text{ kW}/\text{m}^2$) in Figure 3.9 correspond to the flame edges produced upon local quenching. As discussed above, the enhanced burning due to the edge formation is significantly reduced in the presence of water spray (Figure 3.10).

3.5 Concluding Remarks

High-fidelity simulations were conducted to investigate local extinction encountered in turbulent nonpremixed ethylene-air flames interacting with fine water spray. A unified extinction criterion is proposed to account for both strain-induced flame weakening and the flame cooling due to water droplet evaporation. In two dimensional laminar and turbulent flame cases under study, the proposed weakness factor R served as an excellent quantitative metric to detect the local extinction event.

Two turbulent simulations, with and without spray injection, allowed direct comparison of two realistic turbulent flame quenching events by highlighting the additional flame weakening effects due to spray evaporation. Formation of edge flames was observed, and their subsequent evolution leading to the flame recovery or total

extinction were found to depend strongly on the temporal history of the local strain rate as well as the presence of the spray droplets. The cumulative temporal data for the local flame heat release rate versus the weakness factor showed two distinct regimes, the weak stretch regime in which the burning intensity increases with R and the extinction regime in which highly transient extinguishing flamelets exhibit lower yet finite heat release rate at R values significantly higher than unity. The large enhancement in the local heat release rates in some flame segments were attributed to the edge flame formation, which was significantly suppressed by the additional flame weakening in the presence of water spray.

CHAPTER IV

Dynamics of soot formation using MOMIC approach

4.1 Introduction

The purpose of this study is to provide a numerical framework for the high-fidelity simulation of soot. A comprehensive review of the mathematical restrictions on the evolution of the soot statistics and numerical artifacts that appear as a consequence of fractional order moment interpolation is provided. Proposed solutions to these problems are tested in the context of 1-D numerical simulation of diffusion flames.

The soot model implemented is a sixth-order MOMIC. S3D is utilized as the flow solver. The conservation of gas phase is rigorously enforced feedback mechanisms related to soot formation and oxidation.

4.2 Soot Moments: Method of Moments with Interpolative Closure

In this study, the soot is described by a discrete Particle Size Distribution Function (PSDF), with $N_k(M, t)$ describing the number of k carbon atoms contained particles at a given location $M = (x_1, \dots, x_i)$ of space. The temporal rate of change of the

discrete PSDF, is described by the General Dynamic Equation (GDE) for each class N_k :

$$\begin{aligned} \frac{\partial N_k}{\partial t} + \nabla \cdot N_k \vec{U} = & \nabla \cdot D_k \nabla N_k + \nabla \cdot \vec{U}_T N_k + \left[\frac{\partial N_k}{\partial t} \right]_{growth} + \left[\frac{\partial N_k}{\partial t} \right]_{nucleation} + \\ & \left[\frac{\partial N_k}{\partial t} \right]_{coagulation} + \left[\frac{\partial N_k}{\partial t} \right]_{oxidation} \end{aligned} \quad (4.1)$$

The thermophoretic velocity \vec{U}_T , is induced by temperature gradients, driving the particles from higher to lower temperature regions and is represented by:

$$\vec{U}_T = -\frac{3\nu}{4(1 + \frac{\pi\alpha}{8})} \nabla T \quad (4.2)$$

This expression holds for particles in the free molecular regime and denotes that the thermophoresis velocity is independent of the particle size.

The diffusion coefficient D_k is defined by the Stokes-Einstein expression for the coefficient of diffusion:

$$D_k = \frac{k_B T}{f} \quad (4.3)$$

where f is the friction coefficient and depends of the regime of the particle. In the free molecular regime, f is expressed by:

$$f = \frac{2}{3} d_k^2 \rho \left(\frac{2\pi k_B T}{m} \right)^{\frac{1}{2}} \left[1 + \frac{\pi\alpha}{8} \right] \quad (4.4)$$

where ρ represents the gas-phase density and m represents the mixture molecular weight.

4.1 can be expressed in Cartesian coordinates:

$$\frac{\partial N_k}{\partial t} + \frac{\partial}{\partial x_i} (U_i N_k) = \frac{\partial}{\partial x_i} \left(D_k \frac{\partial N_k}{\partial x_i} \right) - \frac{\partial}{\partial x_i} (U_{T,i} N_k) + \dot{N}_k \quad (4.5)$$

where \dot{N}_k includes nucleation, coagulation, surface growth, and oxidation.

Soot particles are assumed to be carbon spheres with a constant density ρ_s . For each class of particle k , the number of contained carbon atoms is denoted by m_k . Multiplying 4.5 by m_k^r with $r \geq 0$, and summing for all k particle classes gives:

$$\begin{aligned} \frac{\partial}{\partial t} \left(\sum_{k=1}^{\infty} m_k^r N_k \right) + \frac{\partial}{\partial x_i} \left(U_i \sum_{k=1}^{\infty} m_k^r N_k \right) &= \frac{\partial}{\partial x_i} \left(\sum_{k=1}^{\infty} m_k^r D_k \frac{\partial N_k}{\partial x_i} \right) \\ &- \frac{\partial}{\partial x_i} \left(U_{T,i} \sum_{k=1}^{\infty} m_k^r N_k \right) + \sum_{k=1}^{\infty} m_k^r \dot{N}_k \end{aligned} \quad (4.6)$$

The soot moment of order r is denoted as M_r and is expressed as:

$$M_r = \sum_{k=1}^{\infty} m_k^r N_k \quad (4.7)$$

Recalling that soot particles are modeled as spheres, the diffusivity coefficient D_k is written as:

$$D_k = D_0 m_k^{-\frac{2}{3}} \quad (4.8)$$

Accordingly, equation 4.6 can be expressed as:

$$\frac{\partial M_r}{\partial t} + \frac{\partial}{\partial x_i} (M_r U_i) = \frac{\partial}{\partial x_i} \left(D_0 \frac{\partial M_{r-\frac{2}{3}}}{\partial x_i} \right) - \frac{\partial}{\partial x_i} (M_r U_{T,i}) + \dot{M}_r \quad (4.9)$$

This is the conservative form of the soot moment transport equation. The soot source term is provided by the soot kinetic model *Frenklach* (2002), differing from this approach only by the use of non-reduced fractional moments. These moments require interpolation between whole-order moments; this is described in the section

on numerical challenges. Appendix B includes the formulation for the nondimensionalization of the soot moment transport equations, as well as the code for the Stineman interpolation method.

The chemistry utilized by the code for the soot simulations is a reduced mechanism (Directed Relation Graph (DRG), *Lu and Law (2005)*). The mechanism is based on a full chemical mechanism (*Appel et al. (2000)*) used to study soot formation in C_2 hydrocarbons. The DRG mechanism, performed by Lu and Luo (unpublished), is validated against a battery of tests to preserve the phenomenological consistency of the flame behavior. It was necessary to include a thorough validation of pyrene concentration since the soot model utilizes pyrene as the inception species for soot nucleation (*Appel et al. (2000)*).

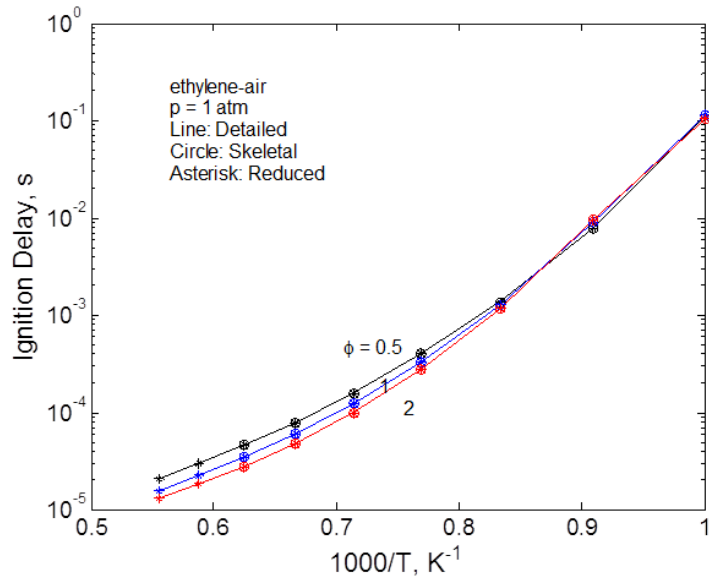


Figure 4.1: Ignition delay time as a function of initial mixture temperature for validation of skeletal (68 species) and reduced (62 species) chemical mechanism.

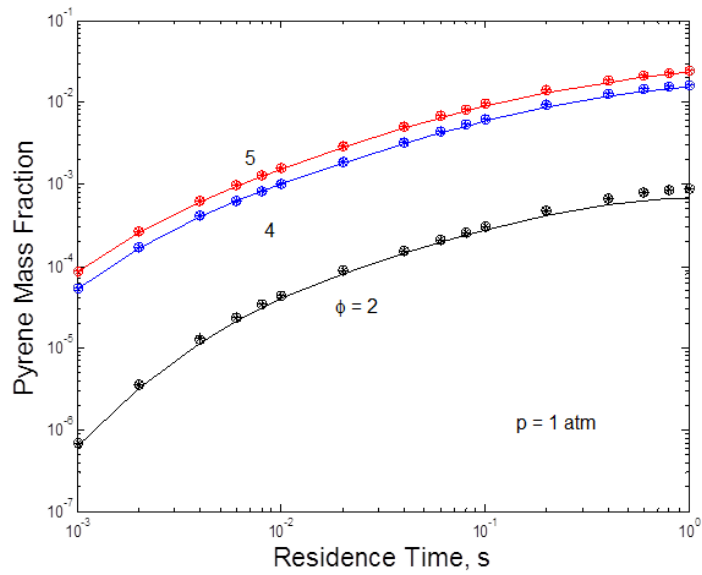


Figure 4.2: Pyrene mass fraction versus function of residence time

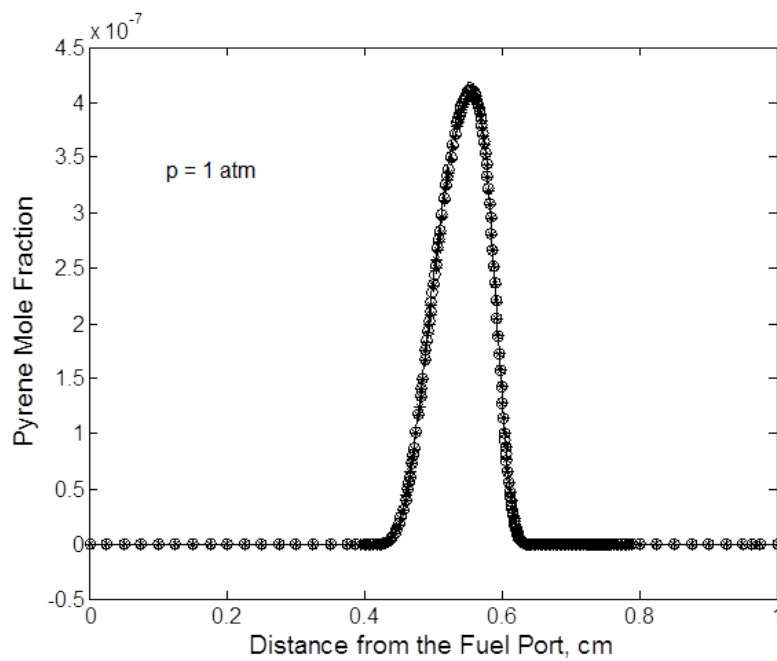


Figure 4.3: Diffusion flame profile of pyrene (A4) concentration.

4.3 Numerical challenges to high-fidelity soot modeling

4.3.1 Comparison of MOMIC studies

The implementation of MOMIC provides key advantages in soot modeling primarily because it can be utilized in a variety of combustion configurations and provides a more physically realistic level of soot formation and transport characteristics. This advances numerical simulation of soot towards better prediction of soot quantity. In the context of DNS we must approach the implementation and validation of MOMIC systematically to address stability and accuracy conditions.

The advantages that DNS offers in the context of CFD is the ability to accurately describe all the relevant scales of the flow, as well as reaction scales in combustion. Thus, DNS is fundamentally equipped to describe soot dynamics, which occur at molecular scales when considering nucleation, oxidation and surface growth and at centimeter to meter scales when considering transport. Therefore, in an effort to advance the numerical simulation of soot towards high-fidelity DNS, the following is a description of the state of the art regarding simulation methods which, when compared with the strong numerical fidelity demands of DNS, provides key insights into issues that must be addressed.

1. Numerical algorithms for flow solvers.

Frenklach (2002) provides the detailed description of the MOMIC implementation. It is mentioned that the MOMIC approach was validated in laminar premixed flames, laminar diffusion flames, plug-flow and perfectly stirred reactors. It is important to note that these cases were all steady laminar flames, and the numerical order of the simulations are assumed to be low order, high dissipation code from the CHEMKIN Suite.

In the context of high-fidelity numerical simulations, it is noted that the DNS code in this study is a high spatial order (8th) and high temporal Runge-Kutta (4th) code that is capable of preserving high gradients and is numerically low dissipation. As a consequence, the appearance of numerical noise at the low range of the moment signal is not smoothed. It is perfectly reasonable to assume that the higher dissipation of the flow solvers in previous studies did not address this issue because the noise was damped by the numerical scheme. We provide a solution to this source of instability that maintains fidelity to the physics of the problem.

2. Oxidation reaction

Interest in heterogenous combustion to study novel engine designs requires study of different mixing regimes. In an effort towards understanding the effects of transport, species and soot formation, our study proposes the use of ethylene air diffusion flames. In the implementation of this method in combustion, *Frenklach (2002)* notes that MOMIC fails to capture the oxidation dynamics of soot. This deficiency is treated with an appropriate approximation, and it raises an important issue that must be addressed in future studies.

The following subsection provides a description of the metric for statistical plausibility of the PSDF. The final sections provide results on one-dimensional transport and reactions tests with appropriate numerical algorithms to ameliorate the presence of instabilities.

4.3.2 Realizability

Given a set of moments describing a PSDF, the realizability provides assurance that the moments computed correspond to a plausible, positive semi-definite distribution function. The problem of realizability is important when considering the transport of particles such as soot.

While the code is able to transport the moments with high degree of spatial and

temporal accuracy, it is noted that this does not entirely guarantee that realizability is preserved (*Vikas et al.* (2011)). Realizability poses a stronger constraint on the time step than the Courant-Friedrichs-Lewy (CFL) condition. Accordingly, the time step must be reduced below values suggested by the CourantFriedrichsLewy (CFL) condition written into the code.

The approach requires that a given set of moments \mathbf{M}^6 and a weighted function $\mathcal{M}^{(6)}$, one can construct a general set of polynomials $\mathcal{P}^{(6)}(m)$:

$$\mathcal{P}^{(6)}(m) = \alpha^T \mathcal{M}^{(6)} \quad (4.10)$$

If \mathcal{P} is a distribution function, it is required that the values of \mathcal{P} be positive. Furthermore, it is required fro realizability that:

$$\langle \|\mathcal{P}^{(6)}(m)\|^2 P \rangle \geq 0 \quad (4.11)$$

$$\alpha^T \langle \mathcal{M}^{(6)} [\mathcal{M}^{(6)}]^T P \rangle \alpha \geq 0 \quad (4.12)$$

The matrix $\mathbf{H} = \langle \mathcal{M}^{(6)} [\mathcal{M}^{(6)}]^T P \rangle$ is a Hankel matrix, defined in its elements as:

$$\mathbf{H}_{i,j} = M_{i+j-2} \quad (4.13)$$

$$\mathbf{H} = \begin{pmatrix} M_0 & M_1 & M_2 & M_3 & M_4 & M_5 \\ M_1 & M_2 & M_3 & M_4 & M_5 & M_6 \\ M_2 & M_3 & M_4 & M_5 & M_6 & M_7 \\ M_3 & M_4 & M_5 & M_6 & M_7 & M_8 \\ M_4 & M_5 & M_6 & M_7 & M_8 & M_9 \\ M_5 & M_6 & M_7 & M_8 & M_9 & M_{10} \end{pmatrix}$$

Therefore, in order to prove the realizability of a 6th order moment (which is employed in the transport of soot), it is necessary to have knowledge of the 6th-10th order moment. Since higher moments are not computed explicitly by the current formulation, it is not possible to verify the realizability of all of the 6th-order moments. Nonetheless, the highest even valued moment that we do have knowledge of is moment 4, which allows for the determination of realizability up to $\mathbf{M}^{(3)}$. The Hankel matrix associated with $\mathbf{M}^{(3)}$ is:

$$\mathbf{H} = \begin{pmatrix} M_0 & M_1 & M_2 \\ M_1 & M_2 & M_3 \\ M_2 & M_3 & M_4 \end{pmatrix} \quad (4.14)$$

According to the Sylvester's criterion, $\mathbf{H}^{(3)}$ is positive definite if and only if all the following matrices have a positive determinant:

- the upper left 1x1 corner of $\mathbf{H}^{(3)}$
- the upper left 2-by-2 corner of $\mathbf{H}^{(3)}$
- $\mathbf{H}^{(3)}$ itself

Therefore, the moments for the matrix $\mathbf{H}^{(3)}$ produce through Sylvester's criterion the following conditions:

- $M_0 \geq 1$
- $\frac{M_0 M_2}{M_1^2} \geq 1$
- $M_2 \frac{M_0 M_4 + 2 M_3 M_1 - M_2^2}{M_0 M_3^2 + M_1^2 M_4} \geq 1$

In order to provide consistent data on the evolution of soot moments, the realizability condition must be satisfied to ensure a high degree of confidence that the moments represent a plausible particle size distribution function. While simulations on soot moments have demonstrated the capabilities of DNS in generating data sets on soot transport, the validity of the data as it pertains to realizability of the soot moments is not addressed. This study will seek to utilize the realizability as an

important metric to determine the accuracy of the soot PSDF.

4.3.3 Results

In order to evaluate the solution stability of the method in the context of DNS, a numerical simulation with transport only was run as a test case. The initial configuration consists of an atmospheric pressure, quiescent air at 500 K with an initial soot profile of $M_0 = (32 + 2^{i+1})e^{-x^4}$ and all subsequent moments as $M_{i+1} = (32 + 2^{i+1})M_i$, where i is the moment order and x is the spatial location. The pre-exponential factor was selected in order for initial conditions of the soot moments to conform to the realizability conditions described in the previous section.

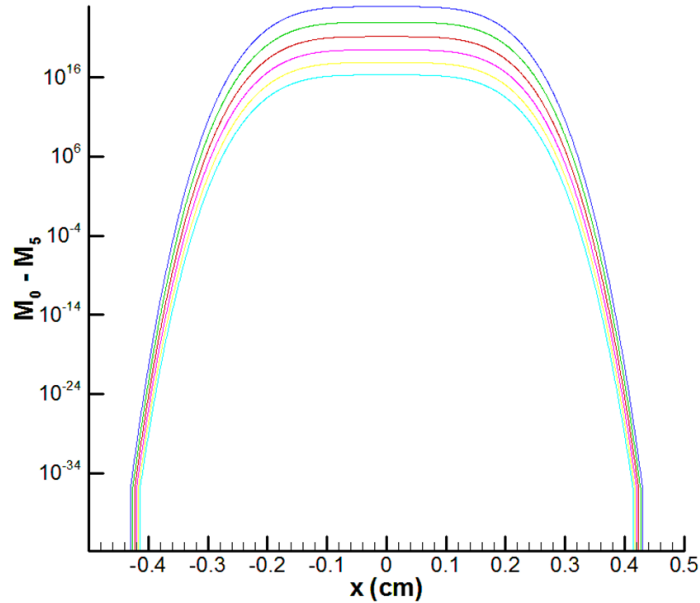


Figure 4.4: Initial conditions for the transport test cases. The moments are plotted in log scale.

The first implementation of the MOMIC approach resulted in the discovery of high frequency noise that begins to encroach into the higher values of soot moment. Soon after $t = 0.25ms$, the simulation crashes.

To resolve this issue, a high-pass filter that would be active at low concentration of

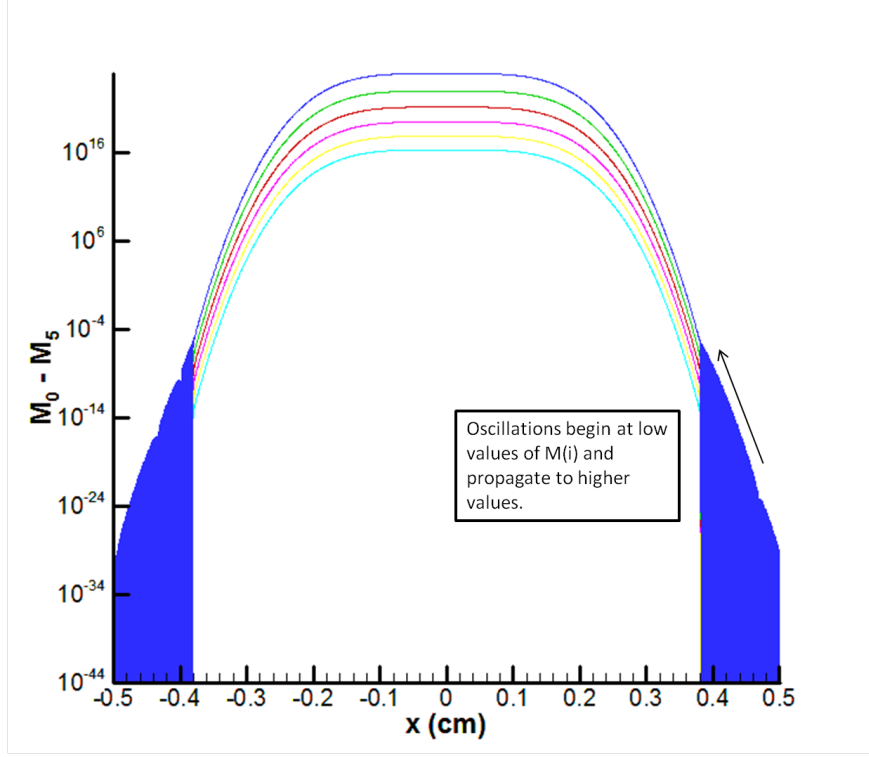


Figure 4.5: One-dimensional evolution of soot profile, with fractional moment diffusion in a quiescent field of pure air, $T=500$ K, $P=1$ atm. Moment profiles in log plot at $t=0.25$ ms

moment values was implemented. This effectively increases the numerical diffusivity of the moments only at such low values that the realizable solution remains unaffected. The function utilized to dissipate this value is derived from the following assumption:

- The magnitude of mass diffusion is treated as equal to momentum diffusion, $Sc_{soot} = \nu/D_{soot} = 1.0$
- All the moments values at low concentrations are treated as equi-diffusive (no additional weights are applied to different moment equations)
- The weighing function applied is dependent only on the value of M_0 , which represents the number density of the soot particles

The weighing function used to apply the artificial diffusivity on the soot moments is:

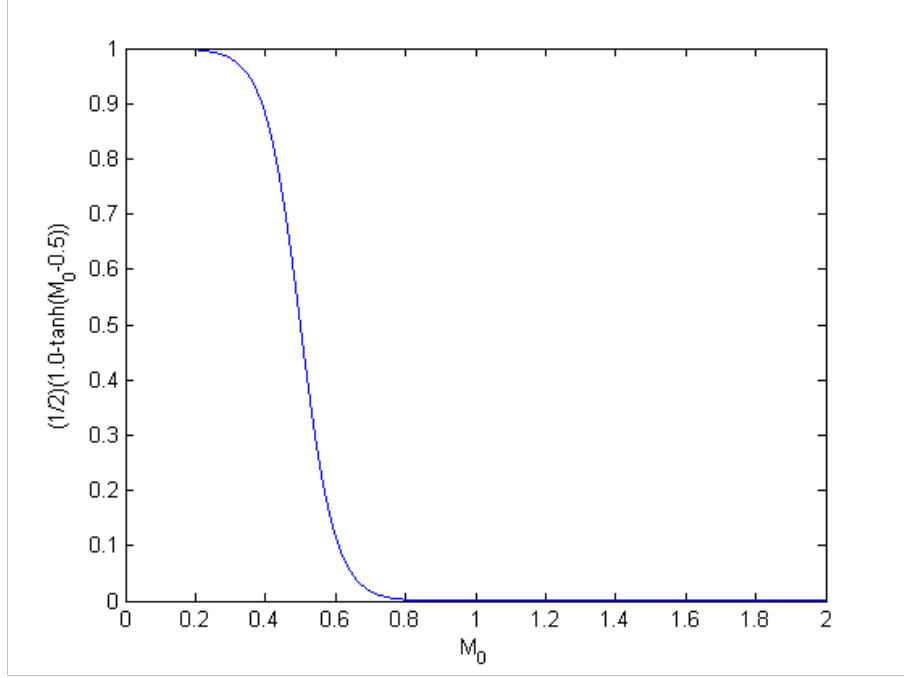


Figure 4.6: Weighing function for the artificial diffusion filter.

$$W(M_0) = \frac{1}{2}(1.0 - \tanh(M_0 - 0.5)) \quad (4.15)$$

The diffusion flux that is added to the transport equations of the soot moments is expressed as:

$$J_{i,soot,Sc} = W(M_0)D_{soot}\nabla M_i = \frac{1}{2}(1.0 - \tanh(M_0 - 0.5))\frac{\nu}{Sc_{soot}}\nabla M_i \quad (4.16)$$

The corresponding modified conservative form of the soot moment transport equation becomes:

$$\frac{\partial M_r}{\partial t} + \frac{\partial}{\partial x_i}(M_r U_i) = \frac{\partial}{\partial x_i} \left(D_0 \frac{\partial M_{r-\frac{2}{3}}}{\partial x_i} \right) + \frac{\partial}{\partial x_i} \left(W(M_0) D_{soot} \frac{\partial M_r}{\partial x_i} \right) - \frac{\partial}{\partial x_i} (M_r U_{T,i}) + \dot{M}_r \quad (4.17)$$

Note that there are three contributions to diffusion in the transport equations:

- Diffusion based on fractional moments: $\frac{\partial}{\partial x_i} \left(D_0 \frac{\partial M_{r-\frac{2}{3}}}{\partial x_i} \right)$
- Thermophoretic diffusion: $-\frac{\partial}{\partial x_i} (M_r U_{T,i})$
- M_0 -weighted artificial diffusion: $\frac{\partial}{\partial x_i} \left(W(M_0) D_{soot} \frac{\partial}{\partial x_i} M_r \right)$

4.3.4 One-dimensional inert, non-reactive, transport test

The application of this diffusive filter allows the solution to smooth out the high-frequency oscillations, as can be observed in 4.7 and 4.9. Nonetheless, figures 4.8 and 4.10 show that while the oscillations are damped out over the span of the simulation time, the challenge of maintaining the realizability remains elusive.

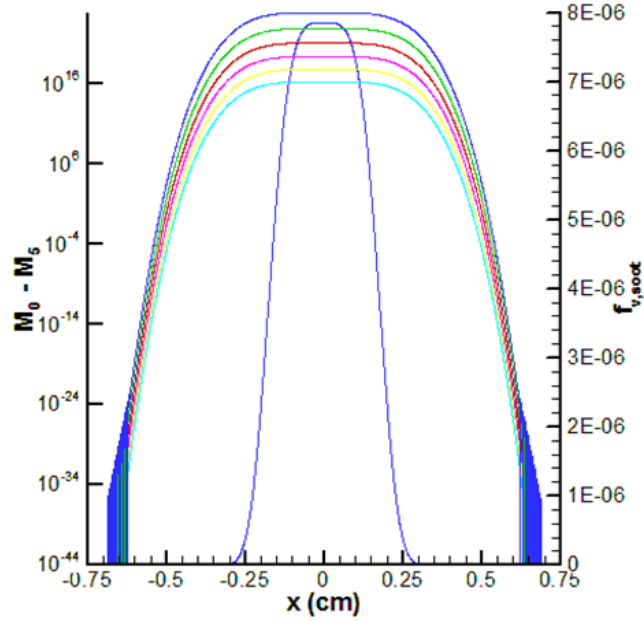


Figure 4.7: Case NV-DS, $t=0.255\text{ms}$

4.3.5 One-dimensional fuel-core, diffusion-flame

In the reacting case, however, we are encouraged by two factors that help to mitigate the problem of realizability in soot moment distributions. First, the initial conditions are derived from an OPPDIF (*Lutz et al. (1996)*) converged solution that

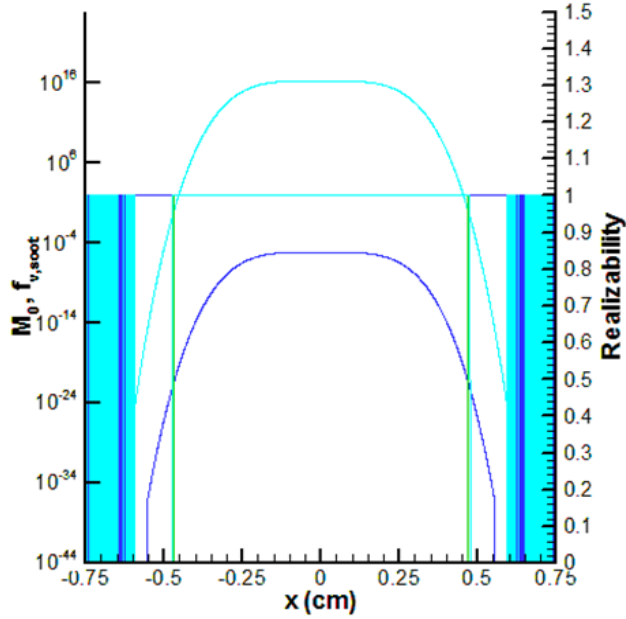


Figure 4.8: Case NV-DS, realizability, $t=0.255\text{ms}$

is determined by the physics, thereby is consistently realizable. Second, the initial case for a flame simulation includes minimum values above a threshold that prevents the appearance of these oscillations, since the signal itself is higher than the value of the numerical noise.

The one-dimensional flame configuration used in this study is derived in the following way:

- A one-dimensional diffusion flame is used to obtain a diffusion flamelet.
- A mixture fraction profile is defined as the independent variable. All species, the temperature and the soot moments are mapped onto the prescribed mixture fraction profile.
- A prescribed value of the gas velocity profile is applied.

Table 4.1 provides additional parameters for the initial condition profile.

The figures 4.12 - 4.14 show the evolution of the soot. The domain shown is only half of the domain, simulation is symmetric about $x = 0\text{cm}$. The soot moments are

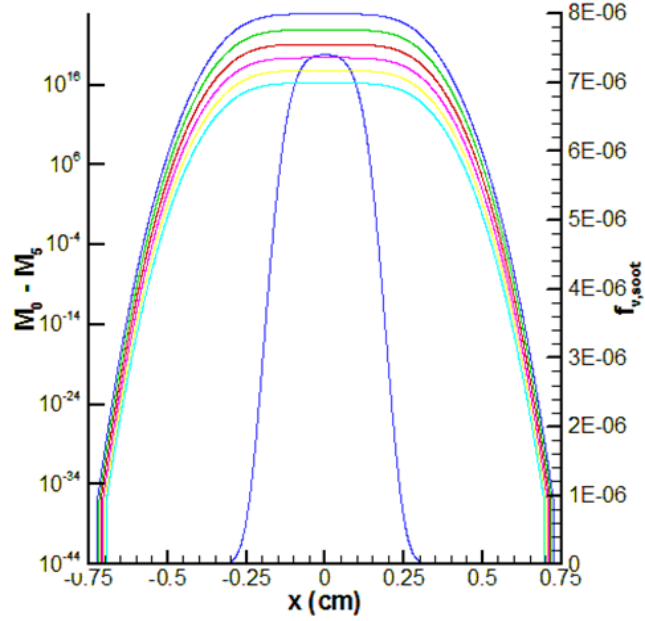


Figure 4.9: Case NV-FS zoomed, $t=1.725\text{ms}$

Scalar dissipation rate	χ_{st}	$7s^{-1}$
Domain length	L_x	2.4 cm
time step	Δt	1.0e-9

Table 4.1: Cases for soot transport evaluation stability and realizability

shown in log plot. The profile of average diameter of the soot population at every point is shown in linear plot. Note that after time 0.25 ms, the moment values of M_1 drops below M_0 . Unstable oscillation begin to form near the end of the simulation and the instability cause the code to fail. This can be explained by understanding the current physical limitations of the soot module that is utilized.

The dynamics of the inception, nucleation, surface growth and oxidation, are coupled back to the gas phase in a manner that conserves the mass. However, as the mass of the particles are reduced, there exist no mechanism that destroys the actual particle once it has reached the mass of the original particle. The reaction of pyrene, shown here:

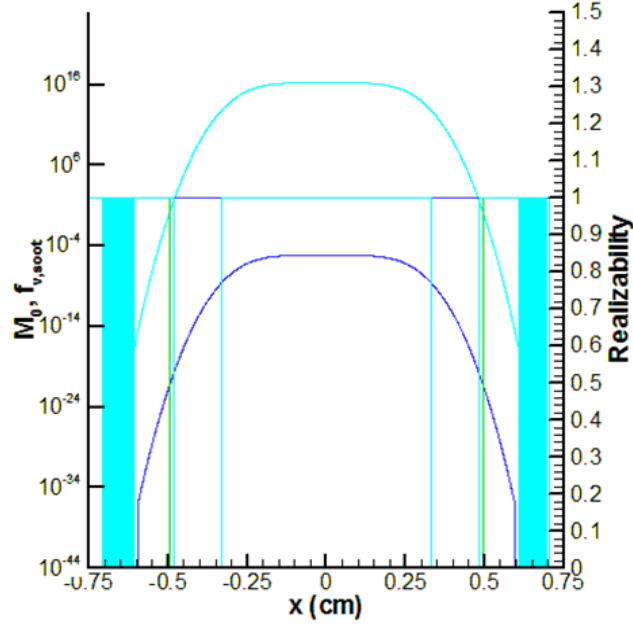


Figure 4.10: Case NV-DS zoomed, $t=1.725\text{ms}$



is the mechanism for the formation of the soot particle. The soot particles that are modeled by the moments continue to grow via the Hydrogen Abstraction Carbon Addition (HACA) mechanism. When oxidation becomes the dominate reaction term, the mass of carbon that is captured in the soot particles is returned to the gas phase, reducing the mass of the soot population described by the moments. M_1 , begins to approach the value of M_0 . Since a single soot particle that is created contains 32 carbon atoms, the reduction of a larger soot particle to a smaller one via oxidation would ultimately produce a particle that is reduced to the same size as the inception particle. This threshold is reached with the ratio of $M_1/M_0 = 32$. In order to maintain stability, we proposed that oxidation reaction be deactivated once the ratio of M_1/M_0 reaches a value of 32. Figures 4.15 - 4.17 show the temporal evolution of the one-dimensional fuel-core diffusion flame. With the oxidation shut-off condition,

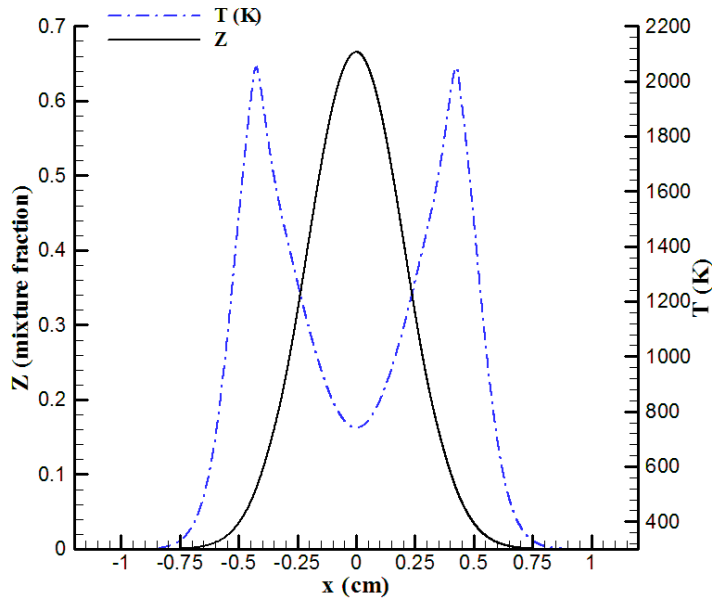


Figure 4.11: Plot of mixture fraction Z and temperature across space, initial conditions

the code stabilizes allows for the stable evolution of the diffusion flame, noting that this instability appears at negligible soot volume fraction values.

4.4 Concluding remarks

High-fidelity simulations were conducted to provide a framework for the accurate and stable modeling of soot using high-order method of moments. A DRG chemical mechanism that accurately captures the presence of pyrene (A4) is developed and incorporated into the code, and is considered an improvement in the ability to more accurately capture soot quantity. A systematic approach to resolve key issues regarding the appearance of high wavenumber oscillations was employed. A description of the method of moments is provided, and a moment transport model is incorporated into the S3D solver. The stability and accuracy issues encountered in evolution of the soot moments was investigated by individually introducing transport terms and numerical treatments to mitigate the oscillations. As a validation step, a

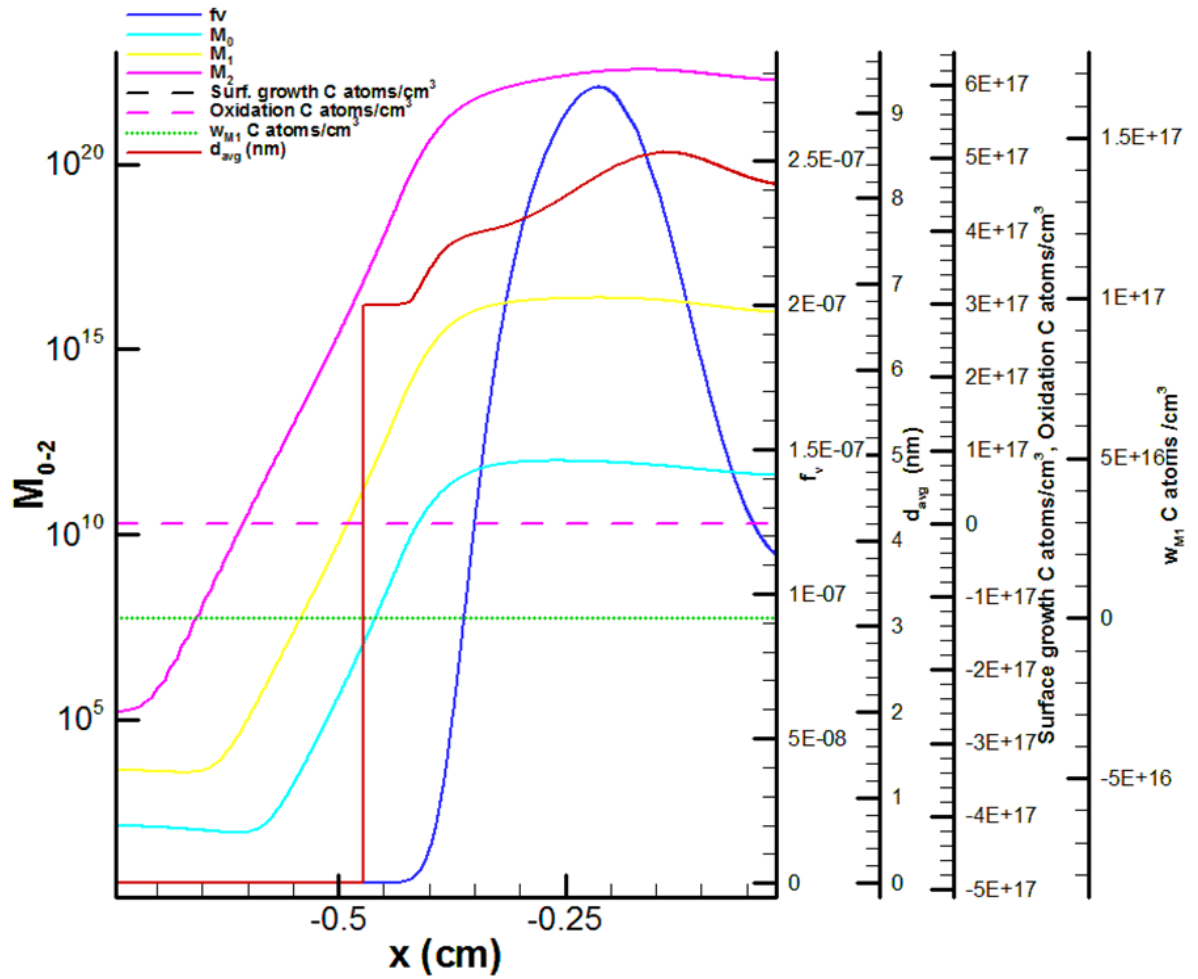


Figure 4.12: Plot of mixture fraction Z , soot volume fraction f_v , average diameter of soot particles d_{avg} , and soot reaction terms, $t=0.0$ ms

one-dimensional diffusion flame simulation was employed to validate the numerical treatments and assumptions.

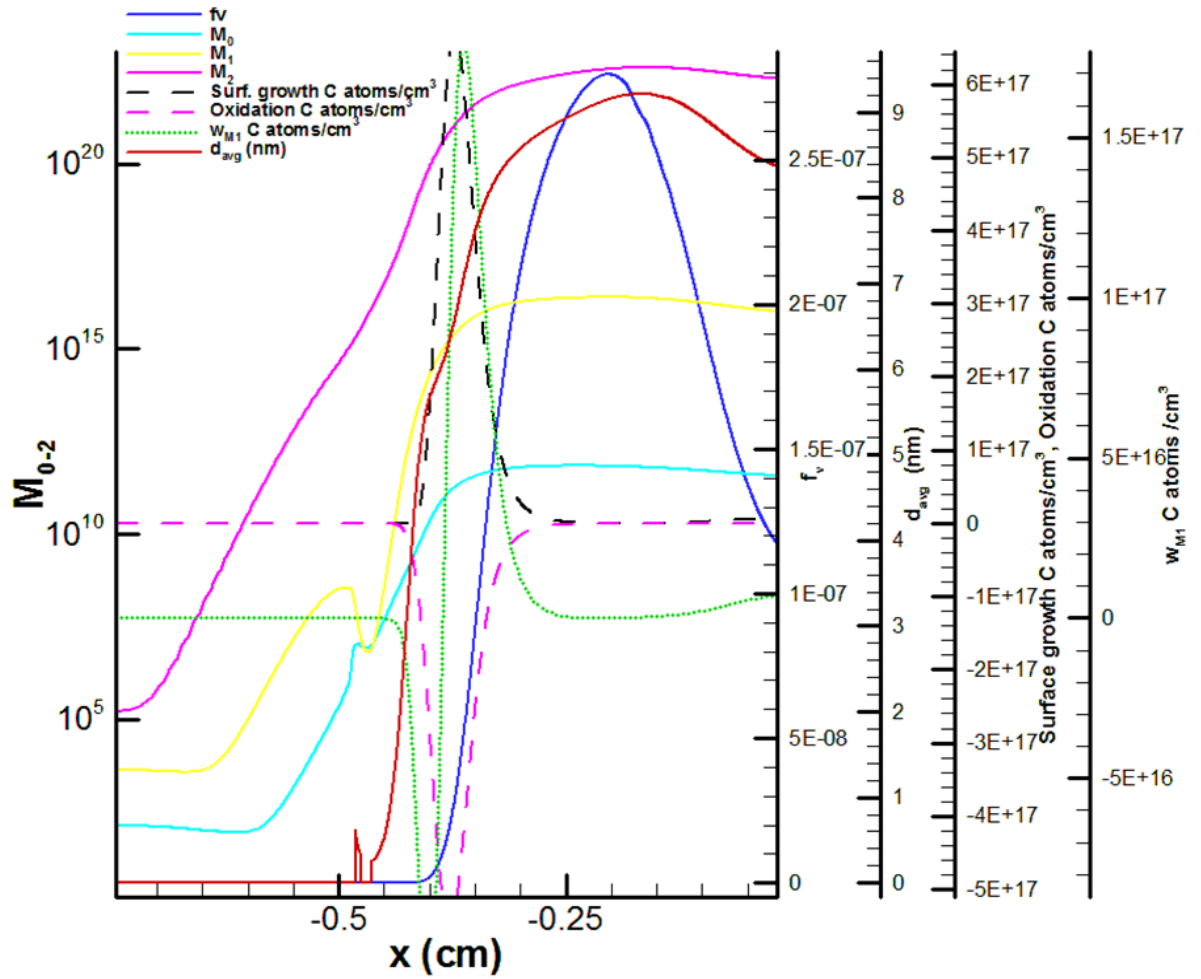


Figure 4.13: Plot of mixture fraction Z , soot volume fraction f_v , average diameter of soot particles d_{avg} , and soot reaction terms, $t=0.25$ ms

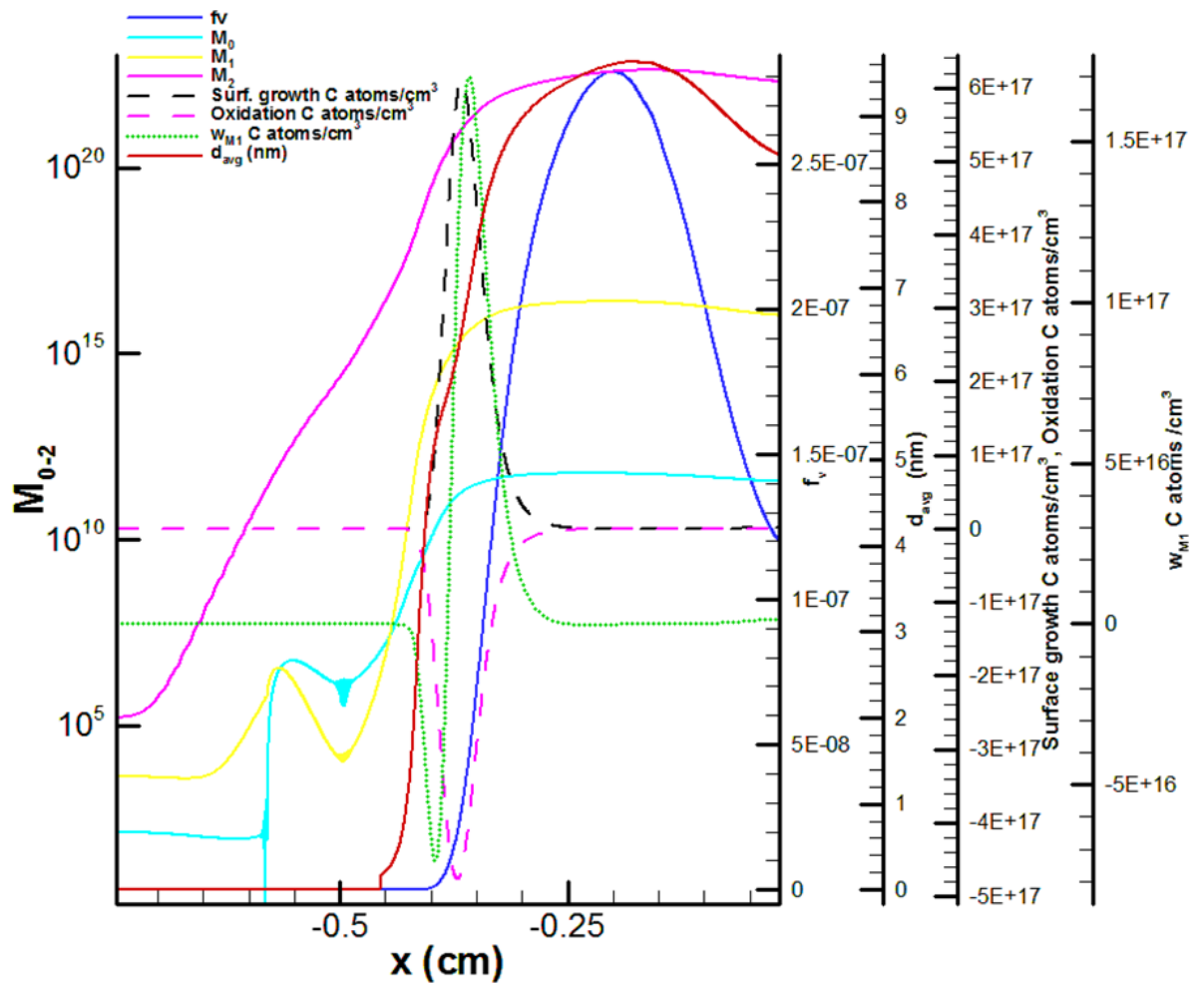


Figure 4.14: Plot of mixture fraction Z , soot volume fraction f_v , average diameter of soot particles d_{avg} , and soot reaction terms, $t=0.37$ ms

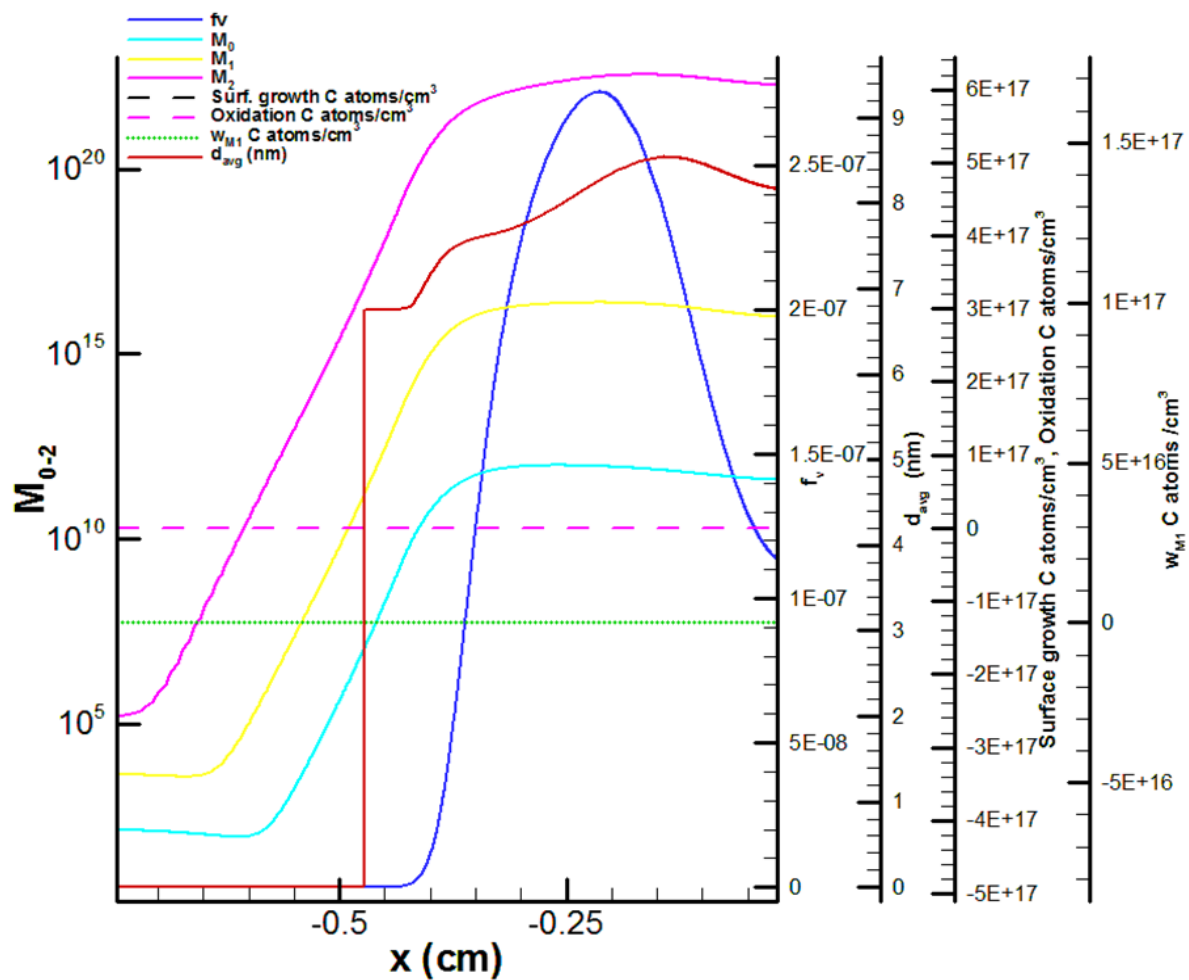


Figure 4.15: Plot of mixture fraction Z , soot volume fraction f_v , average diameter of soot particles d_{avg} , and soot reaction terms, $t=0.0$ ms

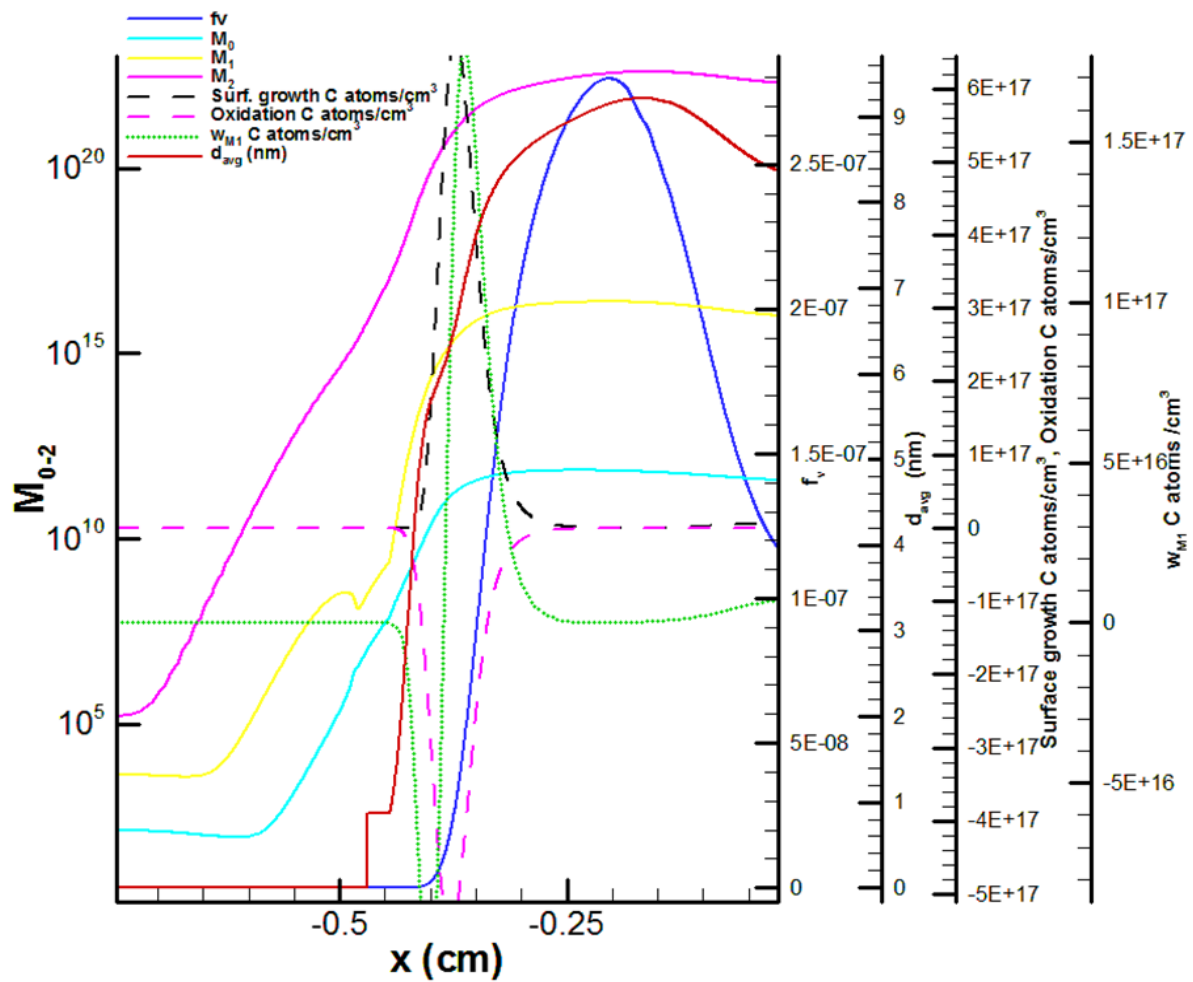


Figure 4.16: Plot of mixture fraction Z , soot volume fraction f_v , average diameter of soot particles d_{avg} , and soot reaction terms, $t=0.25$ ms

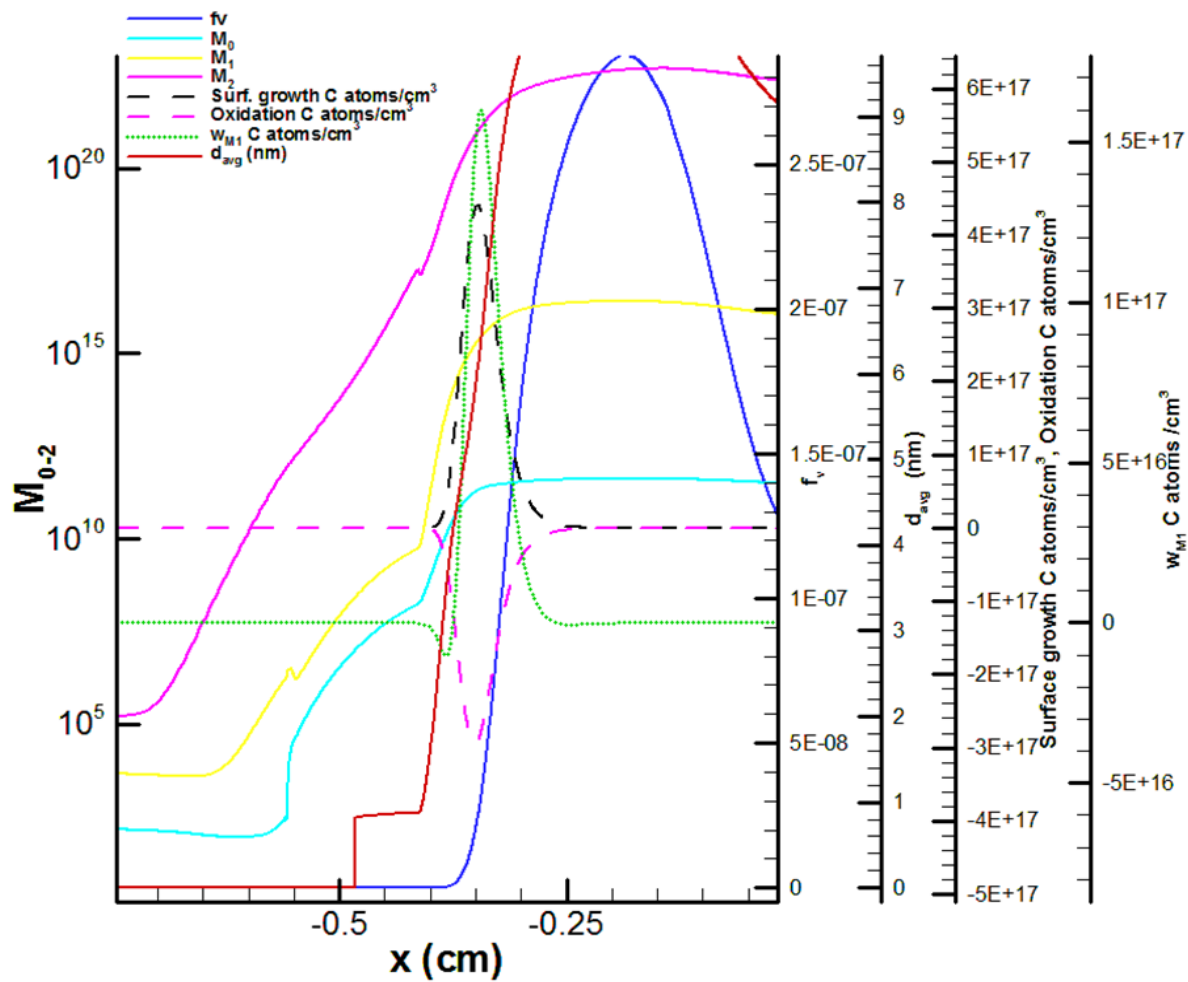


Figure 4.17: Plot of mixture fraction Z , soot volume fraction f_v , average diameter of soot particles d_{avg} , and soot reaction terms, $t=0.75$ ms

CHAPTER V

Conclusions

5.1 Conclusion

The dissertation presented some technical contributions in direct numerical simulations of turbulent flames with capabilities in describing liquid water spray and soot formation. Key contributions in computational model development and scientific investigation are summarized as follows:

1. Characteristic Boundary Conditions for Mass Additive Systems (Chapter 2)

A generalized formulation for the Navier-Stokes Characteristic Boundary Conditions (NSCBC) for compressible reacting flows was developed in order to account for the additional source terms associated with liquid spray droplets. The method allows full coupling of the Eulerian gas phase flow and the Lagrangian liquid droplet transport equations. The new formulation provides consistent and robust boundary condition treatment in the presence of liquid-gas interaction near the inflow and outflow boundaries, thereby allowing efficient and accurate simulations with finite domain sizes. A new finding in the generalized NSCBC for mass-additive systems was that all source terms appearing in the transport equations due to the liquid evaporation must be consistently incorporated in the characteristic boundary equations as well as in the local one-dimensional inviscid expressions. The method was validated by a series of test simulations including single droplets and a large number of droplets

crossing the domain boundaries.

2. Modified Mixture Fraction Formulation for Spray-Laden Flows (Chapter 2)

As an extension to the conventional theoretical approach to describe the reacting scalars in terms of conserved scalar variables, a three-stream mixture fraction formulation was developed in order to account for the additional species sources arising from liquid evaporation. The formulation allows an accurate and unambiguous identification of the flame location and maximum temperature in the presence of additional species generation within the flame due to fuel or water evaporation. The modified mixture fraction formulation proposed in this study provided a convenient and rational means to analyze various flame quantities accurately.

3. Extinction of Turbulent Nonpremixed Flames by Fine Water Spray Evaporation (Chapter 3)

The new computational developments for spray-laden combustion simulations have been utilized in the study of flame extinction due to fine water spray. The subject is relevant to modern fire suppression technology to better understand flame cooling effects by spray evaporation. In the investigation of reference laminar flame simulations, it was found that the modified mixture fraction formulation serves as an accurate diagnostic tool to map out correct flame responses. A unified flame extinction criterion was also proposed to incorporate the combined effects of flame weakening due to hydrodynamic strain and heat losses associated with radiation and water evaporation. Simulations of nonpremixed flames subjected to random flow fluctuations revealed formation of edge flames that can serve as a mechanism for re-ignition. The validity of the unified extinction criterion was demonstrated as a robust identification metric for flame extinction due to various quenching mechanisms.

4. Advanced Soot Models for DNS with Detailed Chemistry (Chapter 4)

Toward predictive simulations of combustion-generated particulate formation, DNS with realistic hydrocarbon fuels was extended to describe complex soot formation

processes by using a higher order method of moments soot model. The choice of the method was based on the consideration of the level of fidelity and computational efficiency. While the method of moments has been used at various levels of complexities in homogeneous systems and engineering simulations, its application in high resolution simulations has been rare. For optimal results, the present study adopted the method of moments with interpolative closure (MOMIC) approach with a total of six moment variables. Detailed development and implementation efforts into multi-dimensional DNS code have revealed a large number of subtle computational issues that have not been found in previous studies. Remedies and improvements for the observed computational difficulties were proposed and validated in various test simulations. The comprehensive model development approach has led to a robust and accurate prediction of soot formation for laminar ethylene-air nonpremixed flames with improved accuracy in the prediction of the total soot production and size distribution characteristics, and points to additional physics that need to be addressed in the pursuit of high-fidelity DNS with soot modeling.

5.2 Future work

During the last decades, DNS has emerged as a valuable research tool in the investigation of fundamental behavior and characterization of combustion phenomena. In principle, an important advantage of DNS over the state-of-the-art experimental diagnostic tools is that it can provide spatially and temporally resolved information of all scalar variables considered, provided the underlying submodels are accurate. In reality, DNS of multi-dimensional turbulent combustion still compromises on accuracy in chemistry, since large amounts of species would increase the computational costs. Other factors that increase the computational costs include the dimensionality of the configuration (1,2 or 3 dimensional) and the range of physical parameters such as high Reynolds number flows, which place a greater demand on capturing ever finer scales

at high Re values. However, as peta-scale computing resources become increasingly available, DNS will be able to reproduce realistic laboratory-scale problems with the utmost accuracy.

It is anticipated that in the future, an extension of the counterflow flame configuration to 3-D will produce better insights of turbulence-chemistry interactions as well as the interaction of water spray. This will ultimately lead to a much greater understanding of these coupled interactions by allowing more accurate statistical analysis with more physically realistic turbulence. In particular, future work will lead to a better understanding of the minimum water loading characteristics for novel mist systems, thereby providing data that will lead to better designs that are effective at quenching fires while preventing extensive water damage to property.

The present study also demonstrated a use of advanced soot models in DNS based on higher order method of moments. In Chapter 4, the investigation was mainly focused on detailed model implementation and its overall effects in achieving accurate and stable solution behavior. An obvious immediate step is to demonstrate the new advanced soot models in 2D and 3D parametric simulations. Since the level of accuracy in predicting various soot quantities have been assessed in this study, the detailed multi-dimensional simulations will reveal quantitative effects of external parameters such as turbulence intensity, mean and variance in the strain rate fluctuation, and the radiative heat losses. The simulation database will be valuable resources to identify and assess different dominant chemical pathways in different regions within turbulent flames. This will lead to a better physical understanding of sooting processes, leading towards efficient and clean combustion of complex hydrocarbon fuels.

Advances in supercomputing resources have allowed DNS to maintain a leading role in the study of fundamental flame studies. Further advancements in both algorithms and computational platforms, will allow for more practical, laboratory scale simulations. The need to maintain the high fidelity nature of direct numerical simu-

lation demands rigorous theoretical study of algorithm stability and model accuracy, thereby ensuring that solutions to realistic combustion problems maintain the highest standards of quality.

APPENDICES

APPENDIX A

Practical details for Navier-Stokes Characteristic Boundary Conditions (NSCBC)

The development of NSCBC stems from work begun by *Thompson* (1987) on Euler equations, extended to Navier-Stokes by *Poinsot and Lele* (1992) and subsequently extended to reacting flows by *Sutherland and Kennedy* (2003) and *Yoo and Im* (2007b). The following is a description of the approach as well as the details of the derivation of the NSCBC for mass-additive systems.

We define the following expressions:

$$E_t = \frac{p}{\gamma - 1} + \frac{1}{2}\rho u_\alpha^2 = \rho h - p + \frac{1}{2}\rho u_\alpha^2 \quad (\text{A.1})$$

$$c = \sqrt{\frac{\gamma p}{\rho}} \quad (\text{A.2})$$

$$h = \sum_{i=1}^N h_i Y_i \quad (\text{A.3})$$

where E_t is the total energy, c is the acoustic speed, and h is the total enthalpy of the mixture.

The strategy for obtaining the characteristic equations requires a transformation from conservative to primitive to characteristic variable space as shown in Chapter 2:

$$\frac{\partial \mathbf{U}_\alpha}{\partial t} + \nabla_{(n)} \cdot \mathbf{F}_a^{(n)} + \nabla_{(t)} \cdot \mathbf{F}_a^{(t)} = \mathbf{D}_a^{(n)} + \mathbf{D}_a^{(t)} + \mathbf{s}_a \quad (\text{A.4})$$

$$\begin{aligned} & \quad \quad \quad (\mathbf{P})_{ba}^{-1} \downarrow \quad \quad \uparrow \mathbf{P}_{ab} \\ \frac{\partial U_b}{\partial t} + A_{bd}^{(n)} \cdot (\nabla_{(n)} \cdot U_d) + A_{bd}^{(t)} \cdot (\nabla_{(t)} U_d) &= D_b^{(n)} + D_b^{(t)} + s_b \quad (\text{A.5}) \end{aligned}$$

$$\begin{aligned} & \quad \quad \quad (S^{(n)})_{cb}^{-1} \downarrow \quad \quad \uparrow S_{bc}^{(n)} \\ (S^{(n)})_{cb}^{-1} \frac{\partial U_b}{\partial t} + \mathcal{L}_c^{(n)} + \mathcal{A}_{cd}^{(t)} \cdot (\nabla_{(t)} U_d) &= \mathcal{D}_c^{(n)} + \mathcal{D}_c^{(t)} + \mathbf{s}_c \quad (\text{A.6}) \end{aligned}$$

In order to convert the Navier-Stokes equations from conservative variable space to primitive variables space, we need to compute the matrix $P = \frac{\partial \mathbf{U}}{\partial \mathbf{U}}$, where \mathbf{U} is the conservative variable and U represents the primitive variable. In 2-D, the conservative and primitive variable vectors are:

$$\mathbf{U} = \begin{pmatrix} \rho u \\ \rho v \\ \rho w \\ \rho \\ E_t \\ \rho Y_i \\ \vdots \\ \rho Y_N \end{pmatrix} \quad (\text{A.7})$$

$$U = \begin{pmatrix} u \\ v \\ w \\ \rho \\ p \\ Y_i \\ \vdots \\ Y_N \end{pmatrix} \quad (\text{A.8})$$

The matrix $P = \frac{\partial \mathbf{U}}{\partial U}$ is expressed as:

$$P = \begin{pmatrix} \rho & 0 & 0 & u & 0 & 0 & 0 & 0 \\ 0 & \rho & 0 & v & 0 & 0 & 0 & 0 \\ 0 & 0 & \rho & w & 0 & 0 & 0 & 0 \\ 0 & 0 & 0 & 1 & 0 & 0 & 0 & 0 \\ \rho u & \rho v & \rho w & e_t - c_v T & \frac{1}{\gamma-1} & \rho \left(h_i - \frac{c_p W T}{W_i} \right) & \dots & \rho \left(h_N - \frac{c_p W T}{W_N} \right) \\ 0 & 0 & 0 & Y_i & 0 & \rho & 0 & 0 \\ 0 & 0 & 0 & \vdots & 0 & 0 & \ddots & 0 \\ 0 & 0 & 0 & Y_N & 0 & 0 & 0 & \rho \end{pmatrix} \quad (\text{A.9})$$

with P^{-1} :

$$P^{-1} = \begin{pmatrix} \frac{1}{\rho} & 0 & 0 & -\frac{u}{\rho} & 0 & 0 & 0 & 0 \\ 0 & \frac{1}{\rho} & 0 & -\frac{v}{\rho} & 0 & 0 & 0 & 0 \\ 0 & 0 & \frac{1}{\rho} & -\frac{w}{\rho} & 0 & 0 & 0 & 0 \\ 0 & 0 & 0 & 1 & 0 & 0 & 0 & 0 \\ u(1-\gamma) & v(1-\gamma) & w(1-\gamma) & \frac{(u^2+v^2)(\gamma-1)}{2} & \gamma-1 & (\gamma-1)\left(\frac{c_p TW}{W_i} - h_i\right) & \cdots & (\gamma-1)\left(\frac{c_p TW}{W_N} - h_N\right) \\ 0 & 0 & -\frac{Y_i}{\rho} & 0 & 0 & \frac{1}{\rho} & 0 & 0 \\ 0 & 0 & \vdots & 0 & 0 & 0 & \ddots & 0 \\ 0 & 0 & -\frac{Y_N}{\rho} & 0 & 0 & 0 & 0 & \frac{1}{\rho} \end{pmatrix} \quad (\text{A.10})$$

Recall that the conservative equations are:

$$\frac{\partial}{\partial t} \begin{bmatrix} \rho \mathbf{u}_\alpha \\ \rho \\ \rho e_t \\ \rho Y_i \end{bmatrix} = \begin{bmatrix} -\nabla_\beta \cdot (\rho \mathbf{u}_\alpha \mathbf{u}_\beta + p \delta_{\alpha\beta}) + \nabla_\beta \cdot \tau_{\beta\alpha} + \rho \sum_{i=1}^N Y_i \mathbf{f}_{i\alpha} + \psi_{u_\alpha} \\ -\nabla_\beta \cdot (\rho \mathbf{u}_\beta) + \psi_\rho \\ -\nabla_\beta \cdot [(\rho e_t + p) \mathbf{u}_\beta] + \nabla_\beta \cdot (\tau_{\beta\alpha} \cdot \mathbf{u}_\alpha - \mathbf{q}_\beta) + \rho \sum_{i=1}^N Y_i \mathbf{f}_{i\beta} \cdot (\mathbf{u}_\beta + \mathbf{V}_{i\beta}) + \psi_e \\ -\nabla_\beta \cdot (\rho Y_i \mathbf{u}_\beta) - \nabla_\beta \cdot (\rho Y_i \mathbf{V}_{i\beta}) + W_i \dot{\omega}_i + \psi_{Y_i} \end{bmatrix} \quad (\text{A.11})$$

If we consider that x is the normal direction, then we can write the conservative equations in form of Eqn. A.4:

$$\begin{aligned}
\frac{\partial}{\partial t} \begin{bmatrix} \rho u \\ \rho v \\ \rho w \\ \rho \\ \rho e_t \\ \rho Y_i \end{bmatrix} + \begin{bmatrix} \frac{\partial}{\partial x}(\rho u u + p) \\ \frac{\partial}{\partial x}(\rho v u) \\ \frac{\partial}{\partial x}(\rho w u) \\ \frac{\partial}{\partial x}(\rho u) \\ \frac{\partial}{\partial x}(\rho e_t + p)u \\ \frac{\partial}{\partial x}(\rho Y_i u) \end{bmatrix} + \begin{bmatrix} \frac{\partial}{\partial y}(\rho u v) + \frac{\partial}{\partial z}(\rho u w) \\ \frac{\partial}{\partial y}(\rho v v + p) + \frac{\partial}{\partial z}(\rho v w) \\ \frac{\partial}{\partial y}(\rho w v) + \frac{\partial}{\partial z}(\rho w w + p) \\ \frac{\partial}{\partial y}(\rho v) + \frac{\partial}{\partial z}(\rho w) \\ \frac{\partial}{\partial y}(\rho e_t + p)v + \frac{\partial}{\partial z}(\rho e_t + p)w \\ \frac{\partial}{\partial y}(\rho Y_i v) + \frac{\partial}{\partial z}(\rho Y_i w) \end{bmatrix} = \\
\begin{bmatrix} \frac{\partial}{\partial x}(\tau_{xx}) \\ \frac{\partial}{\partial x}(\tau_{xy}) \\ \frac{\partial}{\partial x}(\tau_{xz}) \\ 0 \\ \frac{\partial}{\partial x}(\tau_{x\alpha} \cdot u_\alpha - q_x) \\ \frac{\partial}{\partial x}(\rho Y_i V_{i,x}) \end{bmatrix} + \begin{bmatrix} \frac{\partial}{\partial y}(\tau_{yx}) + \frac{\partial}{\partial z}(\tau_{zx}) \\ \frac{\partial}{\partial y}(\tau_{yy}) + \frac{\partial}{\partial z}(\tau_{zy}) \\ \frac{\partial}{\partial y}(\tau_{yz}) + \frac{\partial}{\partial z}(\tau_{zz}) \\ 0 \\ \frac{\partial}{\partial y}(\tau_{y\alpha} \cdot u_\alpha - q_y) + \frac{\partial}{\partial z}(\tau_{z\alpha} \cdot u_\alpha - q_z) \\ \frac{\partial}{\partial y}(\rho Y_i V_{i,y}) + \frac{\partial}{\partial z}(\rho Y_i V_{i,z}) \end{bmatrix} + \\
\begin{bmatrix} \rho \sum_{i=1}^N Y_i f_{i,x} + \psi_u \\ \rho \sum_{i=1}^N Y_i f_{i,y} + \psi_v \\ \rho \sum_{i=1}^N Y_i f_{i,z} + \psi_w \\ \psi_\rho \\ \rho \sum_{i=1}^N Y_i f_{i,\alpha} \cdot (u_\alpha + V_{i,\alpha}) + \psi_e \\ W_i \dot{\omega} + \psi_{Y_i} \end{bmatrix} \tag{A.12}
\end{aligned}$$

When we apply the matrix P^{-1} to Eqn. A.12, we obtain the primitive variable form of the Navier-Stokes equations with the mass additive terms:

$$\begin{aligned}
& \frac{\partial}{\partial t} \begin{bmatrix} u \\ v \\ w \\ \rho \\ p \\ Y_i \end{bmatrix} + \begin{bmatrix} u \frac{\partial u}{\partial x} + \frac{1}{\rho} \frac{\partial p}{\partial x} \\ u \frac{\partial v}{\partial x} \\ u \frac{\partial w}{\partial x} \\ \rho \frac{\partial u}{\partial x} + u \frac{\partial \rho}{\partial x} \\ u \frac{\partial p}{\partial x} + \gamma p \frac{\partial u}{\partial x} \\ u \frac{\partial Y_i}{\partial x} \end{bmatrix} + \begin{bmatrix} v \frac{\partial u}{\partial y} + w \frac{\partial u}{\partial z} \\ v \frac{\partial v}{\partial y} + \frac{1}{\rho} \frac{\partial p}{\partial y} + w \frac{\partial v}{\partial z} \\ v \frac{\partial w}{\partial y} + w \frac{\partial w}{\partial z} + \frac{1}{\rho} \frac{\partial p}{\partial z} \\ \rho \frac{\partial v}{\partial y} + v \frac{\partial \rho}{\partial y} + \rho \frac{\partial w}{\partial z} + w \frac{\partial \rho}{\partial z} \\ v \frac{\partial p}{\partial y} + w \frac{\partial p}{\partial z} + \gamma p \frac{\partial v}{\partial y} + \gamma p \frac{\partial w}{\partial z} \\ v \frac{\partial Y_i}{\partial y} \end{bmatrix} = \\
& \begin{bmatrix} \frac{1}{\rho} \frac{\partial}{\partial x} (\tau_{xx}) \\ \frac{1}{\rho} \frac{\partial}{\partial x} (\tau_{xy}) \\ \frac{1}{\rho} \frac{\partial}{\partial x} (\tau_{xz}) \\ 0 \\ d_p^{(n)} \\ \frac{1}{\rho} \frac{\partial}{\partial x} (\rho Y_i V_{i,x}) \end{bmatrix} + \begin{bmatrix} \frac{1}{\rho} \frac{\partial}{\partial y} (\tau_{yx}) + \frac{1}{\rho} \frac{\partial}{\partial z} (\tau_{zx}) \\ \frac{1}{\rho} \frac{\partial}{\partial y} (\tau_{yy}) + \frac{1}{\rho} \frac{\partial}{\partial z} (\tau_{zy}) \\ \frac{1}{\rho} \frac{\partial}{\partial y} (\tau_{yz}) + \frac{1}{\rho} \frac{\partial}{\partial z} (\tau_{zz}) \\ 0 \\ d_p^{(t)} \\ \frac{1}{\rho} \frac{\partial}{\partial y} (\rho Y_i V_{i,y}) + \frac{1}{\rho} \frac{\partial}{\partial z} (\rho Y_i V_{i,z}) \end{bmatrix} + \\
& \begin{bmatrix} \Sigma_{i=1}^N Y_i f_{i,x} + (\psi_u - u\psi_\rho)/\rho \\ \Sigma_{i=1}^N Y_i f_{i,y} + (\psi_v - v\psi_\rho)/\rho \\ \Sigma_{i=1}^N Y_i f_{i,z} + (\psi_w - w\psi_\rho)/\rho \\ \psi_\rho \\ s_p \\ (1/\rho)(W_i \dot{\omega}_i + (1 - Y_i)\psi_\rho \delta_{i,H_2O}) \end{bmatrix} \tag{A.13}
\end{aligned}$$

The general value of the matrix $A^{(n)} = P^{-1} \frac{\partial F}{\partial U}$, and can be expressed as:

$$A^{(n)} = \begin{bmatrix} u^{(n)} & 0 & 0 & 0 & \frac{\delta_{1n}}{\rho} & 0 \\ 0 & u^{(n)} & 0 & 0 & \frac{\delta_{2n}}{\rho} & 0 \\ 0 & 0 & u^{(n)} & 0 & \frac{\delta_{3n}}{\rho} & 0 \\ \rho\delta_{1n} & \rho\delta_{2n} & \rho\delta_{3n} & u^{(n)} & 0 & 0 \\ \gamma p\delta_{1n} & \gamma p\delta_{2n} & \gamma p\delta_{3n} & 0 & u^{(n)} & 0 \\ 0 & 0 & 0 & 0 & 0 & u^{(n)}\delta_{ij} \end{bmatrix} \quad (\text{A.14})$$

In the case of x direction:

$$A^{(x)} = \begin{bmatrix} u & 0 & 0 & 0 & \frac{1}{\rho} & 0 \\ 0 & u & 0 & 0 & 0 & 0 \\ 0 & 0 & u & 0 & 0 & 0 \\ \rho & 0 & 0 & u & 0 & 0 \\ \gamma p & 0 & 0 & 0 & u & 0 \\ 0 & 0 & 0 & 0 & 0 & u \end{bmatrix} \quad (\text{A.15})$$

By taking the eigenvalue decomposition of $A^{(x)}$, we can extract the $S^{(n)}$ matrix and its inverse as well as the eigenvalues:

$$S^{(x)} = \begin{bmatrix} -\frac{1}{\rho c} & 0 & 0 & 0 & \frac{1}{\rho c} & 0 \\ 0 & 1 & 0 & 0 & 0 & 0 \\ 0 & 0 & 1 & 0 & 0 & 0 \\ \frac{\rho}{\gamma p} & 0 & 0 & 1 & \frac{\rho}{\gamma p} & 0 \\ 1 & 0 & 0 & 0 & 1 & 0 \\ 0 & 0 & 0 & 0 & 0 & 1 \end{bmatrix} \quad (\text{A.16})$$

$$(S^{(x)})^{-1} = \begin{bmatrix} -\frac{\rho c}{2} & 0 & 0 & 0 & \frac{1}{2} & 0 \\ 0 & 1 & 0 & 0 & 0 & 0 \\ 0 & 0 & 1 & 0 & 0 & 0 \\ 0 & 0 & 0 & 1 & -\frac{1}{c^2} & 0 \\ \frac{\rho c}{2} & 0 & 0 & 0 & \frac{1}{2} & 0 \\ 0 & 0 & 0 & 0 & 0 & 1 \end{bmatrix} \quad (\text{A.17})$$

Applying $(S^{(x)})^{-1}$ to the Eqn. A.13, we arrive at the characteristic form of the Navier-Stokes equations:

$$\begin{bmatrix} \frac{1}{2}(\frac{\partial p}{\partial t} - \rho c \frac{\partial u}{\partial x}) \\ \frac{\partial v}{\partial t} \\ \frac{\partial w}{\partial t} \\ \frac{\partial \rho}{\partial t} - \frac{1}{c^2} \frac{\partial u}{\partial x} \\ \frac{1}{2}(\frac{\partial p}{\partial t} + \rho c \frac{\partial u}{\partial x}) \\ \frac{\partial Y_i}{\partial t} \end{bmatrix} + \begin{bmatrix} \frac{u-c}{2}(\frac{\partial p}{\partial x} - \rho c \frac{\partial u}{\partial x}) \\ u \frac{\partial v}{\partial x} \\ u \frac{\partial w}{\partial x} \\ u(\frac{\partial \rho}{\partial x} - \frac{1}{c^2} \frac{\partial p}{\partial x}) \\ \frac{u+c}{2}(\frac{\partial p}{\partial x} + \rho c \frac{\partial u}{\partial x}) \\ u \frac{\partial Y_i}{\partial x} \end{bmatrix} + \begin{bmatrix} (\mathbf{v}_t \cdot \nabla_t p + \gamma p \nabla \cdot \mathbf{v}_t - \rho c \mathbf{v}_t \nabla_t u)/2 \\ (\mathbf{v}_t \cdot \nabla_t v + (1/\rho) \partial p / \partial y) \\ (\mathbf{v}_t \cdot \nabla_t w + (1/\rho) \partial p / \partial w) \\ \nabla_t \cdot (\rho \mathbf{v}_t) - (\mathbf{v}_t \cdot \nabla_t p + \gamma p \nabla_t \cdot \mathbf{v}_t)/c^2 \\ (\mathbf{v}_t \cdot \nabla_t p + \gamma p \nabla \cdot \mathbf{v}_t + \rho c \mathbf{v}_t \nabla_t u)/2 \\ \mathbf{v}_t \cdot \nabla_t Y_i \end{bmatrix} = \begin{bmatrix} (d_p - \rho c d_u)/2 \\ d_v \\ d_w \\ d_\rho - d_p/c^2 \\ (d_p + \rho c d_u)/2 \\ d_{Y_i} \end{bmatrix} + \begin{bmatrix} (s_p - \rho c s_u)/2 \\ s_v \\ s_w \\ s_\rho - s_p/c^2 \\ (s_p + \rho c s_u)/2 \\ s_{Y_i} \end{bmatrix} \quad (\text{A.18})$$

The first group on the right hand side corresponds to $\mathcal{D}_c^{(n)} + \mathcal{D}_c^{(t)}$ and the second group corresponds to \mathfrak{s}_c from equation A.6, with the following d and s vectors:

$$\begin{bmatrix} d_u \\ d_v \\ d_w \\ d_\rho \\ d_p \\ d_{Y_i} \end{bmatrix} = \begin{bmatrix} (1/\rho)\nabla_\alpha \cdot \tau_{\alpha x} \\ (1/\rho)\nabla_\alpha \cdot \tau_{\alpha y} \\ (1/\rho)\nabla_\alpha \cdot \tau_{\alpha z} \\ 0 \\ (\gamma - 1) [\tau_{\beta\alpha} : \nabla_\beta \mathbf{u}_\alpha - \nabla_\alpha \cdot \mathbf{q}_\alpha + \sum_{i=1}^N (h_i - c_p TW/W_i) \nabla_\alpha \cdot (\rho Y_i V_{i,\alpha})] \\ (1/\rho)(\nabla_\alpha \cdot (\rho Y_i V_{i,\alpha})) \end{bmatrix} \quad (\text{A.19})$$

$$\begin{bmatrix} s_u \\ s_v \\ s_w \\ s_\rho \\ s_p \\ s_{Y_i} \end{bmatrix} = \begin{bmatrix} \sum_{i=1}^N Y_i f_{i,x} + (\psi_u - u\psi_\rho)/\rho \\ \sum_{i=1}^N Y_i f_{i,y} + (\psi_v - v\psi_\rho)/\rho \\ \sum_{i=1}^N Y_i f_{i,z} + (\psi_w - w\psi_\rho)/\rho \\ \psi_\rho \\ (\gamma - 1)(\sum_{i=1}^N [-(h_i - c_p TW/W_i)(W_i \dot{\omega}_i + \psi_\rho \delta_{i,H_2O}) \\ + \rho Y_i f_{i,\alpha} V_{i,\alpha}] + \frac{1}{2} \mathbf{u}_\alpha \mathbf{u}_\alpha \psi_\rho - \mathbf{u}_\alpha \psi_{\mathbf{u}_\alpha} + \psi_{et}) \\ (1/\rho)(W_i \dot{\omega}_i + (1 - Y_i) \psi_\rho \delta_{i,H_2O}) \end{bmatrix} \quad (\text{A.20})$$

Equation A.18 represents the characteristic form of the Navier-Stokes equations.

Below we compile the terms in equation A.6 in tabular form:

Table A.1: Temporal part in characteristic form

$(S^{(n)})_{ad}^{-1} \frac{\partial U_d}{\partial t}$	x-direction	y-direction	z-direction
$(S^{(n)})_{1d}^{-1} \frac{\partial U_d}{\partial t}$	$\frac{1}{2}(\frac{\partial p}{\partial t} - \rho c \frac{\partial u}{\partial x})$	$\frac{1}{2}(\frac{\partial p}{\partial t} - \rho c \frac{\partial v}{\partial x})$	$\frac{1}{2}(\frac{\partial p}{\partial t} - \rho c \frac{\partial w}{\partial x})$
$(S^{(n)})_{2d}^{-1} \frac{\partial U_d}{\partial t}$	$\frac{\partial v}{\partial t}$	$\frac{\partial u}{\partial t}$	$\frac{\partial u}{\partial t}$
$(S^{(n)})_{3d}^{-1} \frac{\partial U_d}{\partial t}$	$\frac{\partial w}{\partial t}$	$\frac{\partial w}{\partial t}$	$\frac{\partial v}{\partial t}$
$(S^{(n)})_{4d}^{-1} \frac{\partial U_d}{\partial t}$	$\frac{\partial \rho}{\partial t} - \frac{1}{c^2} \frac{\partial p}{\partial t}$	$\frac{\partial \rho}{\partial t} - \frac{1}{c^2} \frac{\partial p}{\partial t}$	$\frac{\partial \rho}{\partial t} - \frac{1}{c^2} \frac{\partial p}{\partial t}$
$(S^{(n)})_{5d}^{-1} \frac{\partial U_d}{\partial t}$	$\frac{1}{2}(\frac{\partial p}{\partial t} + \rho c \frac{\partial u}{\partial t})$	$\frac{1}{2}(\frac{\partial p}{\partial t} + \rho c \frac{\partial v}{\partial t})$	$\frac{1}{2}(\frac{\partial p}{\partial t} + \rho c \frac{\partial w}{\partial t})$
$(S^{(n)})_{(5+i)d}^{-1} \frac{\partial U_d}{\partial t}$	$\frac{\partial Y_i}{\partial t}$	$\frac{\partial Y_i}{\partial t}$	$\frac{\partial Y_i}{\partial t}$

Table A.2: Normal flux terms in conservative variable form in terms of \mathcal{L} .

$\mathbf{d}^{(n)} = S \mathcal{L}_c^{(n)}$	x-direction	y-direction	z-direction
\mathbf{d}_1	$\frac{1}{\rho c} (\mathcal{L}_5^{(x)} - \mathcal{L}_1^{(x)})$	$\mathcal{L}_2^{(y)}$	$\mathcal{L}_2^{(z)}$
\mathbf{d}_2	$\mathcal{L}_2^{(x)}$	$\frac{1}{\rho c} (\mathcal{L}_5^{(y)} - \mathcal{L}_1^{(y)})$	$\mathcal{L}_3^{(z)}$
\mathbf{d}_3	$\mathcal{L}_3^{(x)}$	$\mathcal{L}_3^{(y)}$	$\frac{1}{\rho c} (\mathcal{L}_5^{(z)} - \mathcal{L}_1^{(z)})$
\mathbf{d}_4	$\frac{1}{c^2} (c^2 \mathcal{L}_4^{(x)} + \mathcal{L}_5^{(x)} + \mathcal{L}_1^{(x)})$	$\frac{1}{c^2} (c^2 \mathcal{L}_4^{(y)} + \mathcal{L}_5^{(y)} + \mathcal{L}_1^{(y)})$	$\frac{1}{c^2} (c^2 \mathcal{L}_4^{(z)} + \mathcal{L}_5^{(z)} + \mathcal{L}_1^{(z)})$
\mathbf{d}_5	$\mathcal{L}_5^{(x)} + \mathcal{L}_1^{(x)}$	$\mathcal{L}_5^{(y)} + \mathcal{L}_1^{(y)}$	$\mathcal{L}_5^{(z)} + \mathcal{L}_1^{(z)}$
\mathbf{d}_{5+i}	$\mathcal{L}_{5+i}^{(x)}$	$\mathcal{L}_{5+i}^{(y)}$	$\mathcal{L}_{5+i}^{(z)}$

Table A.3: Normal flux terms in conservative variable form in terms of \mathbf{d} .

Equation	$\nabla_{(n)} \cdot \mathbf{F}^{(n)}$
x-Momentum	$\rho \mathbf{d}_1^{(n)} + u \mathbf{d}_4^{(n)}$
y-Momentum	$\rho \mathbf{d}_2^{(n)} + v \mathbf{d}_4^{(n)}$
z-Momentum	$\rho \mathbf{d}_3^{(n)} + w \mathbf{d}_4^{(n)}$
Continuity	$\mathbf{d}_4^{(n)}$
Energy	$\rho u \mathbf{d}_1^{(n)} + \rho v \mathbf{d}_2^{(n)} + \rho w \mathbf{d}_3^{(n)} + (e_t - c_v T) \mathbf{d}_4^{(n)} + \frac{\mathbf{d}_5^{(n)}}{(\gamma-1)} + \sum_{i=1}^N \rho \mathbf{d}_{5+i}^{(n)} (h_i - c_p T W / W_i)$

Table A.4: Transverse, viscous and source terms w.r.t. x-direction in characteristic form

$-\mathcal{A}_{cd}^{(t)} \cdot (\nabla_{(t)} U_d)$	\mathcal{D}_c	\mathfrak{s}_c
$\mathfrak{T}_1 = -(\mathbf{v}_t \cdot \nabla_t p + \gamma p \nabla \cdot \mathbf{v}_t - \rho c \mathbf{v}_t \nabla_t u) / 2$	$V_1 = (d_p - \rho c d_u) / 2$	$S_1 = (s_p - \rho c s_u) / 2$
$\mathfrak{T}_2 = (\mathbf{v}_t \cdot \nabla_t v + (1/\rho) \partial p / \partial y)$	$V_2 = d_v$	$S_2 = s_v$
$\mathfrak{T}_3 = -(\mathbf{v}_t \cdot \nabla_t w + (1/\rho) \partial p / \partial z)$	$V_3 = d_w$	$S_3 = s_w$
$\mathfrak{T}_4 = -\nabla_t \cdot (\rho \mathbf{v}_t) + (\mathbf{v}_t \cdot \nabla_t p + \gamma p \nabla_t \cdot \mathbf{v}_t) / c^2$	$V_4 = d_\rho - d_p / c^2$	$S_4 = s_\rho - s_p / c^2$
$\mathfrak{T}_5 = -(\mathbf{v}_t \cdot \nabla_t p + \gamma p \nabla \cdot \mathbf{v}_t + \rho c \mathbf{v}_t \nabla_t u) / 2$	$V_5 = (d_p + \rho c d_u) / 2$	$S_5 = (s_p + \rho c s_u) / 2$
$\mathfrak{T}_{5+i} = -\mathbf{v}_t \cdot \nabla_t Y_i$	$V_{5+i} = d_{Y_i}$	$S_{5+i} = s_{Y_i}$

Table A.5: Transverse, viscous and source terms w.r.t. y-direction in characteristic form

$-\mathcal{A}_{cd}^{(t)} \cdot (\nabla_{(t)} U_d)$	\mathcal{D}_c	\mathfrak{s}_c
$\mathfrak{T}_1 = -(\mathbf{v}_t \cdot \nabla_t p + \gamma p \nabla \cdot \mathbf{v}_t - \rho c \mathbf{v}_t \nabla_t v)/2$	$V_1 = (d_p - \rho c d_v)/2$	$S_1 = (s_p - \rho c s_v)/2$
$\mathfrak{T}_2 = (\mathbf{v}_t \cdot \nabla_t u + (1/\rho) \partial p / \partial x)$	$V_2 = d_u$	$S_2 = s_u$
$\mathfrak{T}_3 = -(\mathbf{v}_t \cdot \nabla_t w + (1/\rho) \partial p / \partial z)$	$V_3 = d_w$	$S_3 = s_w$
$\mathfrak{T}_4 = -\nabla_t \cdot (\rho \mathbf{v}_t) + (\mathbf{v}_t \cdot \nabla_t p + \gamma p \nabla_t \cdot \mathbf{v}_t) / c^2$	$V_4 = d_\rho - d_p / c^2$	$S_4 = s_\rho - s_p / c^2$
$\mathfrak{T}_5 = -(\mathbf{v}_t \cdot \nabla_t p + \gamma p \nabla \cdot \mathbf{v}_t + \rho c \mathbf{v}_t \nabla_t v) / 2$	$V_5 = (d_p + \rho c d_v) / 2$	$S_5 = (s_p + \rho c s_v) / 2$
$\mathfrak{T}_{5+i} = -\mathbf{v}_t \cdot \nabla_t Y_i$	$V_{5+i} = d_{Y_i}$	$S_{5+i} = s_{Y_i}$

Table A.6: Transverse, viscous and source terms w.r.t. z-direction in characteristic form

$-\mathcal{A}_{cd}^{(t)} \cdot (\nabla_{(t)} U_d)$	\mathcal{D}_c	\mathfrak{s}_c
$\mathfrak{T}_1 = -(\mathbf{v}_t \cdot \nabla_t p + \gamma p \nabla \cdot \mathbf{v}_t - \rho c \mathbf{v}_t \nabla_t w) / 2$	$V_1 = (d_p - \rho c d_w) / 2$	$S_1 = (s_p - \rho c s_w) / 2$
$\mathfrak{T}_2 = (\mathbf{v}_t \cdot \nabla_t u + (1/\rho) \partial p / \partial x)$	$V_2 = d_u$	$S_2 = s_u$
$\mathfrak{T}_3 = -(\mathbf{v}_t \cdot \nabla_t v + (1/\rho) \partial p / \partial y)$	$V_3 = d_v$	$S_3 = s_v$
$\mathfrak{T}_4 = -\nabla_t \cdot (\rho \mathbf{v}_t) + (\mathbf{v}_t \cdot \nabla_t p + \gamma p \nabla_t \cdot \mathbf{v}_t) / c^2$	$V_4 = d_\rho - d_p / c^2$	$S_4 = s_\rho - s_p / c^2$
$\mathfrak{T}_5 = -(\mathbf{v}_t \cdot \nabla_t p + \gamma p \nabla \cdot \mathbf{v}_t + \rho c \mathbf{v}_t \nabla_t w) / 2$	$V_5 = (d_p + \rho c d_w) / 2$	$S_5 = (s_p + \rho c s_w) / 2$
$\mathfrak{T}_{5+i} = -\mathbf{v}_t \cdot \nabla_t Y_i$	$V_{5+i} = d_{Y_i}$	$S_{5+i} = s_{Y_i}$

APPENDIX B

Soot source terms for Method of Moments with Interpolative Closure (MOMIC)

B.1 Moment non-dimensionalization

Table B.1: Reference parameters for soot

L_{ref}	reference length
a_{ref}	reference acoustic speed
t_{ref}	reference time scale L_{ref}/a_{ref}
N_{av}	Avogadro's number
d_p	reference particle diameter

Table B.2: Physical parameters for soot

ρ_s	density of soot
m_c	reference number of carbon in particles

Table B.3: Soot non-dimensional values

$N_{k,ref} = \frac{N_{av}}{L_{ref}^3}$	reference value for number density
$\tilde{m}_k = \frac{m_k}{n_c}$	non-dimensional carbon particles in class k
$M_{r,ref} = \frac{N_{av}}{L_{ref}^3} n_c^r$	reference value for moment of moment r

The value of n_c is derived from:

$$n_c = \frac{\pi \rho_s d_p^3}{6m_c} \quad (\text{B.1})$$

Assuming a particle of 300 nm diameter, the corresponding reference number is $n_c = 1.277 \times 10^9$ particles. This value is chosen as the reference value n_c .

The final non-dimensionalized Moment Transport Equation is:

$$\begin{aligned} \frac{\partial \tilde{M}_r}{\partial \tilde{t}} + \frac{\partial}{\partial \tilde{x}_i} \left(\tilde{M}_r \tilde{U}_i \right) &= \frac{L_{ref}^3}{N_{av} n_c^{r-\frac{2}{3}}} \frac{\partial}{\partial \tilde{x}_i} \left(\tilde{D}_0 \frac{\partial M_{r-\frac{2}{3}}}{\partial \tilde{x}_i} \right) \\ &- \frac{\partial}{\partial \tilde{x}_i} \left(\tilde{M}_r \tilde{U}_{T,i} \right) + \frac{t_{ref}}{M_{r,ref}} \dot{M}_r \end{aligned} \quad (\text{B.2})$$

B.2 Stineman interpolation code

```

=====
subroutine stineint(nt,xpm,ypm,ns,xi,yi)
=====

! Perform Stineman interpolation
! Original FORTRAN 77 version written by Gerardo M.E. Perillo
! (Perillo@criba.edu.ar) and M. Cintia Piccolo (Piccolo@criba.edu.ar)
! Instituto Argentino de Oceanographica
! Av. Alem 53, 8000 Bahia Blanca, Argentina

```



```

! Adapted in FORTRAN 90 by Dr. Vivien Lecoustre (vlecous1@umd.edu)
! Fire Protection Engineering Department, University of Maryland
! College Park, Md, USA
!
! NT : length of vectors X and Y
! X : Values of X-axis
! Y : Values of Y-axis
! NS : Length of vector XI and YI
! XI : Values on X-axis to be interpolated
! _____
! - OUTPUT -
! _____
! YI : Vector of interpolated values
!
! _____
implicit none
integer, intent(in) :: nt, ns
real, dimension(ns), intent(in) :: xi
real, dimension(ns), intent(out) :: yi
real, dimension(nt), intent(in) :: xpm, ypm
! — local variables —
real, dimension(nt-1) :: slope
real, dimension(nt) :: t

integer i,j,k,nk
real a, b, c, d, w1, w2, p, as, ay, y0, d1, d2, z, e, f

```

```

! Initialize variables
slope = 0.0
w1 = 1.0
w2 = 1.0
a = 1.0
b = 1.0
c = 1.0
d = 1.0
!-----
p = 0.0
as = 0.0
ay = 0.0
y0 = 0.0
d1 = 0.0
d2 = 0.0
z = 0.0
e = 0.0
f = 0.0
yi(:) = 0.0
slope(:) = 0.0
!-----
! Estimation of slopes
! if((xi(1).lt.0.5).and.xi(1).gt.0.2) write(*,*) 'xi =', xi(ns)
do i = 1,(nt-1)
slope(i) = (ypm(i+1)-ypm(i))/(xpm(i+1)-xpm(i))
enddo

```

```

!-----
! Estimation of derivative

do j = 2,(nt-1)
  i = j-1
  k = j+1

  a = ypm(j)-ypm(i)
  b = xpm(k)-xpm(j)
  c = ypm(k)-ypm(j)
  d = xpm(j)-xpm(i)

  w1 = a*(b**2+c**2)+c*(d**2+a**2)
  w2 = d*(b**2+c**2)+b*(d**2+a**2)

  if (w2.eq.0.0d+0) then
    t(j) = 0.0d+0
  else
    t(j) = w1/w2
  endif

enddo

p = slope(1)-t(2)

if (slope(1)*p.gt.0.0d+0) then !slope(1) and p have the same sign
  t(1) = 2.0d+0*slope(1)-t(2)

```

```

else
as = abs(slope(1))
ay = abs(p)
w1 = as*p
w2 = as + ay

if (w2.eq.0.0) then
t(1) = slope(1)
else
t(1) = slope(1) + w1/w2
endif

endif

p = slope(nt-1) - t(nt-1)

if (slope(nt-1)*p.gt.0.0d+0) then !slope(nt-1) and p have the same sign
t(nt) = 2.0d+0*slope(nt-1)-t(nt-1)
else
as = abs(slope(nt-1))
ay = abs(p)
w1 = as*p
w2 = as + ay

if (w2.eq.0.0) then
t(nt) = slope(nt-1)
else

```

```
t(nt) = slope(nt-1) + w1/w2
```

```
endif
```

```
endif
```

```
!-----
```

```
! Interpolation
```

```
k = 1
```

```
! if((xi(1).lt.0.5).and.xi(1).gt.0.2) write(*,*) 'xi =', xi(ns)
```

```
do j = 1, nt-1,1
```

```
nk = 0
```

```
! i = 1
```

```
do i = k, ns
```

```
a = xi(i)-xpm(j)
```

```
b = xi(i)-xpm(j+1)
```

```
c = xpm(j+1)-xpm(j)
```

```
if (xi(i).le.xpm(1)) then
```

```
if (xi(i).eq.xpm(1))then
```

```
yi(i) = ypm(j)
```

```
else
```

```
yi(i) = 0.0d+0
```

```
endif
```

```
nk = nk + 1
```

```
if((xi(1).lt.0.5).and.xi(1).gt.0.2) write(*,*) 'false xi =', xi(ns)
elseif (xi(i).ge.xpm(nt)) then
```

```
if (xi(i).eq.xpm(nt)) then
```

```
yi(i) = ypm(nt)
```

```
else
```

```
yi(i) = 0.0d+0
```

```
endif
```

```
nk = nk + 1
```

```
if((xi(1).lt.0.5).and.xi(1).gt.0.2) write(*,*) 'false xi =', xi(ns)
```

```
elseif ((xi(i).ge.xpm(j)).and.(xi(i).lt.xpm(j+1))) then
```

```
y0 = ypm(j) + slope(j)*a
```

```
d1 = ypm(j) + t(j)*a - y0
```

```
d2 = ypm(j+1)+t(j+1)*b - y0
```

```
z = d1*d2
```

```
if(z.ge.0.0d+0) then
```

```
yi(i) = y0
```

```
elseif(z.ge.1e-100) then
```

```
yi(i) = y0 + z/(d1+d2)
```

```
elseif (z.lt.0.0d+0) then
```

```
e = z*(a+b)
```

```
f = (d1-d2)*c
```

```
yi(i) = y0 + e/f
```

endif

$nk = nk + 1$

else

go to 255

endif

enddo

255 continue

$k = k + nk$

enddo

return

end subroutine stineint

!-----

BIBLIOGRAPHY

BIBLIOGRAPHY

- Appel, J., H. Bockhorn, and M. Frenklach (2000), Kinetic modeling of soot formation with detailed chemistry and physics: Laminar premixed flames of c2 hydrocarbons, *Combustion and Flame*, 121, 122–136.
- Arias, P. G., H. G. Im, P. Narayanan, and A. Trouvé (2010), Direct numerical simulation of nonpremixed flame extinction by water spray, in *48th AIAA Aerospace Sciences Meeting*, Orlando, Florida.
- Baum, M., T. Poinso, and D. Thévenin (1995), Accurate boundary conditions for multicomponent reactive flows, *Journal of Computational Physics*, 116(2), 247–261, doi:10.1006/jcph.1995.1024.
- Bilger, R. (1977), Reaction rates in diffusion flames, *Combustion and Flame*, 30(277–284).
- Chao, B., C. Law, and J. T'ien (1990), Structure and extinction limits of diffusion flames with flame radiation, *Symposium (International) on Combustion*, 23, 523–531.
- Colonius, T. (2004), Modeling artificial boundary conditions for compressible flow, *Annual Review of Fluid Mechanics*, 36(315–345).
- Frenklach, M. (2002), Method of moments with interpolative closure, *Chemical Engineering Science*, 57, 2229–2239.
- Frenklach, M., and H. Wang (1990), Detailed modeling of soot particle nucleation and growth, *Symposium (International) on Combustion*, 23, 365–370.
- Ihme, M., and Y. C. See (2011), Les flamelet modeling of a three-stream mild combustor: Analysis of flame sensitivity to scalar inflow conditions, *Proceedings of the Combustion Institute*, 33, 1309–1317.
- Im, H. G., and J. H. Chen (1999), Structure and propagation of triple flames in partially premixed hydrogen-air mixtures, *Combustion and Flame*, 119(4), 436–454, doi:10.1016/S0010-2180(99)00073-5.
- Im, H. G., A. Trouvé, and C. Rutland (2007), Direct numerical simulation of turbulent flame quenching by fine water droplets, *Tech. rep.*, Innovative and Novel Computational Impact on Theory and Experiment (INCITE), Department of Energy.

- Kim, S. H., K. Y. Huh, and B. Dally (2005), Conditional moment closure modeling of turbulent nonpremixed combustion in diluted hot coflow, *Proceedings of the Combustion Institute*, *30*, 751–757.
- Lignell, D. O., J. H. Chen, P. J. Smith, T. Lu, and C. K. Law (2007), The effect of flame structure on soot formation and transport in turbulent nonpremixed flames using direct numerical simulation, *Combustion and Flame*, *151*(1-2), 2–28, doi: 10.1016/j.combustflame.2007.05.013.
- Linán, A. (1974), The asymptotic structure of counterflow diffusion flames for large activation energies, *Acta Astronautica*, *1*, 1007–1039.
- Lu, T., and C. K. Law (2005), A directed relation graph method for mechanism reduction, *Proceedings of the Combustion Institute*, *30*, 1333–1341.
- Lutz, A., R. Kee, J. Grear, and F. Rupley (1996), Oppdif: a fortran program for computing opposed flow diffusion flames, *Tech. Rep. SAND96-8243*, Sandia National Laboratories.
- Mehta, R., D. Haworth, and M. Modest (2009), An assessment of gas-phase reaction mechanisms and soot models for laminar atmospheric-pressure ethylene–air flames, *Proceedings of the Combustion Institute*, *32*, 1327–1334.
- Moss, J., C. Stewart, and K. Syed (1988), Flowfield modeling of soot formation at elevated pressure, *Symposium (International) on Combustion*, *22*, 413–423.
- Moss, J., C. Stewart, and K. Young (1995), Modeling soot formation and burnout in a high temperature laminar diffusion flame burning under oxygen-enriched conditions, *Combustion and Flame*, *101*(491-500).
- Narayanan, P., and A. Trouve (2009), Radiation-driven flame weakening effects in sooting turbulent diffusion flames, *Proceedings of the Combustion Institute*, *32*(1), 1481–1489.
- Narayanan, P., H. Baum, and A. Trouvé (2009a), Asymptotic analysis of radiative extinction in laminar counterflow diffusion flames, in *Fall Technical Meeting of the Eastern States Section of the Combustion Institute*, Paper C-31, College Park, Maryland.
- Narayanan, P., A. Trouve, P. G. Arias, and H. G. Im (2009b), Mixture fraction and state relationships in diffusion flames interacting with an evaporating water spray, in *6th U.S. National Combustion Meeting*, Ann Arbor, MI.
- Peters, N. (1983), Local quenching due to flame stretch and non-premixed turbulent combustion, *Combustion Science and Technology*, *30*, 1–6.
- Poinsot, T., and S. K. Lele (1992), Boundary conditions for direct simulations of compressible viscous flows, *Journal of Computational Physics*, *101*, 104–129, doi: 10.1016/0021-9991(92)90046-2.

- Rudy, D. H., and J. C. Strikwerda (1980), A nonreflecting outflow boundary condition for subsonic navier-stokes calculations, *Journal of Computational Physics*, *36*(1), 55–70, doi:10.1016/0021-9991(80)90174-6.
- Sun, C., C. Sung, L. He, and C. Law (1999), Dynamics of weakly stretched flames: quantitative description and extraction of global flame parameters, *Combustion and Flame*, *118*(1-2), 108 – 128.
- Sutherland, J. C., and C. A. Kennedy (2003), Improved boundary conditions for viscous, reacting, compressible flows, *Journal of Computational Physics*, *191*(2), 502 – 524.
- Thompson, K. W. (1987), Time dependent boundary conditions for hyperbolic systems, *Journal of Computational Physics*, *68*, 1–24.
- Vikas, V., Z. Wang, A. Passalacqua, and R. Fox (2011), Realizable high-order finite-volume schemes for quadrature-based moment methods, *Journal of Computational Physics*, *230*, 5328–5352.
- Wang, H., W. Chen, and C. Law (2007), Extinction of counterflow diffusion flames with radiative heat loss and nonunity lewis numbers, *Combustion and Flame*, *148*(3), 100–116.
- Wang, Y., and C. Rutland (2005), Effects of temperature and equivalence ratio on the ignition of n-heptane fuel spray in turbulent flow, *Proceedings of the Combustion Institute*, *30*, 893–900.
- Wang, Y., and C. Rutland (2007), Direct numerical simulation of ignition in turbulent n-heptane liquid-fuel spray jets, *Combustion and Flame*, *149*(4), 353 – 365, doi: 10.1016/j.combustflame.2007.03.005.
- Wang, Y., and A. Trouvé (2004), Artificial acoustic stiffness reduction in fully compressible, direct numerical simulation of combustion, *Combustion Theory and Modeling*, *8*(3), 633–660.
- Wang, Y., and A. Trouve (2006), Direct numerical simulation of nonpremixed flame-wall interactions, *Combustion and Flame*, *144*(3), 461–475.
- Williams, F. A. (1985), *Combustion Theory*, 2nd ed., The Benjamin/Commings Publishing Company, Inc, 2727 Sand Hill Road, Menlo Park, California 94025.
- Xia, J., K. Luo, and S. Kumar (2008), Large-eddy simulation of interactions between a reacting jet and evaporating droplets, *Flow, Turbulence and Combustion*, *80*, 133–153, doi:10.1007/s10494-007-9084-4.
- Yoo, C. S., and H. G. Im (2007a), Transient soot dynamics in turbulent nonpremixed ethylene-air counterflow flames, *Proceedings of the Combustion Institute*, *31*(1), 701 – 708.

Yoo, C. S., and H. G. Im (2007b), Characteristic boundary conditions for simulations of compressible reacting flows with multi-dimensional, viscous and reaction effects, *Combustion Theory and Modelling*, 11(2), 259–286, doi:10.1080/13647830600898995.

Yoo, C. S., Y. Wang, A. Trouvé, and H. G. Im (2005), Characteristic boundary conditions for direct simulations of turbulent counterflow flames, *Combustion Theory and Modeling*, 9(4), 617–646, doi:10.1080/13647830500307378.